Technische
Universität
München

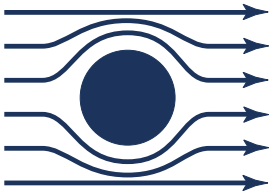

Walther-Meißner
Institut

Bayerische
Akademie
der Wissenschaften

Disentangling Electrical and Thermal Modulations of Magnon Conductivity in Yttrium Iron Garnet

---

Master's thesis

Emir Karadža

Supervisor

Prof. Dr. Rudolf Gross

Advisors

Dr. Matthias Althammer

Tobias Wimmer

Garching – 4. Januar 2021

Contents

1 Introduction

As far as our current knowledge extends, our universe is (for the most part) well-described by the widely accepted Standard Model and thus believed to be made up of matter and force fields. According to this model, the line of distinction between matter and the force-carrying particles is their associated quantum-mechanically defined intrinsic angular momentum - *spin*. All known matter particles posses a half-integer spin ($\frac{\hbar}{2}$), therefore obeying the Fermi-Dirac statistics (fermions), whereas the force-carrying particles exhibit an integer spin ($\hbar$) and are governed by the Bose-Einstein statistics (bosons). The zero-spin Higgs boson can be thought of as a particle manifestation of the equally named field, giving mass to elementary particles and therefore constitutes a special case.

As a physical observable, spin is riddling the community since its discovery [1] almost 100 years ago, when Uhlenbeck and Goudsmit proposed that Pauli's 4^{th} quantum number [2] could be associated with a self-rotation (spin) of electrons. The revolutionists themselves were, however, aware of the fact that this classical explanation was not adequate [3], but the term remained until today. The spin of an electron, being an exclusively relativistic quantum-mechanical phenomenon, has as of now no associated classical counterpart, whereas the spin of photons, for example, can be classically rationalized as the analog of a light wave polarization. Nevertheless, on account of this strange feature, electrons exhibit a finite spin magnetic moment, therefore giving rise to magnetism in solids. The magnetic moment $\boldsymbol{m}_{\mathrm{es}}$, associated with the electron's spin angular momentum $\boldsymbol{S}$, can be written as $\boldsymbol{m}_{\mathrm{es}} = \gamma \boldsymbol{S}$, with γ denoting the gyromagnetic ratio. For electrons, this ratio is given as $\gamma = \frac{g q_{\mathrm{e}}}{m_{\mathrm{e}}}$, where $q_{\mathrm{e}} = -e < 0$ and m_{e} denote the electron's charge and resting mass, respectively, and $g \approx 2$ is the Landé factor. Using these relations, we obtain the magnetic moment of a single electron as $m_{\mathrm{es}} \approx \frac{e\hbar}{2m_{\mathrm{e}}}$, generally known as the Bohr magneton μ_{B}. These handful of equations account for one of the biggest findings of the 20^{th} century physics. However, several decades passed by until the concept of spin found its first practical applications.

Since the discovery of the transistor, the electronics and information processing technology were almost exclusively based on semiconductor technology, harnessing the intrinsic electronic structure of semiconductors and controlling it by using electric fields. Transistors are thus considered to be one of the greatest inventions of the 20^{th} century, which is also certified by the 1956 Nobel Prize in Physics being awarded to Shockley, Bardeen and Brattain "for their researches on semiconductors and the discovery of the transistor effect"[4]. The fast developing semiconductor industry initiated an exponential development of all spheres of human activity, especially by allowing immense scientific progress by making personal computers affordable and widely available. Described by the two famous scaling laws, namely Moore's [5] and Dennard's [6] law, it was predicted that the number of transistors in an integrated circuit would double about every two years and that the power consumption would scale proportionally with the reduced transistor size. Eventually, Dennard's law was abandoned after being valid for 4 decades [7], whereas Moore's law is about to reach its limit, since the size of transistors approaches its physical limit where quantum tunneling effects start playing an important role [8]. As further miniaturization of microelectronic components is increasingly challenging and the demand for low-power data storage and processing evergrowing, novel approaches and solutions for the field of

information processing technology need to be provided [9].

Introducing the spin degree of freedom of electrons is a natural route towards the implementation of current technology via spintronics devices [10]. The field of spintronics aims for manipulation of the intrinsic spin of the electron and its associated magnetic moment in addition to its charge. Being a relatively young field, spintronics established as one of the most promising applied-science fields of the future, yielding important discoveries in both fundamental research and practical devices. Probably the best known derivative of spintronics, the giant magnetoresistance (GMR) discovered by Fert [11] and Grünberg [12], led to a revolution in data storage technology which was awarded by the Nobel committee, recognizing the importance of this finding with the 2007 Nobel Prize in Physics. Another important milestone of spintronics is the transport of angular momentum without accompanying charge transport - a concept known as *pure spin currents* [13]. These currents can be observed for example in nonmagnetic (normal) metals (NM) as well as in magnetically ordered insulators (MOI). The insulating nature of the latter prohibits transport of angular momentum by spin-carrying conduction electrons. In such systems, spin currents manifest in form of spin waves - representing fundamental magnetic excitations in magnetically ordered materials, known as *magnons*. Besides the obvious advantage of being able to transport informations in insulating materials (provided the material is in a magnetically ordered phase), the absence of charge currents could potentially decrease losses associated with Joule heating [14]. Furthermore, magnons have an integer spin and belong to the particle class known as bosons. Contrary to fermions, which are governed by the Pauli exclusion principle, an ensemble of bosons can collectively be driven into the lowest energy state (ground state), a phenomenon known as Bose-Einstein condensation. In this state, magnons could theoretically offer dissipationless transport [15, 16].

In this work, we investigate magnon transport in magnetic transistor devices [17, 18] in the form of NM/MOI heterostructures. A pure spin current, induced by the spin Hall effect (SHE) [19, 20, 21] in a platinum contact (injector), excites non-equilibrium magnons in the adjacent MOI layer [22, 23]. These non-equilibrium magnons diffuse trough the MOI in form of spin waves and can be detected in a second spatially separated and electrically isolated Pt contact (detector) via the inverse spin Hall effect (ISHE) [24]. Furthermore, magnons can be excited thermally by means of the spin Seebeck effect (SSE) [25, 26]. Introducing a third Pt electrode (modulator) placed in between the first two allows to modulate the transport by additionally exciting magnons thermally (SSE) and electrically (SHE) in the magnon transport channel, hence tuning the magnon conductivity of the MOI [17, 18]. In order to gain a deeper insight in the underlying physics of magnon transport, we set out to disentangle the electrically and thermally induced magnon conductivity modulations by using modulator electrodes made of different materials. The materials were choosen specifically to allow progressive reduction of the electrical contribution and were characterized by means of spin Hall magnetoresistance (SMR) measurements.

This thesis is organized as follows: in Chap. 2, an overview of the theoretical concepts essential for this work is offered. The experimental details regarding the choice of materials, the sample fabrication methods and the employed measurement techniques are presented in Chap. 3. In Chap. 4, we characterize different PtAu alloys as potential materials with pronounced SHE efficiency in a series of temperature, magnetic field and alloy thickness

dependent SMR measurements on yttrium iron garnet (YIG) substrates. Furthermore we offer an overview of all metals used in this thesis and precharacterize them by means of SMR measurements. The center of attention of this thesis is Chap. 5, where we discuss magnon transport measurements in NM/YIG heterostrucutes, attempting to phenomenologically understand and discern the mechanisms of electrical and thermal magnon conductivity modulation. The thesis is concluded with a summary and an outlook in Chap. 6.

2 Theoretical Concepts

In order to realize devices harnessing the spin degree of freedom, it is of crucial importance to acquaint oneself with the essence of spin currents as well as with the methods enabling their generation and detection. The aim of this Chapter is, therefore, to offer a brief overview of electronic spin currents (Chap. 2.1) and the spin Hall effect (SHE, Chap. 2.2), representing the most prominent way for generating (direct SHE) and detecting (indirect SHE) pure spin currents. Moreover, we discuss the spin Hall magnetoresistance (SMR, Chap. 2.3) effect, which offers an expedient way to characterize the SHE physics of a normal metal (NM) when structured in a bilayer structure with a magnetically ordered insulator (MOI). Finally, the excitation and transport of spin waves in form of magnonic spin currents in NM/MOI bilayers, being the main focus of this thesis, are introduced in Chap. 2.4.

2.1 Spin Currents

Our intuitive understanding of charge currents inevitably invokes the picture of moving electrons along a certain direction. However, besides being carriers of elementary charge $q_\mathrm{e} = -e$ (with $e > 0$), electrons are also well known to exhibit an intrinsic spin angular momentum $S = \pm\frac{\hbar}{2}$. It is due to its quantum-mechanical origin that measuring spin along an axis (quantization axis) can yield only two results: parallel $S = +\frac{\hbar}{2} = |\uparrow\rangle$ (spin-up) and antiparallel $S = -\frac{\hbar}{2} = |\downarrow\rangle$ (spin-down) aligned spin states. Thus, we can say that an electronic charge current is in general accompanied by the transport of spin angular momentum, therefore giving rise to a spin current. In order to describe the two simultaneously emerging currents, we are going to use the two channel model, where the spin-up and spin-down carriers are considered as separate species. This approach is valid under the assumption that the time interval between two spin flip scattering events is relatively long compared to the time interval between two spin-conserving scattering events [27]. The electric charge current density $\boldsymbol{j}_\mathrm{c}$, and the corresponding spin current density $\boldsymbol{j}_\mathrm{s}$, can then be written as [28]:

$$\boldsymbol{j}_\mathrm{c} = -e(n_\uparrow \boldsymbol{v}_\uparrow + n_\downarrow \boldsymbol{v}_\downarrow) = (\boldsymbol{j}_\uparrow + \boldsymbol{j}_\downarrow), \tag{2.1}$$

$$\boldsymbol{j}_\mathrm{s} = \frac{\hbar}{2}(n_\uparrow \boldsymbol{v}_\uparrow - n_\downarrow \boldsymbol{v}_\downarrow) = -\frac{\hbar}{2e}(\boldsymbol{j}_\uparrow - \boldsymbol{j}_\downarrow), \tag{2.2}$$

respectively, with $\boldsymbol{j}_{\uparrow/\downarrow} = -en_{\uparrow/\downarrow}\boldsymbol{v}_{\uparrow/\downarrow}$ accounting for the charge current densities of the two carrier species, where $n_{\uparrow/\downarrow}$ and $\boldsymbol{v}_{\uparrow/\downarrow}$ denote the carrier density and velocity of the particular species, respectively. A charge current represents a local change of charge with respect to time, thus the charge current density is given in units of $\left[\mathrm{Am}^{-2}\right]$. On the other hand, a spin current would correspond to change of angular momentum with respect to time, hence the spin current density is given in units of $\left[\mathrm{Jm}^{-2}\right]$. That being said, the conversion factor $-\frac{\hbar}{2e}$ reflects the fact that the electron is considered as an angular momentum carrier ($\frac{\hbar}{2}$) in $\boldsymbol{j}_\mathrm{s}$, whereas it is seen as a charge carrier ($-e$) in $\boldsymbol{j}_\mathrm{c}$ [28].

The coupled Eqs. 2.1 and 2.2 can be classified by three cases, as illustrated in Fig. 2.1. The first scenario, depicted in **(a)**, illustrates a *pure charge current*. In this case, the current densities of both spin states are equal ($\boldsymbol{j}_\uparrow = \boldsymbol{j}_\downarrow$), therefore corresponding to a net charge

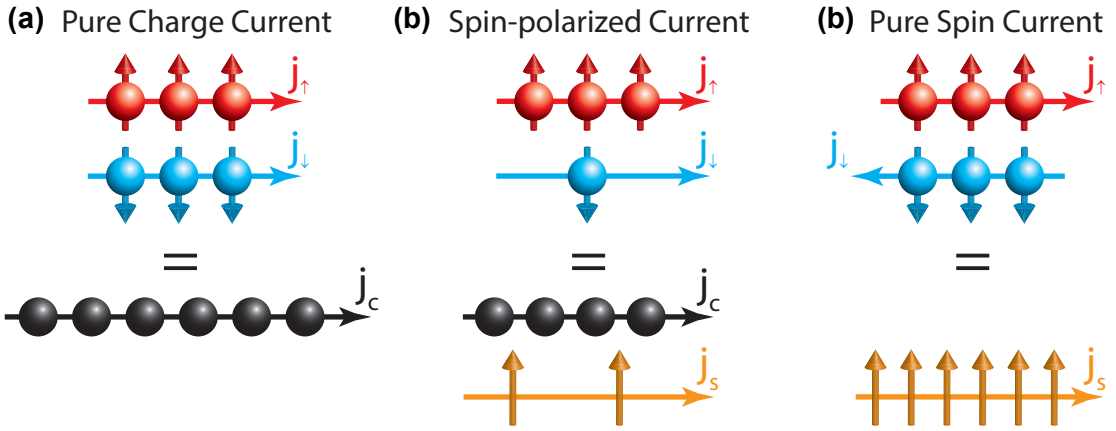

Fig. 2.1: Illustration of charge and spin currents in the two channel model. **(a)** A pure charge current j_c can be represented as the flow of an equal amount of up- and down-spin electrons in the same direction. **(b)** A finite spin polarization of the electron system results in a flow of spin angular momentum accompanying the charge current. **(c)** An equal amount of up- and down-spin electrons flowing in opposite directions gives rise to a pure spin current j_s. Taken from Ref. [29].

transport without an accompanying angular momentum transport. This is in particular the case for normal (paramagnetic) metals with vanishing spin-orbit coupling (SOC). In case of conducting ferromagnets, we typically observe *spin-polarized currents*. Due to the magnetic ordering of these materials, one spin state is energetically favored, causing an asymmetry in the current densities of the two spin states ($j_\uparrow \neq j_\downarrow$). The charge current is therefore associated with a spin current, as illustrated in Fig. 2.1 **(b)**. Last but not least, for equally sized but oppositely directed charge current densities of the two spin states ($j_\uparrow = -j_\downarrow$) as shown in Fig. 2.1 **(c)**, we observe a pure flow of angular momentum without accompanying net charge transport - a *pure spin current*. It is important to point out that such a two channel model is intended to give an intuitive understanding of spin currents, but is limited to systems where the spin currents are carried by electrons. References [30, 31, 32, 33] offer more general approaches for defining the spin current density.

2.2 Spin Hall Effect

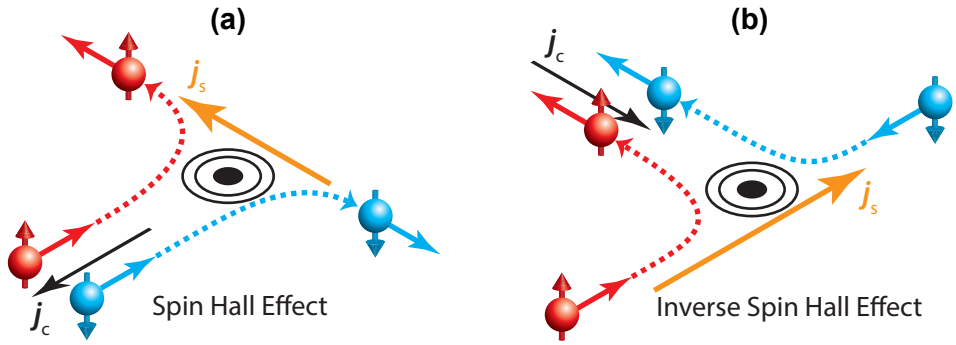

Fig. 2.2: Spin dependent scattering of conduction electrons in paramagnetic materials due to spin-orbit coupling. **(a)** An applied (pure) charge current j_c gives rise to a transverse (pure) spin current j_s as a consequence of the spin Hall effect (SHE). **(b)** In a similar fashion, a (pure) spin charge current j_s will give rise to a transverse (pure) charge current j_c, owing to the inverse spin Hall effect (ISHE). Taken from Ref. [34].

The electrical generation and detection of pure spin currents in this thesis is governed by the spin Hall effect (SHE). This effect was predicted and phenomenologically described by Dyakonov and Perel [19] and subsequently theoretically reformulated by Hirsch [20]. It would take more than 30 years after the original prediction until the first experimental observation of the effect by Kato et al. [21]. For conductors with high SOC, an applied charge current $\boldsymbol{j}_\mathrm{c}$ will lead to spin dependent scattering and deflection of the flowing electron spins as a consequence of the combined influence of extrinsic impurity scattering [35, 36, 37] (i.e. skew- or side-jump-scattering) and intrinsic bandstructure effects [38, 39] (i.e. Berry phase curvature). Consequently, the oppositely oriented spin states obtain transverse velocity components in opposite directions, leading to their spatial separation and therefore giving rise to a transverse spin current $\boldsymbol{j}_\mathrm{s}$, as illustrated in Fig. 2.2 **(a)**. Satisfying the Onsager reciprocity principle [40], a spin current $\boldsymbol{j}_\mathrm{s}$ will be converted into a charge current $\boldsymbol{j}_\mathrm{c}$ due to the same underlying physics, enabling the inverse spin Hall effect (ISHE), as illustrated in Fig. 2.2 **(b)**. The figure of merit for these conversion processes is the dimensionless spin Hall angle θ_SH, reflecting the efficiency of the charge-to-spin/spin-to-charge conversion. We can summarize the SHE and ISHE mathematically with the following equations [41]:

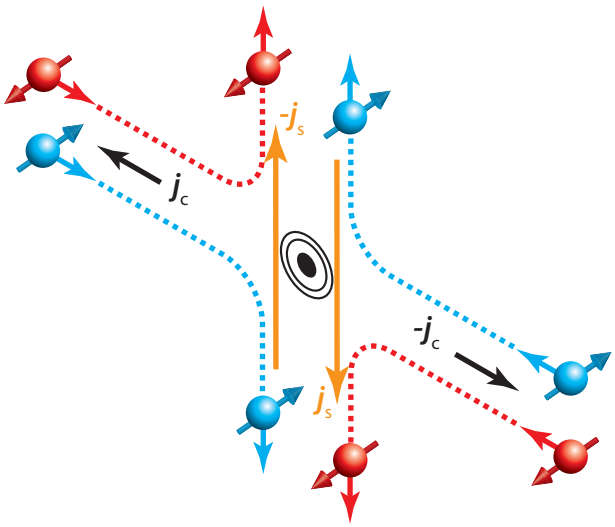

Fig. 2.3: The spin-quantization axis for paramagnetic materials is arbitrary, thus any spin direction with a component perpendicular to the charge current is going to be deflected according to Eq. 2.3. Furhtermore, upon reversal of the charge current $\boldsymbol{j}_\mathrm{c}$, the SHE-induced spin current $\boldsymbol{j}_\mathrm{s}$ is reversed as well. The same effect can be achieved by inverting the sign of the spin Hall angle θ_SH. These observations are as well valid for the ISHE, governed by Eq. 2.4.

$$\boldsymbol{j}_\mathrm{s} = \theta_\mathrm{SH}\frac{\hbar}{2e}\boldsymbol{j}_\mathrm{c} \times \boldsymbol{s}, \tag{2.3}$$

$$\boldsymbol{j}_\mathrm{c} = \theta_\mathrm{SH}\frac{2e}{\hbar}\boldsymbol{j}_\mathrm{s} \times \boldsymbol{s}, \tag{2.4}$$

respectively. Heavy metals, such as platinum (Pt), tungsten (W) or tantalum (Ta), typically have large SOC and thus large spin Hall angles θ_SH, whose sign can vary (c.f. Fig. 2.3). An overview of the metals used in this thesis, together with the literature values of their spin Hall angles θ_SH can be found in Tab. 3.1.

It is important to point out that the SHE is probably the most convenient and eminent way of generating and detecting pure spin currents in normal metals, with the distinct advantage that the spin current can be generated and detected in a single material [42]. One can also utilize nonlocal spin injection [43], spin transfer torque [44], spin pumping [24] and the spin Seebeck effect [45], which require a bilayer structure, with the spin current being generated in one and subsequently detected in the other material of the bilayer. Ne-

vertheless, the SHE was exclusively employed in NM/MOI bilayers within this thesis, as we are going to evince in the following.

2.3 Spin-Hall Magnetoresistance

In the most simplistic picture, one can define magnetoresistance as the susceptibility of a material to change its electrical resistance if placed in an external magnetic field, as firstly discovered by W. Thomson (Lord Kelvin) in 1857 [46]. Nowadays, magnetoresistance effects depending on the magnetization direction of a magnetic material, namely anisotropic [47], giant [11] and tunnel [36] magnetoresistance are considered to be all-important effects in data storage technology. Being observed in metallic magnets, these effects rely on the flow of conduction electrons through the magnet. The spin Hall magnetoresistance (SMR), reported by Nakayama et al. [48] for NM/MOI bilayers, has shown to be a fundamentally different magnetoresistance effect, since the bilayer resistance reflects the magnetization direction of the interfaced MOI, even though the NM's conduction electrons cannot enter the MOI. In order to gain a deeper insight in the underlying physics of this effect, we will consider a NM/MOI structure as illustrated in Fig. 2.4.

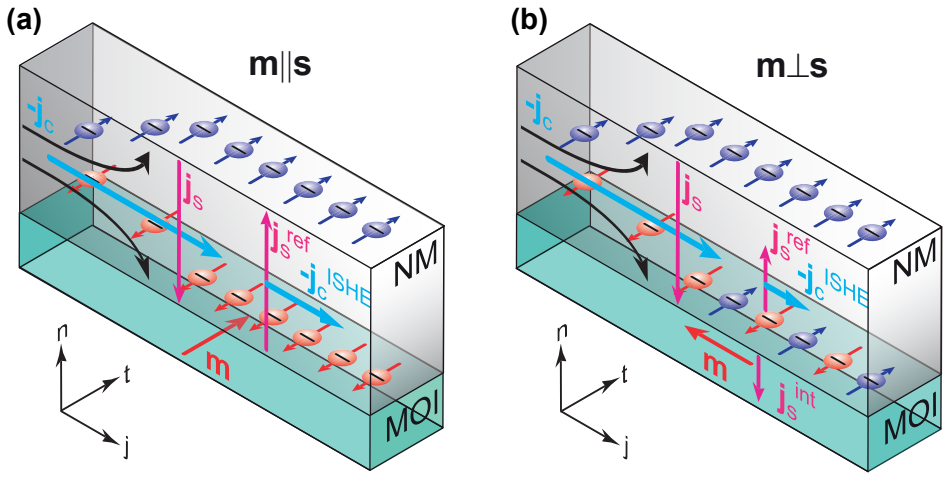

Fig. 2.4: Two limiting cases of SMR in a NM/MOI bilayer. **(a)** For $\boldsymbol{m} \parallel \boldsymbol{s}$, the SHE-induced spin current $\boldsymbol{j}_\mathrm{s}$ cannot enter the MOI, thus being reflected as $\boldsymbol{j}_\mathrm{s}^{ref}$, therefore resembling the NM behavior in absence of the MOI. **(b)** $\boldsymbol{m} \perp \boldsymbol{s}$, $\boldsymbol{j}_\mathrm{s}$ partially enters the MOI, causing a decrease of $\boldsymbol{j}_\mathrm{s}^{ref}$, compared to the first case, subsequently resulting in an increase of the resistance. Adapted from Ref. [49].

If we apply a charge current $-\boldsymbol{j}_\mathrm{c}$ to the NM in the $\mathbf{j}$-direction, a SHE-induced transverse spin current $\boldsymbol{j}_\mathrm{s}$ will flow along $-\mathbf{n}$, with an interfacial spin polarization $\boldsymbol{s}$ pointing along $-\mathbf{t}$ and a NM with positive θ_SH. This will lead to a finite spin accumulation $\boldsymbol{\mu}_\mathrm{s}$ at the NM/MOI interface, provided that the interface is distanced within the length scale of the spin diffusion length λ_s. The spin accumulation is given as $\boldsymbol{\mu}_\mathrm{s} = \mu_\mathrm{s}^0 \boldsymbol{s}$, with μ_s^0 [J] denoting the spin chemical potential at the interface. Generally, spin chemical potentials arise as the result of spatial separation of opposite electronic spin states $\mu_\mathrm{s} = \mu_\uparrow - \mu_\downarrow$ ($\mu_{\uparrow/\downarrow}$ represents the spin chemical potential of the particular spin species) and its gradient represents a driving force for spin currents. Since we are considering a NM/MOI bilayer, we need to introduce the magnetization $\boldsymbol{M}$, with $\boldsymbol{m} = \boldsymbol{M}/|\boldsymbol{M}|$ being the corresponding magnetization direction of the MOI. In the case of a parallel alignment of $\boldsymbol{m}$ and $\boldsymbol{s}$, as depicted in Fig. 2.4 **(a)**, $\boldsymbol{\mu}_\mathrm{s}$ will

as well be parallelly aligned to $\boldsymbol{m}$, therefore not exerting any spin orbit torque (SOT) on $\boldsymbol{M}$ [50]. As a consequence, the SHE-induced spin current cannot penetrate the MOI, thus prohibiting the flow of any interfacial spin current. This results in the total reflection of the SHE-induced spin current, giving rise to the reflected spin current $\boldsymbol{j}_{\mathrm{s}}^{\mathrm{ref}}$ (note the change of direction), which is, via the ISHE, converted into a charge current $-\boldsymbol{j}_{\mathrm{c}}^{\mathrm{ISHE}}$ flowing in the same direction as the initial $-\boldsymbol{j}_{\mathrm{c}}$ (c.f. Eq. 2.4). This case fully resembles the case of the isolated NM, therefore yielding the same resistance as for the plain NM. For the perpendicular alignment of $\boldsymbol{m}$ and $\boldsymbol{s}$, however, $\boldsymbol{\mu}_{\mathrm{s}}$ is able to exert SOT on $\boldsymbol{M}$ [51], with a spin current $\boldsymbol{j}_{\mathrm{s,int}}$ flowing across the interface, therefore causing partial absorption of the spin accumulation $\boldsymbol{\mu}_{\mathrm{s}}$ at the interface. As a consequence, the reflected spin current $\boldsymbol{j}_{\mathrm{s}}^{\mathrm{ref}}$ will be reduced as compared to the first case, giving rise to a lower ISHE-induced charge current $-\boldsymbol{j}_{\mathrm{c}}^{\mathrm{ISHE}}$. In summary, we observe a partial dissipation of the initial charge current $-\boldsymbol{j}_{\mathrm{c}}$ into the MOI for $\boldsymbol{m} \perp \boldsymbol{s}$, which corresponds to the resistance change known as SMR. The exact amount of the spin accumulation/spin current being absorbed in the MOI is governed by the so-called spin mixing conductance $g^{\uparrow\downarrow}$. It measures the number of spin-flip scattering events at the particular NM/MOI interface when $\boldsymbol{m} \perp \boldsymbol{s}$ and can thus be understood intuitively as the number of open channels for spin transport across interfaces with mutually perpendicular spins [52, 53, 54, 55]. The effect can be quantified by writing down the expression for the interfacial spin current [34]:

$$\boldsymbol{j}_{\mathrm{s,int}}(T=0) = \frac{1}{4\pi}\left(g_{\mathrm{i}}^{\uparrow\downarrow} + g_{\mathrm{r}}^{\uparrow\downarrow}\boldsymbol{m}\times\right)(\boldsymbol{\mu}_{\mathrm{s}} \times \boldsymbol{m}), \tag{2.5}$$

with $g_{\mathrm{i}}^{\uparrow\downarrow}$ and $g_{\mathrm{r}}^{\uparrow\downarrow}$ corresponding to the imaginary and real part of $g^{\uparrow\downarrow}$, respectively. We will try to offer a simple explanation for this rather complicated expression which is fully elucidated in Ref. [34]. Obviously, both terms in the equation, with corresponding torques $\propto g_{\mathrm{i}}^{\uparrow\downarrow}$ and $\propto g_{\mathrm{r}}^{\uparrow\downarrow}$, will only be finite for non-collinear alignment of $\boldsymbol{\mu}_{\mathrm{s}}$ and $\boldsymbol{m}$. Furthermore, the second term $\propto \boldsymbol{m} \times (\boldsymbol{\mu}_{\mathrm{s}} \times \boldsymbol{m})$ is governed by the dephasing of spins scattered at the interface due to their precession in the exchange field of $\boldsymbol{m}$. This dephasing results in a loss of transverse spin momentum that is transferred to the magnetic order. Due to incomplete dephasing however, finite transverse momentum will be preserved, therefore directly exerting torque $\propto \boldsymbol{\mu}_{\mathrm{s}} \times \boldsymbol{m}$ to the magnetic order. Taken together, the two contributions sum up to Eq. 2.5. For a phenomenological description, we are interested in the longitudinal resistance change of the NM in the bilayer as a function of the magnetization direction $\boldsymbol{m}$. We can therefore write [48]:

$$\rho_{\mathrm{long}} = \rho_0 + \Delta\rho\left(1 - (\boldsymbol{m}\cdot\boldsymbol{t})^2\right), \tag{2.6}$$

with $\rho_0 = \rho_\perp$ corresponding to the resistivity of the NM itself and $\Delta\rho = \rho_\parallel - \rho_\perp$ corresponds to the SMR-induced resistivity change ($\rho_\perp$ and $\rho_\parallel$ designate the NM's resistances for $\boldsymbol{j}_{\mathrm{c}} \perp \boldsymbol{m}$ and $\boldsymbol{j}_{\mathrm{c}} \parallel \boldsymbol{m}$, respectively). For $g_{\mathrm{i}}^{\uparrow\downarrow} \ll g_{\mathrm{r}}^{\uparrow\downarrow}$, the resistance change can be related to the microscopic parameters as [48, 50]:

$$\frac{\Delta\rho}{\rho_0} = \frac{\theta_{\mathrm{SH}}^2(2\lambda_{\mathrm{s}}^2\rho_{\mathrm{NM}})(t_{\mathrm{NM}})^{-1}g_{\mathrm{r}}^{\uparrow\downarrow}\tanh(\frac{t_{\mathrm{NM}}}{2\lambda_{\mathrm{s}}})}{\frac{h}{2e} + 2\lambda_{\mathrm{s}}\rho_{\mathrm{NM}}g_{\mathrm{r}}^{\uparrow\downarrow}\coth(\frac{t_{\mathrm{NM}}}{\lambda_{\mathrm{s}}})}, \tag{2.7}$$

where ρ_{NM}, t_{NM} and λ_{s} correspond to the resistivity, thickness and spin diffusion length of the NM, respectively. As for the requirements of this thesis, the SMR effect was employed as a powerful probe for characterizing the SHE efficiency of different NMs deposited onto distinct yttrium iron garnet (YIG) films. The SMR amplitude essentially depends on θ_{SH}, λ_{s}, $g^{\uparrow\downarrow}$ and is therefore strongly depending on the quality of the NM/MOI interface and the general fabrication process quality. By conducting SMR measurements, it is thus possible to characterize the injection of SHE-induced spin currents in the MOI for a particular NM/MOI interface (thereby taking into account θ_{SH}, λ_{s} and $g^{\uparrow\downarrow}$), which is of significant importance for the measurements in Chap. 5. Let us point out that the description of SMR, as offered above, is completely valid only for the zero-temperature limit, whereas finite temperature effects affecting the SMR will be discussed in Chap. 4.

2.4 Magnon Transport

By patterning NM/MOI bilayers with two finite-distanced electrodes, as depicted in Fig. 2.5, we are able to harness the insulating nature of the MOI to the point where transport of angular momentum is enabled by *magnons*, rather than by moving charge carriers. As we are going to elucidate in the following, a charge current applied to the left (injector) electrode causes a spin accumulation at the NM/MOI interface, subsequently generating magnons in the MOI. These non-equilibrium magnons tend to diffuse in the MOI, eventually arriving at the right (detector) electrode, where we can detect the magnon diffusion current by means of the ISHE. Magnon transport, as described here, was first theoretically proposed by Zhang and Zhang [56, 57], experimentally achieved by Cornelissen et al. [22] and confirmed by Goennenwein et al. [23].

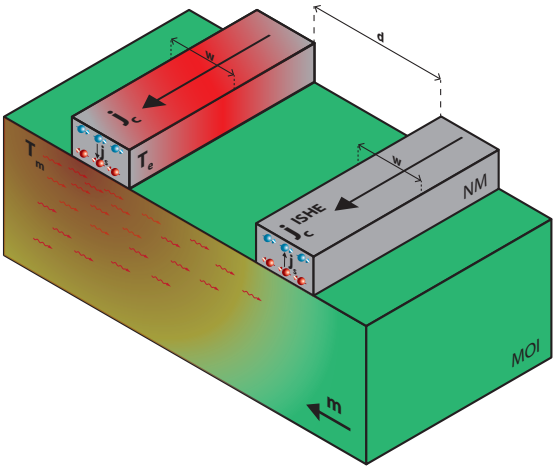

Fig. 2.5: Schematic illustration of a NM/MOI bilayer structure with two electrically isolated electrodes. Applying a charge current $\boldsymbol{j}_{\mathrm{c}}$ to the left electrode (injector), will give rise to a transverse SHE-induced spin current $\boldsymbol{j}_{\mathrm{s}}$ and increase the electronic system's temperature to T_{e} due to Joule heating. The SHE-induced spin accumulation at the interface either excites or annihilates magnons in the MOI, depending on the direction of $\boldsymbol{j}_{\mathrm{c}}$, whereas the mismatch of T_{e} and T_{m}, the latter being the temperature of the magnon system, at the interface, excites magnons due to the spin Seebeck effect (SSE) for arbitrary direction of $\boldsymbol{j}_{\mathrm{c}}$. The non-equilibrium magnon accumulation μ_m causes a magnon spin diffusion current in the MOI, which induces a spin accumulation at the second NM/MOI interface, that can be detected at the electrode (detector) via the ISHE. Adapted from Ref. [29].

Contrary to metallic systems, where spin currents are constituted of moving charges, as described in Chap. 2.1, spin currents in magnetic insulators are referred to as spin waves. Due to the strong exchange interaction in these materials, a local perturbation of the magnetic order

leads to high frequency dynamic vibrations of the spin system, with frequencies in the GHz- or even THz-regime [34]. For an accumulation of coupled electron spins ($\hbar/2$), a single magnon excitation could be portrayed as the inversion of a single spin state ($\hbar/2 + \hbar/2 = \hbar$), but spread across multiple localized spins. Each of those localized spins is then slightly tilted with respect to the others, with the spin flip event being prevailed on a length scale defined by the wavelength (energy) of the magnon.

As already stated, a charge current applied to the NM injector will cause a magnon diffusion current in the MOI. The exact mechanism of the magnon generation is, however, a synergy of multiple effects. In order to discuss this matter in more detail, it is important to properly define the total spin current flowing across the NM/MOI interface for finite temperatures [58]:

$$\boldsymbol{j}_{\mathrm{s,int}} = \frac{1}{4\pi}\left(\tilde{g}_{\mathrm{i}}^{\uparrow\downarrow} + \tilde{g}_{\mathrm{r}}^{\uparrow\downarrow}\boldsymbol{m}\times\right)\left(\boldsymbol{\mu}_{\mathrm{s}}\times\boldsymbol{m} - \hbar\dot{\boldsymbol{m}}\right) + \left[g(\mu_{\mathrm{m}} + \boldsymbol{\mu}_{\mathrm{s}}\cdot\boldsymbol{m}) + S_{\mathrm{c}}(T_{\mathrm{m}} - T_{\mathrm{e}})\right]\boldsymbol{m}, \tag{2.8}$$

where the direction of $\boldsymbol{j}_{\mathrm{s,int}}$ designates the spin polarization of the spin current (the current itself is flowing across the interface- perpendicular to it). $\tilde{g}_{\mathrm{r}}^{\uparrow\downarrow}$ and $\tilde{g}_{\mathrm{i}}^{\uparrow\downarrow}$ correspond to the real and imaginary part of the effective spin mixing conductance $\tilde{g}^{\uparrow\downarrow}$, which is the finite-temperature correction of the spin mixing conductance $g^{\uparrow\downarrow}$ defined in Chap. 2.3. The spin conductance g represents a measure of the interface spin transparency [59, 56, 57] at finite temperatures for $\boldsymbol{s} \parallel \boldsymbol{m}$, whereas S_{c} denotes the spin Seebeck coefficient which is associated with thermally driven currents due to the temperature difference of the magnonic T_{m} and electronic T_{e} bath.

Let us now briefly discuss all individual terms given in Eq. 2.8. The contributions related to $\boldsymbol{\mu}_{\mathrm{s}}\times\boldsymbol{m}$ were already explained for the zero-temperature case in Chap. 2.3. We recall that this term is finite for $\boldsymbol{m} \perp \boldsymbol{\mu}_{\mathrm{s}}$, giving rise to torques, which are perpendicular to $\boldsymbol{m}$. This will lead to excitation of transverse spin excitations, which will dephase on a short lengthscale. The terms associated with the time derivative $\dot{\boldsymbol{m}}$ reflect the spin pumping contributions as a consequence of coherent precession of the magnetization $\boldsymbol{M}$ [60, 61, 62]. For the SHE-induced magnon transport considered within this thesis, however, typically no coherent magnetization precession is excited and we can neglect this contribution.

The contribution proportional to g, on the other hand, reflects inelastic spin flip scattering events of the spin polarized electrons when $\boldsymbol{m} \parallel \boldsymbol{\mu}_{\mathrm{s}}$ [34, 58]. Hereby, the scattered electrons will release a part of their energy and, depending on the relative orientation of $\boldsymbol{\mu}_{\mathrm{s}}$ and $\boldsymbol{m}$, transfer their spin angular momentum to excite (parallel alignment of $\boldsymbol{\mu}_{\mathrm{s}}$ and $\boldsymbol{m}$) or absorb (antiparallel alignment of $\boldsymbol{\mu}_{\mathrm{s}}$ and $\boldsymbol{m}$) a magnon in the thermal spectrum. This will subsequently cause a non-equilibrium magnon accumulation or depletion, which is described by the magnon chemical potential μ_{m}. The non-equilibrium magnon accumulation/depletion will represent longitudinal spin waves (since parallel aligned with $\boldsymbol{m}$), and therefore contribute to the magnon transport at finite temperatures. We can understand the requirement for finite temperatures intuitively if we think of this process as a coupling of the electron spin accumulation to thermal fluctuations of the magnetization, rather than to the magnetization itself. Finally, the term associated with S_{c} is as well a finite temperature effect, since the temperature difference $T_{\mathrm{m}} - T_{\mathrm{e}}$ is required as the driving force. Furthermo-

re, we can deduce that this contribution, known as the spin Seebeck effect (SSE) [25, 63], is not depending on the relative orientation of $\boldsymbol{m}$ and $\boldsymbol{\mu}_\mathrm{s}$, giving rise to a spin polarization parallel to $\boldsymbol{m}$.

If we now apply these observations to our macroscopic picture, the contributions proportional to g will arise as a consequence of the SHE-induced spin accumulation at the interface. Furthermore, by switching the polarization of the current applied to the injector electrode, we can change between magnon accumulation and depletion for a fixed $\boldsymbol{m}$, due to the symmetry of the SHE (c.f. Eq. 2.3 and Fig. 2.3). Both scenarios will cause a non-equlibrium magnon chemical potential, therefore causing a finite magnon spin current to flow in the MOI. If the non-equilibrium magnons are able to reach the detector, an electron spin accumulation in the NM layer will be induced and subsequently detected via the ISHE, hence employing the SHE symmetry twice. Joule heating, emerging as the consequence of applying a charge current to a material with finite resistance, will cause magnon injection, as described by the SSE contribution. Since the heating-induced magnons are not depending on $\boldsymbol{\mu}_\mathrm{s}$, the symmetry of magnon transport due to thermally induced magnons will be governed by the ISHE at the detector only.

After introducing the injection and detection of magnons in a MOI via the (I)SHE in the preceeding paragraphs, we now describe the diffusive transport of a magnon accumulation μ_m in the MOI. Having an integer spin, magnons obey the Bose-Einstein statistics, and are therefore described by a bosonic distribution function [59] $f(\boldsymbol{r},\epsilon) = \left(\exp\left(\frac{\epsilon-\mu_\mathrm{m}(\boldsymbol{r})}{k_\mathrm{B}T_\mathrm{m}(\boldsymbol{r})}\right)-1\right)^{-1}$, with space-dependent magnon chemical potential $\mu_\mathrm{m}(\boldsymbol{r})$ and temperature $T_\mathrm{m}(\boldsymbol{r})$ [59]. Utilizing the Boltzmann transport theory approach, one can show that the magnon spin and heat currents in the MOI system are driven by gradients of the magnon chemical potential $\nabla\mu_\mathrm{m}$ and temperature ∇T_m, with the latter being characterized as a minor correction for sufficiently large lengthscales [34, 59]. Therefore, we can write the magnon spin diffusion equation as [34]:

$$D_\mathrm{m}\nabla^2\mu_\mathrm{m} = \frac{\mu_\mathrm{m}}{\tau_\mathrm{m}}, \tag{2.9}$$

where D_m and τ_m correspond to the magnon diffusion constant and the magnon lifetime, respectively. We can identify the magnon diffusion length as $\lambda_\mathrm{m} = \sqrt{D_\mathrm{m}\tau_\mathrm{m}}$. Taking into account the previously offered considerations about magnon transport in a MOI, we can, without loss of generality, reduce Eq. 2.9 to the 1D case to highlight the regimes of magnon transport. We discern between two limiting cases: the first one given by $d \ll \lambda_\mathrm{m}$ gives a spatial decay of the magnon current according to $1/(2d)$, corresponding to a diffusion similar to electron diffusion, without magnon spin relaxation, whereas the second one given by $d \gg \lambda_\mathrm{m}$ corresponds to an exponential decaying magnon current, governed by $\exp(-d/\lambda_\mathrm{m})$.

3 Experimental Details

Research conducted within this thesis was based on patterning metallic micro- and nanostructures onto the magnetic insulator yttrium iron garnet ($Y_3Fe_5O_{12}$), more commonly known as *YIG*, by means of electron beam litography and sputter deposition. In this Chapter we present details regarding the used materials (Chap. 3.1), furthermore describing the processes of sample fabrication (Chap. 3.2) and finally giving a brief overview of the different utilized measurement techniques (Chap. 3.3).

3.1 Material Systems

The magnetic insulator analysed in this thesis is the rare-earth iron garnet ferrimagnet $Y_3Fe_5O_{12}$. The Y^{3+} ions are dodecahedrally coordinated, while the Fe^{3+} ions are octahedrally (two ions: Fe^{a}) and tetrahedrally (three ions: Fe^{d}) coordinated to O^{2-} ions, as shown in Fig. 3.1 **(a)**. In total, YIG reassembles a body-centered-cubic (bcc) crystal structure, with the conventional unit cell containing 80 atoms (12 Y^{3+}, 8 $Fe^{3+(a)}$, 12 $Fe^{3+(d)}$ and 48 O^{2-} ions), corresponding to 4 molecular formulas of YIG [64]. Since the Y^{3+} and O^{2-} ions have completely filled shells, they only exhibit a weak diamagnetic contribution when an external magnetic field $\boldsymbol{H}$ is applied, showing no spontaneous magnetic moment. The magnetic character

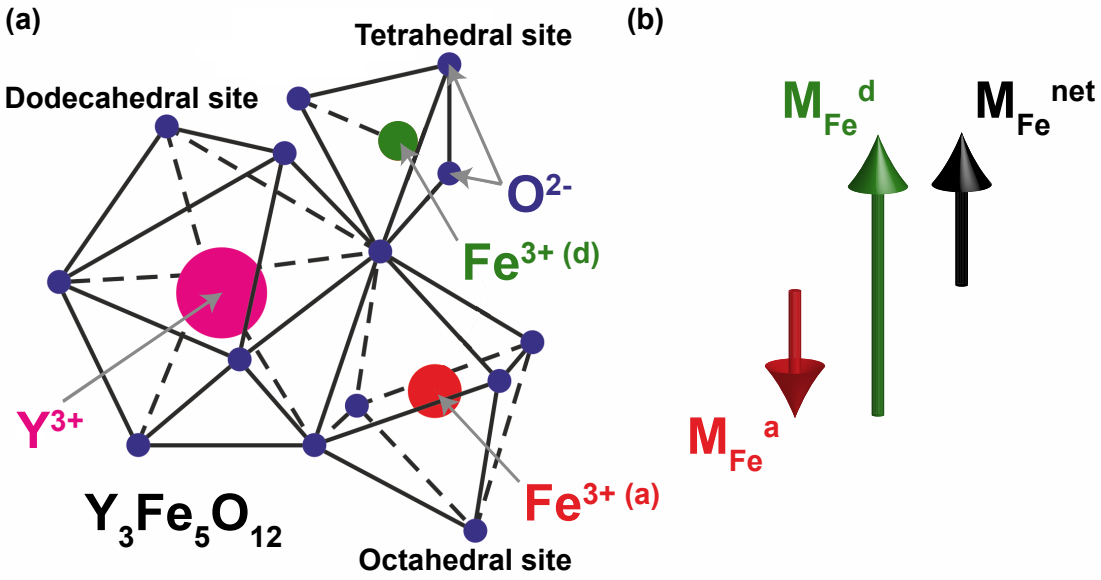

Fig. 3.1: (a) Schematic illustration of YIG crystal structure. The Y^{3+} ion (pink) occupies the dodecahedral site, whereas Fe^{3+} ions occupy the tetrahedral (green) or octahedral (red) site, all of them being coordinated to O^{2-} ions (purple). **(b)** Corresponding Fe sublattice magnetizations: $\boldsymbol{M}_{\mathrm{Fe}}^{\mathrm{d}}$ (green) and $\boldsymbol{M}_{\mathrm{Fe}}^{\mathrm{a}}$ (red) being the magnetizations of the tetrahedral and octahedral sites, respectively. Note that $\boldsymbol{M}_{\mathrm{Fe}}^{\mathrm{net}} \parallel \boldsymbol{H}$. Adapted from [65].

of YIG stems from the 3d electrons of the Fe^{3+} ions, with each ion carrying a magnetic moment of $5\mu_{\mathrm{B}}$. Within the individual magnetic sublattices, the moments are ferromagnetically exchange coupled, however, the antiferromagnetic superexchange coupling [66, 67] between the nearest $Fe^{3+(a)}$ and $Fe^{3+(d)}$ ions is predominant, causing a strong antiparallel coupling persisting up to very high external fields (above 250 T [68]) and temperatures

Metal	Z	$\rho(\Omega\,\mathrm{m})$	$\theta_{\mathrm{SH}}(\%)$	$\lambda_{\mathrm{sd}}(\mathrm{nm})$
Al (4.2 K)[43, 70]	13	$9.5 \cdot 10^{-8}$	0.032 ± 0.006	455 ± 15
Ti (295 K)[71]	22	$3.0 \cdot 10^{-6}$	-0.036 ± 0.004	≈ 13.3
Ru (4.2 K)[72]	44	$9.5 \cdot 10^{-8}$	$-$	≈ 14
Ta (295 K)[73]	73	$2.0 \cdot 10^{-6}$	-3 ± 1	1.5 ± 0.5
Ir (295 K)[74]	77	$2.5 \cdot 10^{-7}$	≈ 2	1.3 ± 0.1
Pt (295 K)[75]	78	$3.3 \cdot 10^{-7}$	11 ± 8	1.5 ± 0.5
Au (295 K)[76]	79	$4.9 \cdot 10^{-8}$	8.4 ± 0.7	≈ 60

Tab. 3.1: List of metals used for fabrication of the NM | YIG heterostructures, with indicated atomic number (Z), resistivity (ρ), SHE angle (θ_{SH}) and spin diffusion length (λ_{sd}).

($T_{\mathrm{c}} = 559\,\mathrm{K}$ [69]). This, hence allows approximating YIG with a ferromagnet with a net magnetization of $\boldsymbol{M}_{\mathrm{Fe}}^{\mathrm{net}} = \boldsymbol{M}_{\mathrm{Fe}}^{\mathrm{d}} + \boldsymbol{M}_{\mathrm{Fe}}^{\mathrm{a}}$, as depicted in Fig. 3.1 **(b)**, adding up to a net magnetic moment of $20\mu_{\mathrm{B}}$ per unit cell. The crystal's cubic symmetry is also reflected in its magnetic anisotropy. One must point out that only thin-film YIG crystals were used within this work, introducing an additional shape anisotropy which basically confines the magnetization within the sample's plane. Taking into consideration the perfected crystal growth method as well as the fact that YIG is best known for having the lowest spin-wave damping coefficient, it becomes clear why it became the material of choice when studying new phenomena in magnets [64].

This research focused on studying NM | YIG heterostructures. For that purpose we used 2 types of YIG samples: commercially available $2\,\mu\mathrm{m}$ thick YIG films grown via liquid phase epitaxy (LPE) on (111)-oriented Gadolinium-Gallium-Garnett (GGG) substrates and ultrathin YIG films ($\sim 10\,\mathrm{nm}$) grown at the Walther-Meißner-Institut (WMI) via pulsed laser deposition (PLD) on (100)-oriented GGG substrates. The thick LPE YIG films were used for the spin Hall magnetoresistance studies in Chap. 4, since they are commercially available providing multiple samples for this study. For the current induced modulation studies of magnon transport in Chap. 5 thin films grown by PLD were used, since the effects in current modulation only are detectable in the thin film limit. In order to enable differentiating between thermally and SHE induced effects, we used a variety of metals, featuring small or even vanishing spin Hall angles, thereby progressively reducing the SHE-induced contribution. The deposited metals among some properties are listed in Tab. 3.1.

3.2 Sample Fabrication

The aforementioned types of YIG samples were used with different objectives. In the following Chapters we are going to discuss this matter in detail, but for now it is important to note that we employed distinct fabrication methods for the individual samples. Nevertheless, the sample fabrication processes were specifically tailored to maximize the interface conversion of the electron spin current to a magnon spin current (and vice versa). This enables us to achieve the highest efficiency of the SHE/ISHE in the NM, thus allowing the usage of these effects for injection and detection of magnon waves in the magnetic insulator YIG. Therefore, we applied thin metallic films via sputter deposition on top of YIG, patterning them into micro- and nanostructures by utilization of electron beam lithography and lift-off techniques. Here, we summarize the different fabrication procedures by

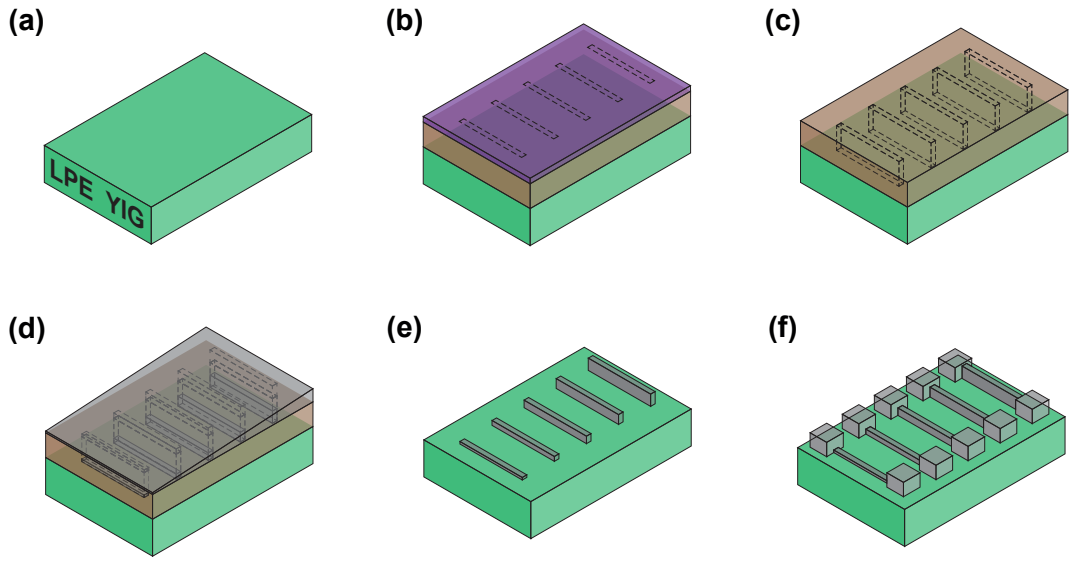

Fig. 3.2: Summary of fabrication process with wedge sputtering. **(a)** Prior fabrication the YIG film is extensively cleaned. **(b)** Resists are spin coated and baked out. **(c)** Written and developed sample. **(d)** Material deposited in wedge-form. **(e)** Lift-off. **(f)** Finalized sample.

	resist layers	spin coating	baking out	base dose	development time
alignment/ focus markers	PMMA/MA33% PMMA-Electra 92	1 min @ 4000 rpm 1 min @ 4000 rpm	2 min @ 170 °C 2 min @ 90 °C	$3\,\mathrm{Cm}^{-2}$	90 s
macrostructures (bondpads)	PMMA 600K PMMA-Electra 92	1 min @ 4000 rpm 1 min @ 4000 rpm	2 min @ 170 °C 2 min @ 90 °C	$4.85\,\mathrm{Cm}^{-2}$	120 s
nanostructures (bondpads)	PMMA 600K PMMA 950K PMMA-Electra 92	1 min @ 4000 rpm 1 min @ 4000 rpm 1 min @ 4000 rpm	5 min @ 170 °C 5 min @ 170 °C 2 min @ 90 °C	$5.6\,\mathrm{Cm}^{-2}$	120 s

Tab. 3.2: Summary of resists and lithography parameters used for the different types of structures.

describing a general fabrication process, step by step, and offer a more detailed overview subsequently.

Prior every lithography step, the YIG samples are cleaned with acetone and isopropanol (IPA) in an ultrasonic bath. The starting ultrasonic power level (i.e. for a blank sample) is put to maximal output, and gradually reduced for every successive step, in order to minimize damaging the previously fabricated structures. The sample is then blow-dried with nitrogen and spin-coated with multiple (distinct) resist layers and baked out on a hotplate after each coating. For achieving the optimal writing process in terms of avoiding surface charge accumulation (due to the fact that YIG is an insulator), the last coated resist layer is a conductive resist. Following the preparation, we install the sample into the *NanoBeam nB5* electron beam lithography system (*NanoBeam Ltd.*) which was used for the writing process. The used resists are so-called positive resists: the resist vanishes, after applying an appropriate developer, at a point where the surface was irradiated with the electron beam. After finishing the writing, the conductive resist is removed by rinsing the sample in dionized water ($\sim 20\,\mathrm{s}$) and the sample blow-dried. All samples are then developed in the *AR 600-56* developer and subsequently rinsed in IPA ($\sim 30\,\mathrm{s}$) with the aim of stopping

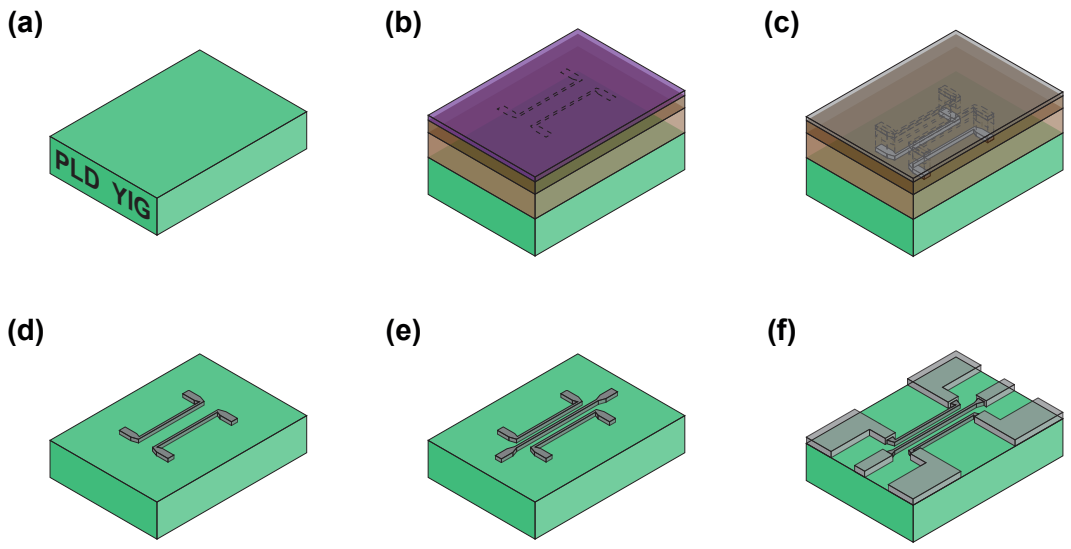

Fig. 3.3: Summary of nanostructures fabrication process. **(a)** Prior fabrication the YIG film is extensively cleaned. **(b)** Resist are spin coated and baked out. **(c)** Written and developed sample. **(d)** Patterned Pt injector and detector. **(e)** Patterned modulator. **(f)** Finalized sample.

the development process and removing unwanted residues of the resist. The sample is hereby prepared for the sputter deposition. For removing the unwanted sputtered material we apply a lift-off technique. The sample is therefore submerged in a previously heated up ($\sim 70\,^{\circ}\mathrm{C}$) acetone bath for at least $15\,\mathrm{min}$ and gently pipetted to support the process. Finally, we put the sample into the ultrasonic bath at the lowest power level for few short bursts only, in order to remove any potential unwanted metallic remains. Hereby, one patterning step, as illustrated in Fig. 3.4, is completed. The specific lithography parameters for the used resists are listed in Tab. 3.2.

The entire fabrication process of the samples consists of four patterning steps. In the first step we pattern $\sim 45\,\mathrm{nm}$ thick platinum (Pt) markers, which are used for focusing the electron beam as well as for the alignment of the structures patterned in the following steps. In the second step we pattern pure Pt structures, whereas in the third step we pattern one/multiple other metallic films. Finally, we pattern $\sim 50\,\mathrm{nm}$ thick aluminum (Al) lead and bonding pads, which are allowing to connect the structures electrically. The fabrication of the two sample types differed in terms of the 3^{rd} and 4^{th} step. For the microstructures sputtered onto the LPE-grown YIG samples, we utilized the so called wedge sputtering technique: the wedge shutter (i.e. the shutter covering the sample

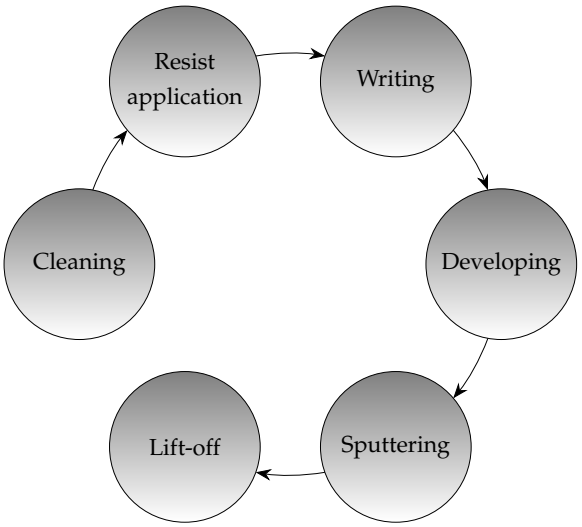

Fig. 3.4: Scheme illustrating one patterning step.

prior/after the deposition process which is normally used to prevent unwanted deposition) was gradually opened during the material deposition process, causing a thickness gradient in the structures, thus allowing thickness-dependent measurements on one sample. This was done for pure Pt (3^{rd} step) and with different alloys of Pt and gold (Au) (4^{th} step), each of them being patterned in a distinct row. The fabrication process is summarized in Fig. 3.2. For the nanostructures sputtered onto the PLD-grown YIG samples, we patterned $\sim 5\,\mathrm{nm}$ thick Pt devices for injection/detection of spin waves (3^{rd} step), whereas different metallic films of equal thickness were patterned in order to extensively investigate magnon transport properties (4^{th} step). Additionally, pure Pt structures with two and three strips were patterned for reference devices. This fabrication process in illustrated in Fig. 3.3.

3.3 Setup and Measurement Techniques

Upon completing the fabrication, the samples are glued onto a chip carrier and connected to its Copper (Cu) contacts by Al-wire bonding, as shown in Fig. 3.5. We then install the sample on a dipstick, which is inserted into a superconducting magnet cryostat. Even though the magnet itself is operated at very low temperatures, the so-called variable temperature insert (VTI), where the sample resides within the cryostat, allows to set the sample's temperature within the range of $2\,\mathrm{K} \leq T_{\mathrm{sample}} \leq 300\,\mathrm{K}$ with a $\pm 10\,\mathrm{mK}$ precision. The measurements are conducted with two different superconducting magnet cryostat setups at the Walther-Meißner-Institut: a 1D magnet with a field strength of up to $\mu_0 H = 7\,\mathrm{T}$ with the possibility to rotate the sample by utilizing an electronic stepper motor, and a 3D-vector magnet reaching magnetic field strengths of up to $\mu_0 H = 2.5\,\mathrm{T}$ and $\mu_0 H = 6\,\mathrm{T}$, in the horizontal plane and in the vertical direction, respectively. Therefore, both setups are well suited for angle dependent measurement, being the main type of measurements performed in this thesis. For the SMR measurements (Chap. 4), we apply a DC charge current to the electrode and measure the voltage drop along it (c.f. Fig. 3.5 **(a)**). For the magnon transport measurements (Chap. 5), we apply either a DC or an AC charge current I_{inj} to the injector electrode and measure the voltage output at the detector electrode (c.f. Fig. 3.5 **(b)**). Additionally, a DC charge current I_{mod} is applied to the modulator electrode. Note that in the case of the DC-type magnon transport measurements, we are able to simultaneous-

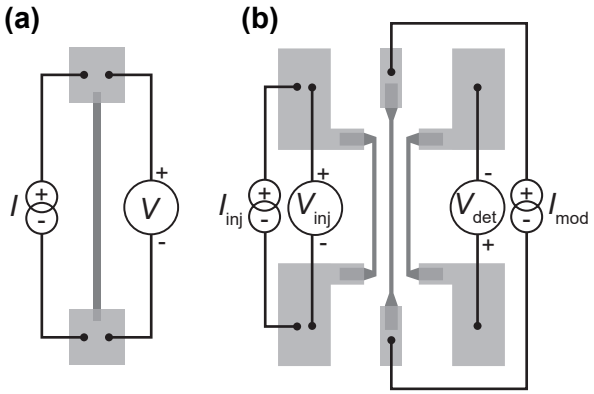

Fig. 3.5: Schematic illustration of patterned and contacted structures. **(a)** The microstructures are patterned into strips of $940\,\mu\mathrm{m}$ length and $20\,\mu\mathrm{m}$ width. **(b)** The nanostructure devices consist of three electrodes: injector, modulator, detector (going from left to right). Injector/detector are $50\,\mu\mathrm{m}$ long, $500\,\mathrm{nm}$ wide and $5\,\mathrm{nm}$ thick, whereas the modulator strips are $64\,\mu\mathrm{m}$ long, with widths ranging from $100\,\mathrm{nm}$ to $1000\,\mathrm{nm}$ and thicknesses ranging from $5\,\mathrm{nm}$ to $15\,\mathrm{nm}$.

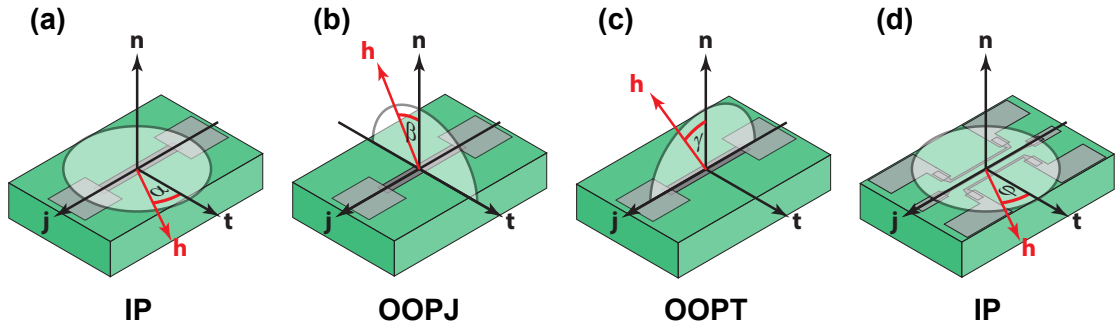

Fig. 3.6: Schematic illustration of the three orthogonal magnetic field rotation planes. **(a)** The external field is rotated in the thin film plane (IP). **(b)** The field is rotated out of plane around the **j**-axis (OOPJ) **(c)** The field is rotated out of plane around the **t**-axis (OOPT). **(d)** IP rotation for a three strip structure.

ly conduct SMR measurements at the injector electrode. Depending on the superconducting magnet cryostat setup, the angle dependent magnetoresistance and magnetotransport measurements are performed either by rotating the sample within a static external magnetic field (1D magnet setup) or by rotating the external magnetic field around the sample (3D magnet setup), with both approaches yielding the same result. Furthemore, we define three mutually orthogonal rotation planes, as depicted in Fig. 3.6.

Due to the small scales of our devices, applying charge currents of the order of magnitude of $100\,\mu\mathrm{A}$ results in relatively high current densities ($j_{\mathrm{inj}} \sim 10^{10}\mathrm{Am}^{-2}$), giving rise to both electrically (SHE) and thermally induced magnons. In order to be able to distinguish between the contributions from electrically and thermally excited effects, we employ two different measurement techniques based on application of AC (Chap. 3.3.2) and DC (Chap. 3.3.1) currents to the injector, both being well suited for investigation of magnon transport [77].

3.3.1 DC Current Reversal Method

The DC current reversal method was initially used for SMR measurements of devices shown in Fig. 3.2. Let us therefore start by considering a device contacted as illustrated in Fig. 3.5 **(a)**. The method itself, as the name suggests, is comprised of applying DC currents of positive ($+I$) and negative ($-I$) polarity subsequently to the device. The corresponding voltage drops $V^+ = V(+I)$ and $V^- = V(-I)$ are recorded simultaneously. This allows us to harness the symmetries of the electrical and thermal effects in order to differentiate between the corresponding contributions. The electrical voltage contribution switches sign upon polarity change (i.e. V^{el} is proportional to odd powers of I), whereas the thermal voltage contribution is insensitive to the polarity change of the current (i.e. V^{el} is proportional to even powers of I). Therefore, we can calculate the individual contributions as:

$$V^{\mathrm{el}} = \frac{V^+ - V^-}{2} \tag{3.1}$$

$$V^{\mathrm{therm}} = \frac{V^+ + V^-}{2}. \tag{3.2}$$

The measurement method was then adapted for the nanodevices (Fig. 3.3), contacted as depicted in Fig. 3.5 **(b)**. In case of measurements without applied current at the modulator ($I_{\mathrm{mod}} = 0$), or for reference devices without the modulator electrode, we can fully adapt Eqs. 3.1 and 3.2 for magnetoresistance voltage measurements (c.f. Chap. 2.3) at the injector as well as for magnon transport voltage measurement (c.f. Chap. 2.4) at the detector:

$$V_{\mathrm{inj/det}}^{\mathrm{el}} = \frac{V_{\mathrm{inj/det}}^{+} - V_{\mathrm{inj/det}}^{-}}{2} \tag{3.3}$$

$$V_{\mathrm{inj/det}}^{\mathrm{therm}} = \frac{V_{\mathrm{inj/det}}^{+} + V_{\mathrm{inj/det}}^{-}}{2}. \tag{3.4}$$

By this we established an adequate procedure for distinguishing between thermal and electrical voltage contributions at injector and detector. We now want to utilize the modulator electrode (c.f. Chap. 5.1.1) in order to manipulate the magnon transport between injector and detector via an additional SHE-induced and thermal injection of magnons. However, by applying a finite DC current at the modulator ($I_{\mathrm{mod}} \neq 0$), we will also alter the signal at the detector by superimposing an additional contribution stemming from the modulator electrode. Since we want to measure the change of magnon conductance for the signal originating from the injector exclusively, we must account for the signal emerging from the modulator. This is done by refining the current reversal method by introducing an additional measurement point for zero current at the injector. The applied current sequence at the injector becomes $+I_{\mathrm{inj}}, 0, -I_{\mathrm{inj}}$, with the corresponding voltages $V_{\mathrm{det}}^{+}, V_{\mathrm{det}}^{0}, V_{\mathrm{det}}^{+}$, measured at the detector [1)]. Finally, we obtain:

$$V_{\mathrm{det}}^{\mathrm{el}} = \frac{(V_{\mathrm{det}}^{+} - V_{\mathrm{det}}^{0}) - (V_{\mathrm{det}}^{-} - V_{\mathrm{det}}^{0})}{2} = \frac{V_{\mathrm{det}}^{+} - V_{\mathrm{det}}^{-}}{2} \tag{3.5}$$

$$V_{\mathrm{det}}^{\mathrm{therm}} = \frac{(V_{\mathrm{det}}^{+} - V_{\mathrm{det}}^{0}) + (V_{\mathrm{det}}^{-} - V_{\mathrm{det}}^{0})}{2} = \frac{V_{\mathrm{det}}^{+} + V_{\mathrm{det}}^{-}}{2} - V_{\mathrm{det}}^{0}. \tag{3.6}$$

The right hand sides of Eqs. 3.5 and 3.6 hold only if the characteristic current sequence is applied to the injector for a constant modulator current. We see that in this case the electrical contribution from the modulator will be filtered out automatically, whereas the modulator's thermal contribution needs to be subtracted by hand. Furthermore, in order to increase precision we repeat the measurement 5 times for every external parameter setting. The final values for both contributions are obtained by taking the arithmetic mean of the 5 measurement sequences. As for the instruments, we used Keithley 2400 Sourcemeters to feed currents through the devices, with typically measuring the voltage at the injector and modulator with Keithley 2010 Multimeters and the voltage at the detector with Keithley 2182 Nanovoltmeter.

3.3.2 AC Lock-In Detection

In case of the AC- readout technique, we apply an AC stimulus to the injector, rather than sequences of DC currents, while a constant DC current is applied to the modulator simul-

[1)] T. Wimmer proposed the name Current Staggering.

taneously (Fig. 3.5 **(b)**). The frequency-sensitive voltage feedback at the detector is then measured via a lock-in detection scheme, allowing to filter out the direct modulator contribution. In order to minimize the capacitive and inductive coupling between the nanostrips, which might overcast the magnon transport signals, we used very low frequency currents $\sim 7\,\mathrm{Hz}$. Furthermore, the frequency f was chosen such that $n \cdot f \neq m \cdot 50\,\mathrm{Hz}$ ($m, n \in \mathbb{N}$), assuring that it does not coincide with multiples of the frequency of the AC power outlet [34]. In particular, a sinusoidal shaped AC current $I_{\mathrm{inj}}(t) = I_0 \sin(\omega t)$ was applied to the injector, with $\omega = 2\pi f$ and the injected current amplitude I_0. This will subsequently give rise to a voltage at the detector, oscillating with the same frequency, due to electrical and thermal magnon transport driven by $I_{\mathrm{inj}}(t)$. As for the previous method, we want to obtain the ability to differentiate between the thermal and electrical effects. For this purpose, we can, without loss of generality, write the measured voltage response $V_{\mathrm{det}}(t)$ at the detector as an expansion with respect to the injector current $I_{\mathrm{inj}}(t)$:

$$V_{\mathrm{det}}(t) = \sum_{i=1}^{\infty} R_{\mathrm{i}} I_{\mathrm{inj}}^{\mathrm{i}}(t) = R_1 I_{\mathrm{inj}}(t) + R_2 I_{\mathrm{inj}}^2(t) + \mathcal{O}(I_{\mathrm{inj}}^3(t)). \tag{3.7}$$

Here, R_{i} are the transport coefficients carrying information about the conversion processes at the injector/YIG and YIG/detector interfaces as well as the transport in the YIG layer. Note that in the right hand side of Eq. 3.7 we consider powers of the detector current up to second order only, since the higher order contributions can be neglected for sufficiently small injector currents. The lock-in detection method allows us to measure an arbitrary n^{th} harmonic voltage signal $V^{\mathrm{n}\omega}$ in form of two components. This is achieved by first multiplying $V_{\mathrm{det}}(t)$ with two sinusoidal reference signals mutually shifted by $90°$ (i.e. $V_0^{\mathrm{ref}} \sin(n\omega t)$ and $V_0^{\mathrm{ref}} \cos(n\omega t)$), one at a time, and subsequently integrating the multiplied signals over a time interval T much larger than the oscillation period of $I_{\mathrm{inj}}(t)$ (i.e. $T \gg 1/f$). We obtain $V^{\mathrm{n}\omega}$ as:

$$V_{\mathrm{X}}^{\mathrm{n}\omega} = \frac{\sqrt{2}}{T} \int_t^{t+T} V_0^{\mathrm{ref}} \sin(n\omega t') V_{\mathrm{det}}(t') \mathrm{d}t' \tag{3.8}$$

$$V_{\mathrm{Y}}^{\mathrm{n}\omega} = \frac{\sqrt{2}}{T} \int_t^{t+T} V_0^{\mathrm{ref}} \cos(n\omega t') V_{\mathrm{det}}(t') \mathrm{d}t' \tag{3.9}$$

Inserting Eq. 3.7 into Eqs. 3.8 and 3.9, yields for the first two harmonic voltages:

$$V_{\mathrm{X}}^{1\omega} = I_1 R_1 \cos(\phi) \qquad V_{\mathrm{Y}}^{1\omega} = I_1 R_1 \sin(\phi) \tag{3.10}$$

$$V_{\mathrm{X}}^{2\omega} = I_1^2 R_2 \sin(2\phi) \qquad V_{\mathrm{Y}}^{2\omega} = I_1^2 R_2 \cos(2\phi). \tag{3.11}$$

It has become obvious that the first (Eqs. 3.10) and second (Eqs. 3.11) harmonic voltage signals correspond to effects that are odd and even under current reversal, respectively, thereby allowing to differentiate between electrical and thermal effects in magnon transport measurements.

Furthermore, it is possible to transform the measured signals so that the full signal re-

sponse emerges in only one of the components. This is achieved by applying a rotation matrix to our signals:

$$\begin{pmatrix} V_{\mathrm{X}'}^{\mathrm{n}\omega} \\ V_{\mathrm{Y}'}^{\mathrm{n}\omega} \end{pmatrix} = \begin{pmatrix} \cos(n\phi) & -\sin(n\phi) \\ \sin(n\phi) & \cos(n\phi) \end{pmatrix} \begin{pmatrix} V_{\mathrm{X}}^{\mathrm{n}\omega} \\ V_{\mathrm{Y}}^{\mathrm{n}\omega} \end{pmatrix} \tag{3.12}$$

Here, we need to point out that the phase ϕ is determined iteratively, by applying the rotation matrix to the harmonic voltages for different values of ϕ until the signal appears in only one component. We used a Zurich Instruments HF2LI $50\,\mathrm{MHz}$ Lock-In Amplifier to simultaneously record the first and second harmonic voltage at the detector, combined with a SR560 Low Noise Preamplifier in order to amplify the voltage signals. The AC current at the injector is generated by a Keithley 6221 DC and AC Current Source, which was triggered by the Lock-In.

4 Spin Hall Magnetoresistance in NM | YIG Heterostructures

This Chapter focuses on magnetoresistance measurements of NM/YIG heterostructures with NMs of different spin-Hall efficiency (c.f. Tab. 3.1). In particular, we conducted SMR (c.f. Chap. 2.3) measurements by means of angle-dependent magnetoresistance (ADMR) measurements [75], as illustrated in Fig. 3.6. Quantities like the spin-Hall angle θ_{SH}, spin diffusion length λ_{s} and the spin mixing conductance $g^{\uparrow\downarrow}$ are crucial parameters when it comes to SMR [50, 75], as well as for magnon transport measurements [59, 16]. However, obtaining the values of these quantities is not straightforward, since they are strongly influenced by the heterostructure's composition, its interface properties and external parameters. SMR measurements are, thus, a very powerful probe for the overall efficiency of spin injection into a magnetic insulator (magnon generation) by means of the SHE [22]. Therefore, we employed the SMR in order to characterize the spin Hall physics of the used metals, granting us a more complete overview for the magnon transport measurements discussed in Chap. 5.

One of the major motivations for the work discussed in this Chapter are based on recent publications [78, 79], which claim to have achieved a giant spin Hall angle and an enormous enhancement of the spin-orbit torque efficiency for $\mathrm{Pt}_{1-\mathrm{x}}\mathrm{Au}_{\mathrm{x}}$ alloys. In order to verify these results, we fabricated samples with PtAu alloy devices of different thickness (Fig. 3.2) on top of LPE-grown films. The measurements were conducted for fields and temperatures ranging from $0.1\,\mathrm{T}$ to $7\,\mathrm{T}$ and $5\,\mathrm{K}$ to $300\,\mathrm{K}$, respectively. The results of these measurements are then compared to SMR measurements of nanodevices fabricated on top of PLD-grown films which were used for the magnon transport experiments presented in Chap. 5.

All measurements presented in this Chapter are conducted by utilizing the DC current reversal method (c.f. Chap. 3.3.1), with a current of $100\,\mu\mathrm{A}$ being applied to the device. The field orientation has been rotated over the full accessible angle range forwards and backwards, in order to check for reproducibility and possible hysteresis effects.

4.1 Angle-dependent Magnetoresistance Measurements in PtAu Alloys

For the purpose of characterizing the spin-Hall-activity of $\mathrm{Pt}_{1-\mathrm{x}}\mathrm{Au}_{\mathrm{x}}$ alloys, we patterned devices with $x = 0.1$ and $x = 0.25$ on two LPE YIG samples, together with additional reference Pt devices on the same samples. After completing the preparation process and contacting the devices (c.f. Fig. 3.5 (a)), we measured the voltage drop along the device while rotating the external magnetic field, and finally extracted the electrical voltage contribution (c.f. Eq. 2.3). As explained in Chap. 2.3, the relative orientation of the YIG magnetization $\boldsymbol{M}$ and the SHE-induced spin accumulation $\boldsymbol{\mu}_{\mathrm{s}}$ in the NM controls the boundary condition for the injection of spin currents from the NM into YIG, which can be varied by rotating the external magnetic field (assuming the magnetization is always aligned with the external magnetic field, which is valid for large enough external magnetic fields). Let us start by examining Fig. 4.1, which shows the electrical voltage contribution V^{el} as a function of α, corresponding to the angle between the external field $\boldsymbol{H}$ and the $\mathbf{t}$-direction. The data is obtained from in-plane rotations of an $18\,\mathrm{nm}$-thick $\mathrm{Pt}_{0.75}\mathrm{Au}_{0.25}$ device. We will start by assigning the characteristic features of the measurements, as well as describing the process of normalizing the data. The direction of the spin accumulation $\boldsymbol{\mu}_{\mathrm{s}}$ is predetermined by the

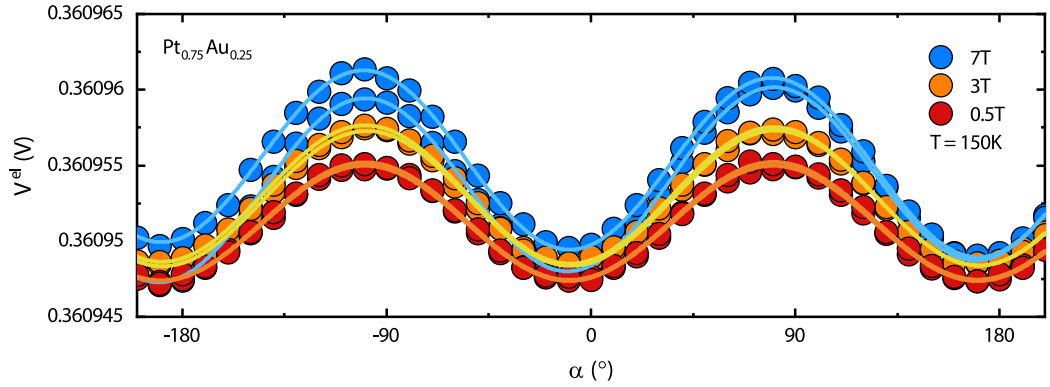

Fig. 4.1: Electric contribution of angle-dependent magnetoresistance measurements for three different fields at $150\,\mathrm{K}$ of a $\mathrm{Pt}_{0.75}\mathrm{Au}_{0.25}$ device grown on LPE YIG. The solid lines indicate the fits to Eq. 4.1.

charge and thus spin current direction as well as the sign of the spin Hall angle according to the SHE symmetry (c.f. Eq. 2.3). In our case, $\boldsymbol{\mu}_\mathbf{s}$ points along **t** and -**t** for positive and negative charge currents, respectively, considering a spin current flowing across the NM/YIG interface and a positive spin Hall angle (c.f. Figs. 2.3 and 2.4). For $\alpha = 0, \pm 180°$, $\boldsymbol{M}$ and $\boldsymbol{\mu}_\mathrm{s}$ are aligned parallel and the spin accumulation cannot exert a spin-orbit torque (SOT) on the magnetization, thereby only a small spin current can flow trough the NM/YIG interface (the finite spin current for $T > 0$ is a consequence of magnon excitation, c.f. Chap. 2.4). On the other hand, for $\alpha = \pm 90°$, $\boldsymbol{M}$ and $\boldsymbol{\mu}_\mathrm{s}$ are perpendicular to each other and hence the spin accumulation exerts maximal SOT on the magnetization - a finite spin current will flow across the interface (this will cause reduction of the ISHE-induced charge current, resulting in an increase of the voltage, c.f. Chap. 2.3). In between these two limiting cases, the torque will be governed by the projection of $\boldsymbol{\mu}_\mathrm{s}$ onto $\boldsymbol{M}$. Taking into account the $180°$ periodicity of the effect, we obtain a $\cos^2(\alpha)$ shape[2)]. Due to imperfect alignment (e.g. slightly rotated sample), we see a finite deviation of the curve's minima and maxima from $(0, \pm 180°)$ and $(\pm 90°)$, respectively. The slight asymmetry between the forth and back rotations, as well as between the two maxima and minima for both rotations is a consequence of thermal drift, causing a linear change in the NM's resistance, thus altering the voltage. In order to subtract the thermal drift contribution and account for the sample's misalignment, we fit the following function to our data for each rotation direction separately:

$$V^{\mathrm{el}} = V_0 + k_\mathrm{T}\alpha + \Delta V \cos^2(\alpha - \alpha_0). \tag{4.1}$$

Here, V_0 is the offset which indicates the device's Ohmic resistance, k_T the slope of the thermal drift, ΔV the amplitude of the voltage change due to SMR and α_0 the aforementioned misalignment (depending on the measurement geometry also an additional $90°$ shift, as in the case of IP measurements, must be added to α). By comparing the fit parameters with Fig. 4.1, we can infer that, after subtracting the thermal drift, V_0 corresponds to the minima of the curve, whereas ΔV corresponds to the difference of the maximum voltage level and the minimum voltage level (hence amplitude). Finally, we can normalize the ADMR

[2)] Note the $90°$ offset due to the specific angle definition: $\cos^2(x \pm 90°) = \sin^2(x)$.

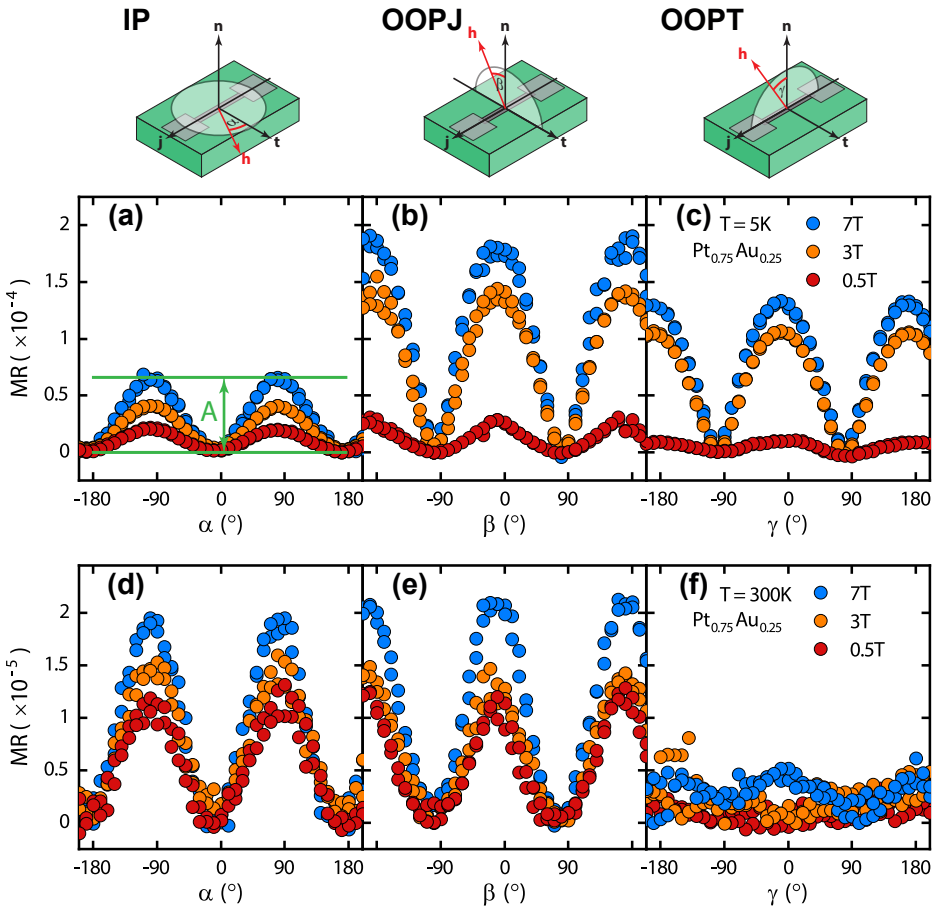

Fig. 4.2: Normalized ADMR measurements of an $18\,\mathrm{nm}$-thick $Pt_{0.75}Au_{0.25}$ device grown on LPE YIG. The upper (panels **(a)-(c)**) and lower (panels **(d)-(f)**) row correspond to measurements at $5\,\mathrm{K}$ and $300\,\mathrm{K}$, respectively, whereas the first, second and third column correspond to IP, OOPJ and OOPT measurements, respectively. The rotation geometry is indicated on top, and the normalized amplitude A is shown as an example for the $7\,\mathrm{T}$ measurements in **(a)**.

signals as:

$$\mathrm{MR} = \frac{V^{\mathrm{el}'}(\alpha) - V_0}{V_0}, \tag{4.2}$$

with:

$$V^{\mathrm{el}'}(\alpha) = V^{\mathrm{el}}(\alpha) - k_{\mathrm{T}}\alpha, \tag{4.3}$$

$$\mathrm{A} = \frac{\Delta V}{V_0}, \tag{4.4}$$

being the electric signal contribution after subtracting the thermal drift and the normalized amplitude of the magnetoresistance (MR), respectively.

Figure 4.2 shows the normalized SMR measurements for rotations in all three defined planes (IP, OOPJ, OOPT) for an $18\,\mathrm{nm}$-thick $Pt_{0.75}Au_{0.25}$ device. According to the established theory, we expect the IP and OOPJ measurements to show a $\cos^2(\alpha)$ modulation, as already described, with the only difference being the $90°$ shift due to the specific rotation angle definition. Furthermore, we expect to observe the same normalized amplitude for IP

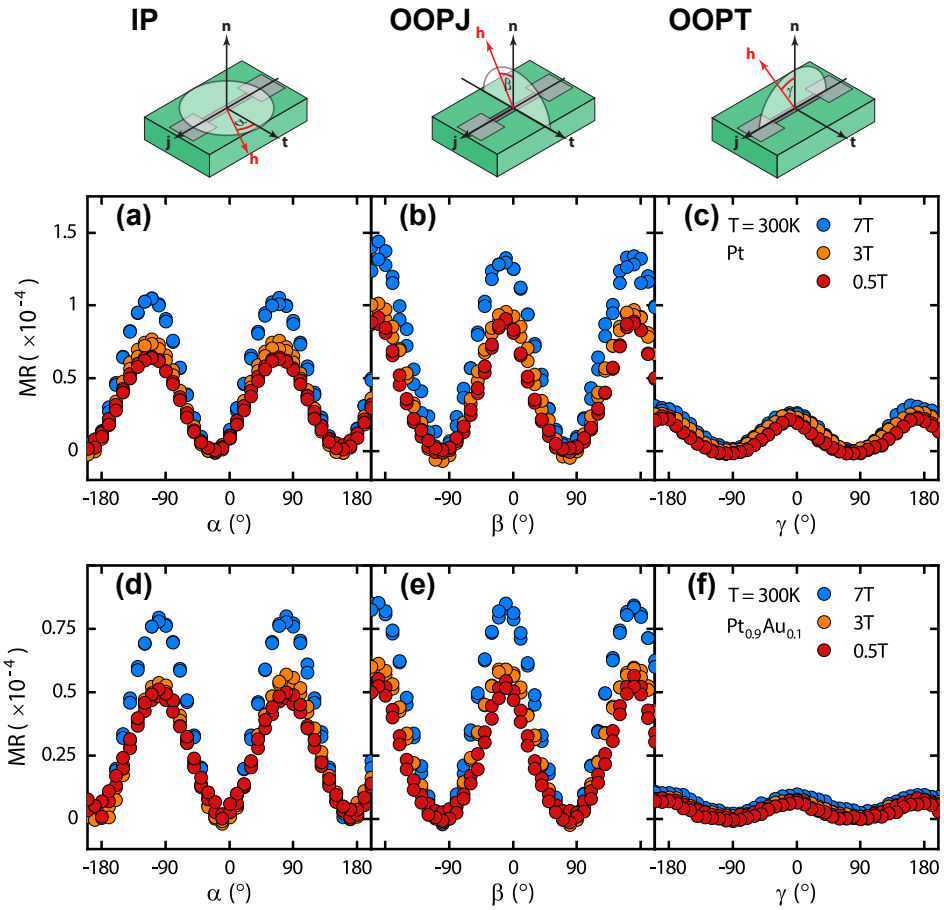

Fig. 4.3: Normalized ADMR measurements of a $12.5\,\mathrm{nm}$-thick Pt device (upper row, **(a)-(c)**) and a $13.25\,\mathrm{nm}$-thick $\mathrm{Pt_{0.9}Au_{0.1}}$ device (lower row, **(d)-(f)**) grown on LPE YIG. The first, second and third column correspond to IP, OOPJ and OOPT measurements, respectively. The rotation geometry is indicated on top.

and OOPJ measurements. On the other hand, in the case of OOPT measurements, we expect to measure a constant high voltage level without any modulation, since the magnetization $\boldsymbol{M}$ points always perpendicular to the spin accumulation $\boldsymbol{\mu}_\mathrm{s}$ in this case. This would then correspond to a zero-normalized amplitude A (c.f. Eq. 4.4). The measurements, however, exhibit large deviations from the predictions. First of all, we observe an angle-dependent behavior in the OOPT configuration for measurements at $5\,\mathrm{K}$ (Fig. 4.2 **(c)**), with an amplitude two times as large as the IP amplitude (Fig. 4.2 **(a)**). Furthermore, the amplitude of the OOPJ (Fig. 4.2 **(b)**) measurement is significantly larger as the IP amplitude. Approximately, the amplitudes of the IP and OOPT measurements sum up to the OOPJ amplitude. The measurements at $300\,\mathrm{K}$ (Fig. 4.2 **(d)-(f)**) show a decrease of the OOPT signal of almost two orders of magnitude compared to the $T = 5\,\mathrm{K}$ case, however, a finite angle-dependent modulation is still present. The OOPJ amplitude shows a reduction of one order of magnitude, and the IP amplitude is reduced by factor two, with a slight difference between these two amplitudes persisting.

Similar results arise from measurements of $\mathrm{Pt_{0.9}Au_{0.1}}$, as well as Pt devices. We present normalized IP, OOPJ and OOPT SMR measurements for a $12.5\,\mathrm{nm}$-thick Pt and a $13.25\,\mathrm{nm}$-thick $\mathrm{Pt_{0.9}Au_{0.1}}$ device at $300\,\mathrm{K}$ in Fig. 4.3. Again, we observe an angle-dependent modulation of the OOPT signal, with the difference of the OOPJ and IP amplitudes approximately

corresponding to the OOPT amplitude. This effect was already observed in previous works [80, 81, 82], and we are going to offer a short overview of the possible explanations. The first expected and also most simple cause for the specific behavior in the OOPT measurements would be to assume that the sample it not perfectly aligned within the designated planes and therefore behaves according to a tilted rotation plane. As mentioned in Chap. 3, after finalizing the fabrication, the samples are glued onto chip carriers. This process surely introduces misalignment causing a slight in-plane rotation of the real **j**- and **t**-axes, as well as an out of plane deviation from the **n**-axis. This effect, however, could only account for an OOPT signal which would be smaller by at least one order of magnitude from the observed one. Furthermore, in that case, we would not expect a drastic reduction of the effect when increasing temperature (compare **(c)** and **(f)** from Fig. 4.2). Let us therefore consider an alternative approach for the case of an ordinary magnetoresistance (OMR): for an external field applied perpendicular to the NM an increase of the NM's resistance arises due to motion of the conduction electrons along curved trajectories, induced by the Lorentz force [83]. The observed MR in the OOPT configuration, having the same amplitude as the difference of the OOPJ and IP amplitudes is therefore in agreement with OMR, since we would expect the same signature (in terms of magnitude and angle dependence) in OOPJ and OOPT stemming from OMR. Nonetheless, OMR exhibits a $(\mu_0 H)^2$ dependence [123], which was not demonstrated, as we will see in Chap. 4.2. Finally, we discuss the possibility of anisotropic magnetoresistance (AMR) due to magnetic proximity effects (MPE). AMR is a phenomenon that occurs in ferromagnets in which the resistivity depends on the angle between the current and magnetization directions [84]. Despite not being a ferromagnetic material itself, Pt can still exhibit AMR, since it is possible to induce a ferromagnetic layer at the interface layer of an NM adjacent to a ferromagnetic material [85]. An AMR induced in that fashion could also offer an explanation of our observations: if we assume a negative AMR (decrease of resistance for $\boldsymbol{M} \parallel \boldsymbol{j}_\mathrm{c}$), we would expect to measure an angle-dependent modulation in the OOPT configuration, having the same signature as the observed signal. Furthermore, the SMR signal in the IP configuration would then be reduced, due to the counteracting AMR. Similar behaviour was demonstrated in Pt/YIG bilayers [86], however other studies [87] led to conflicting results. Hence, the most probable scenario is actually a combination of all three mentioned effects. This superposition unfortunately makes a quantitative extraction of the three different contributions rather tedious.

If we now compare the IP measurements of all three devices at $300\,\mathrm{K}$ (Figs. 4.2 **(d)** and 4.3 **(a)**, **(d)**) and disregard a contribution from AMR at these temperatures, it becomes obvious that the SMR amplitude is decreasing with increasing concentration of the Au component, being the highest for pure Pt. Even though the devices are not completely equal due to different thicknesses, we specifically chose these devices for comparison since they exhibit the highest SMR amplitudes combined with the lowest noise level, within the series of thickness dependent measurements. We can conclude that alloying Pt and Au does not yield higher spin-Hall activity compared to Pt, at least if done by co-sputtering on YIG films. It is important to state that the co-sputtering complicates the production of alloys with different concentrations, since it is difficult to precisely control the ratio of the components, without conducting further control experiments to determine the achieved composition. Furthermore, we assume that the deposition introduces many defects (especially the formation of

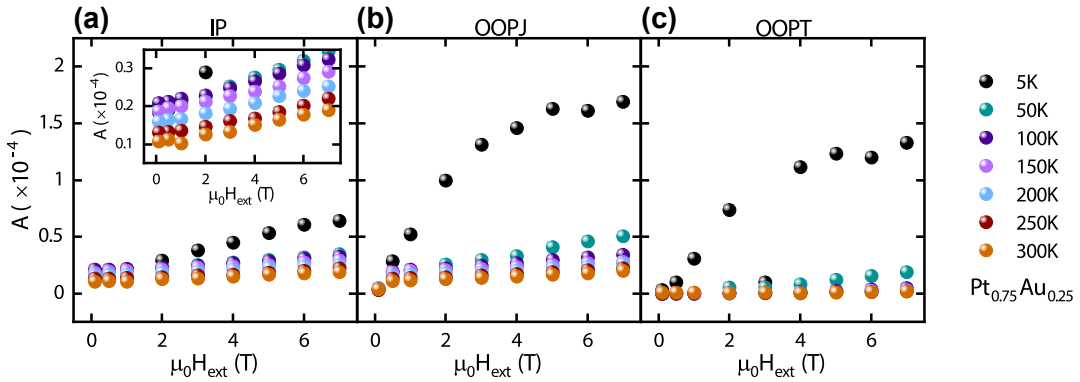

Fig. 4.4: Field dependence of MR for IP **(a)**, OOPJ **(b)** and OOPT **(c)** configurations of an $18\,\mathrm{nm}$-thick $\mathrm{Pt_{0.75}Au_{0.25}}$ device, for various temperatures.

grains) and promotes interlayer diffusion of oxygen, thereby also stimulating oxidation of the alloy, thus drastically increasing the resistance of the alloy compared to previous experiments [75, 79]. Our $12.5\,\mathrm{nm}$-thick Pt device has a resistivity of $1.2 \cdot 10^{-5}\,\Omega\,\mathrm{m}$ at room temperature, thus being almost two orders of magnitude larger than the resistivity of a device of equal thickness from Ref. [75] with a resistivity of $4.3 \cdot 10^{-7}\,\Omega\,\mathrm{m}$. The same holds for our PtAu alloys: our $14\,\mathrm{nm}$-thick $\mathrm{Pt_{0.75}Au_{0.25}}$ and $12.5\,\mathrm{nm}$-thick $\mathrm{Pt_{0.9}Au_{0.1}}$ devices have shown resistivities of $2 \cdot 10^{-6}\,\Omega\,\mathrm{m}$ and $6 \cdot 10^{-6}\,\Omega\,\mathrm{m}$, respectively, which is about one order of magnitude larger than the resistivities of $4\,\mathrm{nm}$-thick $\mathrm{Pt_{0.75}Au_{0.25}}$ and $\mathrm{Pt_{0.85}Au_{0.15}}$ devices presented in Ref. [79], with resistivites of $8 \cdot 10^{-7}\,\Omega\,\mathrm{m}$ and $7 \cdot 10^{-7}\,\Omega\,\mathrm{m}$, respectively. Due to this increase of resistance, we were not able to investigate samples thinner than $10\,\mathrm{nm}$, therefore not approaching the optimal thicknesses given by twice the spin diffusion length. Since the spin diffusion length of Pt is $\lambda_\mathrm{s} \sim 1.5\,\mathrm{nm}$ [75], we speculate the spin-diffusion length of PtAu to be of the same order of magnitude.

4.2 Field Dependence

If we take a look at Figs. 4.2 and 4.3, we notice that the MR effect exhibits a clear field dependence. This behavior is in contrast to the standard theory of SMR [50]. In order to investigate this phenomenon in more detail, we plot the normalized MR amplitude with respect to the applied field for different temperatures. The amplitudes were extracted from the ADMR measurement via Eq. 4.1 using a self-written automatized data evaluation script. Figure 4.4 shows the field dependent data of an $18\,\mathrm{nm}$-thick $\mathrm{Pt_{0.75}Au_{0.25}}$ device for the IP, OOPJ and OOPT configurations (**(a)**, **(b)**, **(c)**, respectively). In the IP configuration, the MR follows an almost linear growth behavior, with the slope increasing with decreasing temperature. For the low temperatures below $150\,\mathrm{K}$, the curves seem to start saturating. In the OOPT configuration, the signal is almost vanishing above $50\,\mathrm{K}$. However, as we discussed in the previous Section, for very low temperatures the MR amplitude is drastically increased. Eventually, the curve starts saturating, which is in contrast with the quadratic dependence expected from OMR. Finally, the OOPJ field dependence represents a superposition of the IP and OOPT dependence. In Fig. 4.3, we present the field dependent MR of $12.5\,\mathrm{nm}$-thick Pt and $13.25\,\mathrm{nm}$-thick $\mathrm{Pt_{0.9}Au_{0.1}}$ devices (**(a)** and **(b)**, respectively), for the IP configuration. Here, we also observe an almost linear increase of the MR with increasing

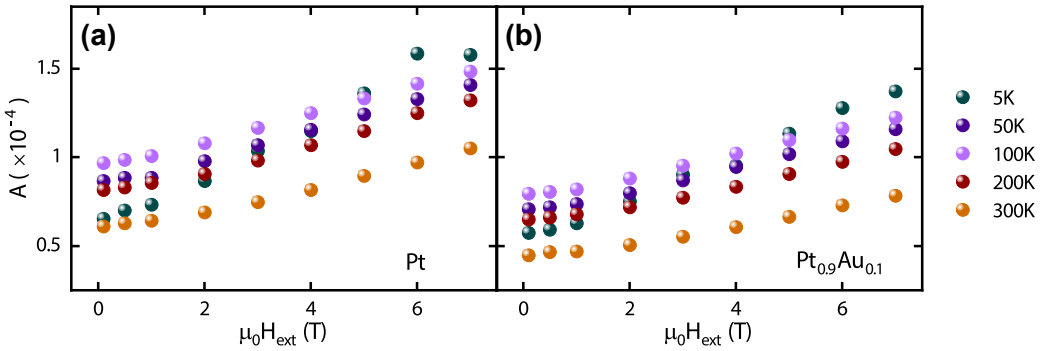

Fig. 4.5: Field dependence of normalized MR amplitude for IP measurements of $12.5\,\mathrm{nm}$ thick Pt **(a)**, and $13.25\,\mathrm{nm}$ thick $\mathrm{Pt_{0.9}Au_{0.1}}$ **(b)** devices.

field.

We assume that the cause of this deviation from the theoretical predictions lies in the imperfect NM/YIG interface. Due to magnetic pinning effects induced by finite surface roughness, as well as defects introduced by the sample fabrication process, the magnetic moments of the YIG at the interface are not perfectly aligned along the external magnetic field $\mu_0 H$, even for large fields. Thus, a channel for reduction of the SOT is opened, resulting in the decrease of SMR. However, we expect a saturation for large enough fields, since the number of aligned magnetic moments should increase with increasing fields and ultimetely saturate when all pinned moments are aligned. Furthermore, one could also consider the Hanle magnetoresistance (HMR) effect [88]. Similar to the OMR, the HMR also has a quadratic field dependence. In this case, however, the magnetic field is influencing the NM's SHE induced spin accumulation, rather than the conduction electrons, causing a precession of the spin accumulation around the external field direction. The spins will eventually dephase, therefore destroying the spin accumulation at the interface and ultimately lowering the ISHE-induced charge current. Nevertheless, we did not observe a quadratic field dependence, suggesting that pinning effects are the dominant source of the field dependence.

4.3 Temperature Dependence

In Fig. 4.6, we show the MR amplitudes of an $18\,\mathrm{nm}$-thick $\mathrm{Pt_{0.75}Au_{0.25}}$ device as a function of temperature for IP **(a)**, OOPJ **(b)** and OOPT **(c)** configurations. The transition from $5\,\mathrm{K}$ to $50\,\mathrm{K}$ shows a drastic decrease of the MR amplitude with increasing temperature for higher fields in case of the OOPJ and OOPT configurations. For temperatures above $100\,\mathrm{K}$, we observe a slight linear decrease of the MR amplitude with increasing temperature in all three configurations. Interestingly, for IP measurements at $0.5\,\mathrm{T}$ we see that the curve has a local maximum at $100\,\mathrm{K}$. Comparing this with Fig. 4.7, we observe the same behavior at $0.5\,\mathrm{T}$, as well as $3\,\mathrm{T}$, for the $12.5\,\mathrm{nm}$ thick Pt **(a)** and $13.25\,\mathrm{nm}$ thick $\mathrm{Pt_{0.9}Au_{0.1}}$ **(b)** devices. Above $100\,\mathrm{K}$, the signal decreases with temperature. As discussed in the previous Section, the steep decrease of MR in the out of plane configurations with increasing temperature is most probably a consequence of the dominant MPE-induced AMR at temperatures in vicinity of $T = 0$. To exclude parasitic MR effects not related to SMR, we focus on the measurements in

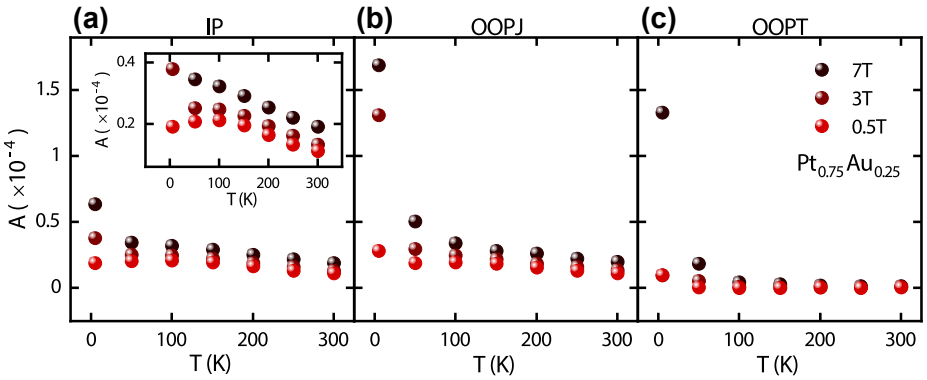

Fig. 4.6: Temperature dependence of normalized MR amplitude for IP **(a)**, OOPJ **(b)**, OOPT **(c)** measurements of an $18\,\mathrm{nm}$-thick $\mathrm{Pt}_{0.75}\mathrm{Au}_{0.25}$ device.

IP configuration. In order to qualitatively describe the observed temperature dependence it is necessary to elucidate the corresponding dependencies of the quantities which define the SMR (c.f. Eq. 2.7). Therefore, we are going to discuss the temperature-dependent behavior of the spin-Hall angle θ_{SH}, spin diffusion length λ_{s}, spin mixing conductance $g^{\uparrow\downarrow}$ and resistivity ρ of the NM. For this matter, we discuss the observations made in Refs. [89], [90] and [91].

In Ref. [89], SMR measurements of Pt/YIG bilayers were used to obtain values of the aforementioned quantities by fitting Eq. 2.7 to Pt-thickness dependent SMR amplitudes and by extracting the fit parameters. The θ_{SH} values obtained by this method clearly illustrate a temperature dependence. Starting at low temperatures $T = 10\,\mathrm{K}$, θ_{SH} has a value of $\sim 7.5/\%$, which increases to its maximal value of $\sim 11\%$ at $T = 200\,\mathrm{K}$. With further increasing of the temperature, a slight decrease of θ_{SH} to $\sim 10.5\%$ at $T = 300\,\mathrm{K}$ is observed. In the case of $g^{\uparrow\downarrow}$ (the real part, as discussed in Chap. 2.3) and λ_{s}, the obtained values did not show a pronounced temperature dependence. Indeed, the temperature dependent SMR measurements in Ref. [92] resemble the temperature dependence of θ_{SH}. Since our measurements are qualitatively different, we assume that $g^{\uparrow\downarrow}$ and λ_{s} are temperature dependent as well. A constant $g^{\uparrow\downarrow}$ implies that the thermal fluctuations of the magnetization of YIG are negligible [58]. Thermal fluctuations, however, can be regarded as a consequence of an energy increase due to rising temperature, reducing the stability of the magnetic system by introducing chaotic magnetization dynamics. Therefore, we expect finite deviations from the clearly defined two limiting cases $\boldsymbol{M} \parallel \boldsymbol{\mu}_{\mathrm{s}}$ and $\boldsymbol{M} \perp \boldsymbol{\mu}_{\mathrm{s}}$ which define our SMR amplitude. Thus, the SMR is lowered by thermal magnetization fluctuations, which are reflected in a temperature dependent $g^{\uparrow\downarrow}$ [93].

In Ref. [90], spin absorption in lateral spin valve structures was used for studying the spin transport and the temperature dependence of the SHE in Pt and Au. The θ_{SH} of Pt was shown to have a similar temperature dependence as discussed in Ref. [89], although being relatively small with a maximal value of $\sim 2\%$ at $T = 100\,\mathrm{K}$. In the case of Au, the maximal value of θ_{SH} is 0.15% at $T = 10\,\mathrm{K}$ and reduces with increasing temperature. The more important result, however, is the pronounced temperature dependence of λ_{s} for Pt (Au), which decreases from $\sim 3.5\,\mathrm{nm}$ ($\sim 55\,\mathrm{nm}$) at $T = 10\,\mathrm{K}$ to $\sim 2\,\mathrm{nm}$ ($\sim 30\,\mathrm{nm}$) at $T = 300\,\mathrm{K}$. SMR measurements presented in Ref. [91] (by using a similar technique as in Ref. [89]), yielded qualitatively the same result as the measurements in Ref. [90] for λ_{s},

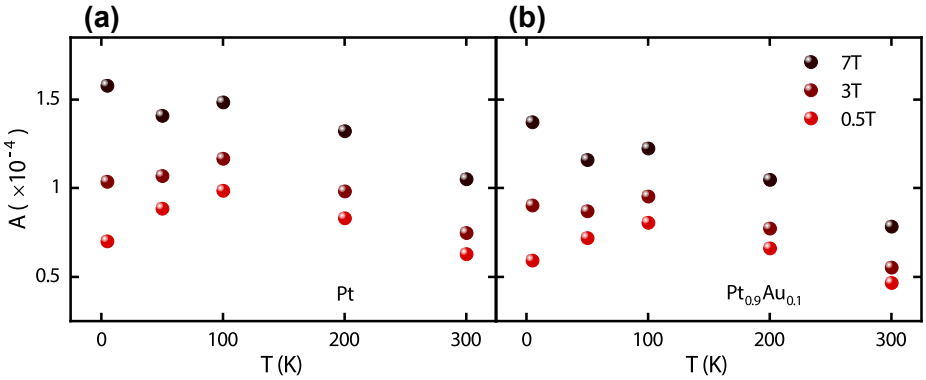

Fig. 4.7: Temperature dependence of normalized MR amplitudefor IP measurements of $12.5\,\mathrm{nm}$-thick Pt **(a)** and $13.25\,\mathrm{nm}$-thick $\mathrm{Pt_{0.9}Au_{0.1}}$ **(b)** devices.

which decreases with increasing temperature temperature, while θ_{SH} and $g^{\uparrow\downarrow}$ were assumed to be independent of temperature. In both works the decrease of λ_{s} was attributed to increased phonon-scattering with increasing temperature, which can be described by the Elliot-Yafet mechanism [94, 95]. Intuitively, the decrease of λ_{s} should induce a reduction of the SMR amplitude, since the spin-flip scattering events arise more often, thus resulting in an increased relaxation of the electron spins and finally reducing the spin current.

That being said, we are able to qualitatively explain the specific temperature dependence of our measurements. The three mechanisms, namely increase of θ_{SH} and decrease of $g^{\uparrow\downarrow}$ and λ_{s} with increasing temperature, are balanced for temperatures where we observe a maximum. For lower temperatures, the increase in MR with increasing temperature is dominated by the increase of θ_{SH} with temperature, whereas the SMR amplitude is reduced by the thermal fluctuations and phonon scattering for higher temperatures.

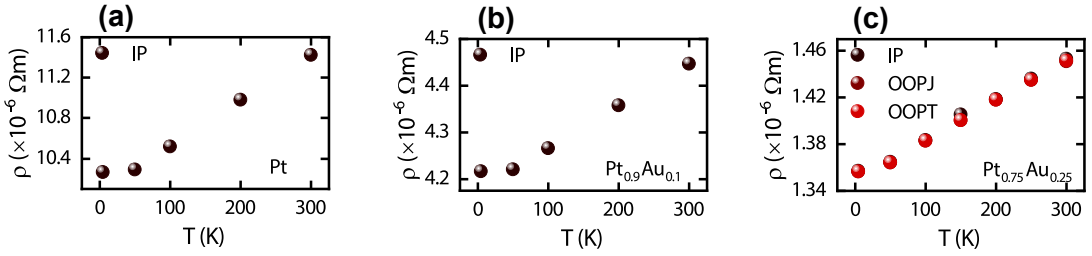

Fig. 4.8: Temperature dependence of resistivities of $12.5\,\mathrm{nm}$-thick Pt **(a)**, $13.25\,\mathrm{nm}$-thick $\mathrm{Pt_{0.9}Au_{0.1}}$ **(b)** and $18\,\mathrm{nm}$-thick $\mathrm{Pt_{0.75}Au_{0.25}}$ **(c)** devices for measurements conducted at $\mu_0 H = 7\,\mathrm{T}$.

Let us now consider the resistivities of the particular samples. Figure 4.8 shows the corresponding temperature dependence for the Pt **(a)**, $\mathrm{Pt_{0.9}Au_{0.1}}$ **(b)** and $\mathrm{Pt_{0.0.75}Au_{0.25}}$ **(c)** samples. As expected, the resistivities increase with temperature, corresponding to the usual metallic behavior. At very low temperatures, however, the electron scattering is mainly influenced by boundary surfaces, impurities and defects [96]. Thus, a further decrease of temperature is not resulting in a lowering of resistivity - the residual resistivity is reached. Interestingly, the resistivities are generally one to two orders of magnitude larger than we would expect for Pt and its alloys with Au of similar thickness [75, 79]. This again indicates that the overall quality of the devices is not as good as expected. Furthermore, it could also be an indicator that the assumed thickness is not corresponding to the real one. As a

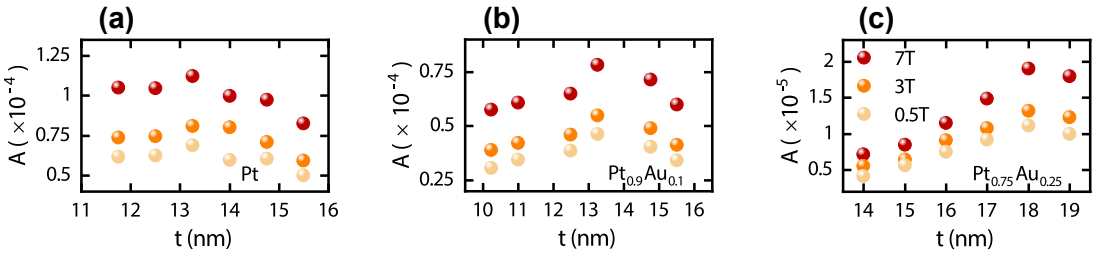

Fig. 4.9: Thickness dependence of MR amplitudes for Pt **(a)**, $\mathrm{Pt_{0.9}Au_{0.1}}$ **(b)** and $\mathrm{Pt_{0.75}Au_{0.25}}$ **(c)** devices, for IP measurements conducted at $\mu_0 H = 7\,\mathrm{T}$ and $T = 300\,\mathrm{K}$. The legend from **(c)** is valid for **(a)** and **(b)** as well.

matter of fact, we conducted AFM measurements in order to confirm the thickness profile calculated from the sputtering parameters. However, the measurements have shown inconsistencies and pointed to another possible issue due to potential resist residues which would alter the measured thickness, but even more important, strongly influence the interface quality and therefore reduce the spin mixing conductance. In the following Section, we will take a look at the thickness dependencies in order to gain more insight.

4.4 Thickness Dependence

Finally, we want to discuss the thickness dependencies of our SMR measurements. The main reason for fabricating devices of different thickness was to obtain the ability to extract the key quantities defining the SMR effect: the spin-Hall angle θ_{SH}, spin diffusion length λ_{s} and spin mixing conductance $g^{\uparrow\downarrow}$. Since Pt is already well characterized, we were able to use it as a reference. As already mentioned, we expect λ_{s} to be in the order of magnitude of $1\,\mathrm{nm}$. Figure 4.9 shows the normalized MR amplitudes as a function of the device thicknesses from IP measurements conducted at $\mu_0 H = 7\,\mathrm{T}$ and $T = 300\,\mathrm{K}$, for Pt **(a)**, $\mathrm{Pt_{0.9}Au_{0.1}}$ **(b)** and $\mathrm{Pt_{0.75}Au_{0.25}}$ **(c)**. Indeed, for all three material systems we observe a thickness dependent behavior. Furthermore, we can unambiguously define the thicknesses for which the SMR is exhibiting a maximum. As a rule of thumb, one can estimate λ_{s} by half the thickness for which the SMR is maximum: the SHE will generate spin accumulations on the lower and upper surface of the NM for a spin current running perpendicular to the NM's plane. The maximum spin accumulation on the NM/YIG interface will be induced if the total thickness of the NM exceeds two times λ_{s} such that the two interfaces do not influence each other. In addition, for larger thickness values, the SMR effect is reduced as shunting effects start to play a role. Of course, in reality the situation is more complicated,

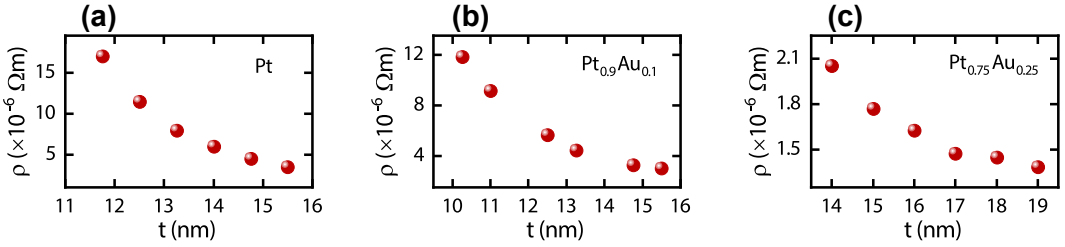

Fig. 4.10: Thickness dependence of resistivities for Pt **(a)**, $\mathrm{Pt_{0.9}Au_{0.1}}$ **(b)** and $\mathrm{Pt_{0.75}Au_{0.25}}$ **(c)** devices for measurements conducted at $\mu_0 H = 7\,\mathrm{T}$ and $T = 300\,\mathrm{K}$.

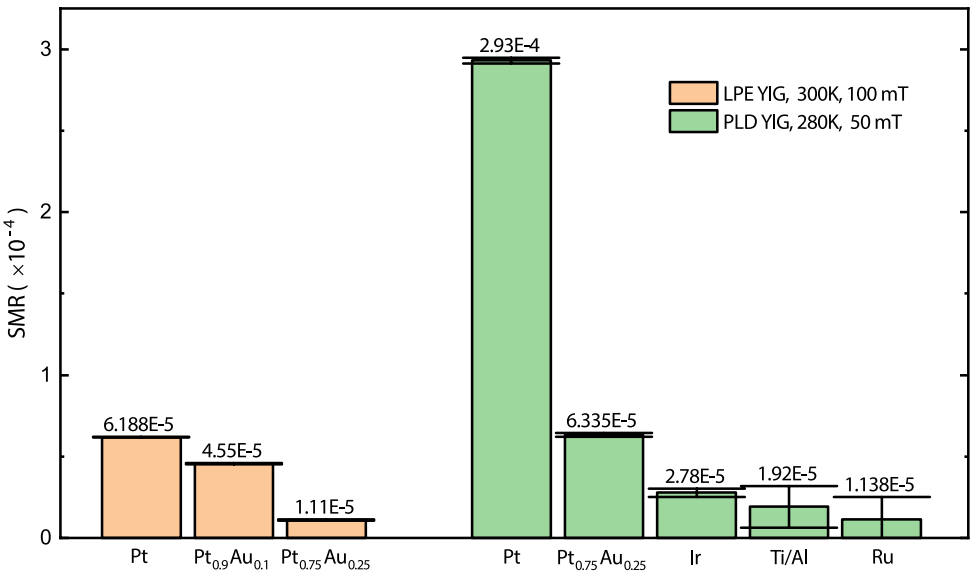

Fig. 4.11: SMR of different metals adjacent to YIG used for fabrication of devices during this thesis. Liquid Phase Epitaxy (LPE) grown YIG films were used for characterization of novel PtAu alloys, whereas Pulsed Laser Deposition (PLD) grown YIG films were used for magnon spin transport measurements. External parameters as well as fit errors are indicated.

but this rule of thumb is good enough for a rough estimation of our measurements. Hence, we can estimate $\lambda_\mathrm{s} = 7\,\mathrm{nm}$ from Fig. 4.9 **(a)**, which is much larger than the typically reported $\lambda_\mathrm{s} = 1.5\,\mathrm{nm}$ for Pt adjacent to YIG [75]. We conclude that the observed thickness dependence is not a consequence of the spin diffusion mechanism, but rather reflecting the fact that the NM/YIG interface was not of the same quality on the whole sample. Therefore, we expect a spatially inhomogeneous spin mixing conductance $g^{\uparrow\downarrow}$ across the sample, thus causing a spatially, rather than thickness dependent, behavior. This issue, most likely caused by the resist, has to be addressed for future studies, such that a reliable extraction of spin transport parameters is possible. However, we can easily verify that the devices are of different thickness by inspecting the samples' resistivities with respect to thickness, as shown in Fig. 4.10 for Pt **(a)**, $\mathrm{Pt_{0.9}Au_{0.1}}$ **(b)** and $\mathrm{Pt_{0.75}Au_{0.25}}$ **(c)** devices. Obviously, the resistivities increase with decrease of thickness, indicating the contributions from surface scattering. We must, however, point out once more that the resistivites are at least one order of magnitude larger than expected, as discussed in Chap. 4.1.

4.5 Overview of Used Materials

The main purpose of this thesis is the manipulation of magnon spin transport by utilizing materials exhibiting different spin-Hall efficiencies. By tuning the SHE, we are able to compare and better understand contributions stemming from both SHE and thermally modulated magnon conductivity, therefore gaining a deeper insight into the mechanisms of magnon transport. Here, we want to summarize the SMR measurements conducted for both LPE- and PLD-grown YIG samples, as illustrated in Fig. 4.11. We immediately observe an enormous difference between the two types of samples, with materials of low θ_SH (c.f.

3.1), grown on PLD YIG, showing SMR amplitudes of same order as Pt grown on LPE YIG. We can attribute this difference to the higher interface quality of the PLD YIG films, therefore exhibiting larger $g^{\uparrow\downarrow}$ as compared to LPE YIG. Nevertheless, as we are going to see in the next Chapter, deploying materials with negligible spin-Hall angles (as compared to Pt), will allow to almost totally turn off the SHE channel for inducing magnons, and examine the properties of thermal magnon generation exclusively.

4.6 Summary

In this Chapter, we discussed SMR measurements of NM/YIG heterostructures. The main focus lay in the characterization of different PtAu alloys, which were promising candidates for highly efficient spin current generation [78, 79]. Therefore, we patterned $\mathrm{Pt_{1-x}Au_x}$ devices with $x = 0.1$ and $x = 0.25$ on two YIG films, with additional reference Pt devices. We conducted SMR measurements in three mutually orthogonal planes (c.f. Chap. 4.1), covering the range of temperatures from $T = 5\,\mathrm{K}$ to $T = 300\,\mathrm{K}$ and magnetic fields from $\mu_0 H = 0.1\,\mathrm{T}$ to $\mu_0 H = 7\,\mathrm{T}$. In order to perform thickness dependent measurements, the so-called wedge-sputtering technique was employed (c.f. Chap. 3.2). For low temperatures $T < 100\,\mathrm{K}$, an additional MR effect unrelated to SMR physics was observed in the OOPJ and OOPT measurement configurations. This effect is most probably caused by the combination of OMR, MPE induced AMR and imperfect alignment of the samples to the external magnetic field rotation planes. Furthermore, we observed a pronounced magnetic field dependence of the SMR (c.f. Chap. 4.2), which is not theoretically predicted [50], but most likely a consequence of an imperfect NM/YIG interface that introduces pinning effects. The characteristic temperature dependence of the SMR measurements (c.f. Chap. 4.3) was qualitatively explained by considering the temperature dependencies of the spin Hall angle θ_{SH}, the spin diffusion length λ_{s} and the spin mixing conductance $g^{\uparrow\downarrow}$. In order to estimate the values of these quantities for our devices, we also conducted thickness dependent measurements (c.f. Chap. 4.4). However, peculiar results indicated that the interface quality of our devices was spatially very inhomogeneous. Furthermore, additional AFM measurements yielded inconsistencies, indicating possible resist residues at the interface. In general, all devices exhibited enormously high resistance, namely one to two orders of magnitude larger than literature values, therefore not allowing measurements of few-nm-thick devices, which were expected to exhibit the largest SHE. We address this issue to defects introduced during the fabrication process. We could, however, conclude that finite SMR was observed for the PtAu alloys, with a decreasing SMR amplitude with increasing Au concentration in the alloy. Finally, an overview of SMR measurements for all metals used for electrode fabrication in this thesis was presented (c.f. Chap. 4.5).

5 All Electrical Magnon Transport in Multiterminal NM | YIG Nanostructures

Since the discovery [22, 23] of long distance magnon spin transport in heterostructures consisting of two separated and electrically isolated Pt electrodes on a YIG substrate, as described in Chap. 2.4, a widely accepted theory [56, 57, 59] explaining its underlying physical principles was established. Practically, such a material system allows the transport of spin information via *magnons*, the quantized excitations of the spin system in a magnetically ordered material (MOI), rather than by spin polarized conduction electrons. Caused by the MOI's large bandgap, the absence of conduction electrons is a promising step towards the development of low-power spintronic devices [17, 97, 98, 99, 100, 101]. However, the most crucial limitation of such a system arises due to the fact that the magnon number in a spin system is not conserved. Thus, an efficient way of manipulating (attenuating and enhancing) magnonic transport implies an artificially induced variation of the number of magnons in the system [17]. In order to achieve this, a third Pt electrode, in between the existing two (c.f. Fig. 5.1 **(b)**), is added to the heterostructure design discussed in Chap. 2.4. Modeled as a magnon transistor device, we now have an injector electrode (source), a modulator electrode (gate) and a detector electrode (drain). In this configuration, the transport of magnons between injector and detector can be altered via the application of a DC charge current in the modulator, leading to a change of the magnon density beneath the modulator via SHE- and thermally induced magnon accumulations (c.f. Fig. 5.1 **(c)-(e)**). As a result, the magnon conductivity σ_{m} between injector and detector can be tuned by the application of the modulator current. This particularly allows to counteract the magnetic Gilbert damping by SHE-induced spin orbit torques (SOT) acting on the magnetization and therefore effectively reduce the damping-induced magnon relaxation [17, 18, 102, 103, 104, 105, 106]. In a recent publication [18], Wimmer et al. from the Walther-Meißner-Institut demonstrated that for large enough modulator currents it is possible to fully compensate the Gilbert damping by means of SOT, reaching a "zero-effective damping regime". This leads to a diverging magnon lifetime, ensuing spin transport with an effectively vanishing magnon decay underneath the modulator.

From an experimental point of view, the magnon transport signal between injector and detector as function of the DC bias in the modulator corresponds to a magnon conductivity measurement (c.f. Chap. 3.3). As expected for an SHE-active modulator (as in the case of Pt), the detector signal (i.e. magnon conductivity) exhibits a modulator current dependence given by a superposition of a linear and quadratic contribution in modulator current for the low bias regime. However, for larger currents, a deviation from this behavior is observed. This deviation is parametrized by two characteristic currents: (i) the "onset current" corresponds to the magnon conductivity modulation becoming strongly non-linear (and non-quadratic) and (ii) the "critical current", which is related to the state where the magnon damping beneath the modulator is fully compensated. These findings were discussed within the theoretical framework of spin-current induced formation of a magnon Bose-Einstein condensate (BEC) [15, 16, 107, 108, 109, 110]. Recently, similar experiments were conducted by Liu et al. [106]. Different to the result obtained by Wimmer et al. [18], it is demonstrated that the magnon conductivity decreases (rather than increases) beyond

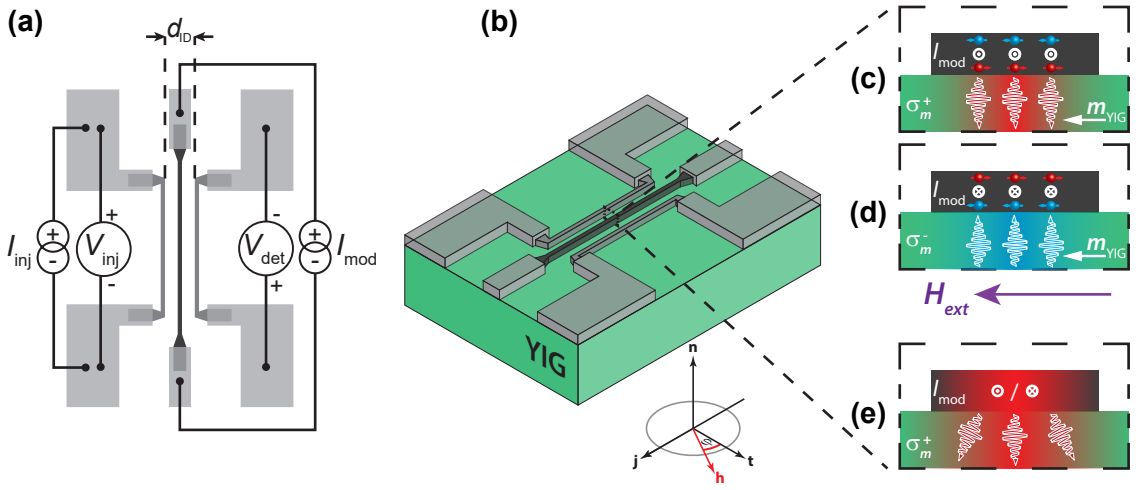

Fig. 5.1: (a) Schematic illustration of a device and the electrical connection scheme. Going from left to right, the electrodes are denoted as the injector (I), modulator (M) and detector (D). The I and D electrodes are made of Pt and are $50\,\mu m$ long, $0.5\,\mu m$ wide and $5\,nm$ thick, whereas for the M electrode different NMs and geometries were utilized, with a constant length of $64\,\mu m$. The edge-to-edge distance d_{ID} between I and D is indicated. **(b)** 3D illustration of a device with the coordinate system and the definition of the external magnetic field angle φ. The M electrode can, generally, alter the magnon transport by means of SHE: **(c)**, **(d)** or by thermal injection of magnons: **(e)**. **(c)** The magnetic moment associated with the SHE-induced spin accumulation at the NM/YIG interface for $I_{mod} > 0$ is antiparallel to the sample magnetization, therefore increasing the magnon density underneath the M, as well as increasing the magnon conductivity indicated by σ_m^+. **(d)** For $I_{mod} < 0$ the induced magnetic moment is parallel to the sample magnetization, causing a depletion of the magnon system underneath M and, subsequently, a reduced magnon conductivity indicated by σ_m^-. **(e)** Thermal injection of magnons is active for both current directions, regardless of the magnetization orientation and used NM, thus increasing the magnon conductivity indicated by σ_m^+.

the critical current. Furthermore, no dependence on the relative field orientation or field strength for the onset current was observed. Therefore, the authors argue that the SSE torque (c.f. Chap. 2.4) plays an essential role, contrary to the assumptions of Wimmer et al. [18].

In order to gain a deeper insight and widen the understanding of the observed phenomena, this work attempts to disentangle the SHE and thermally induced contributions to the spin transport modulation introduced above. For this matter, we replicated the device design with Pt injector and detector and introduced several different metals for the modulator (c.f. Chap. 3.2). By utilizing metals of different SHE-efficiency (c.f Tab. 3.1 and Fig. 4.11), we were able to progressively reduce the SHE-induced contribution. The spin Hall physics of the metals is characterized by means of SMR measurements (c.f. Chap. 4).

In our experiment, we apply a charge current I_{inj} to the injector and simultaneously measure the corresponding magnon transport detector voltage related to either the electrical or thermal excitation of magnons at the injector, as discussed in Chap. 2.4. The magnon conductivity in YIG is altered by an additional current I_{mod} applied to the modulator strip placed in between the injector and detector. In order to discern between electrically and thermally injected magnons from the injector as well as excluding the direct magnon spin signal stemming from the modulator, we apply either the DC current reversal method or AC lock-in detection as described in detail in Chap. 3.3. Both measurement schemes allow

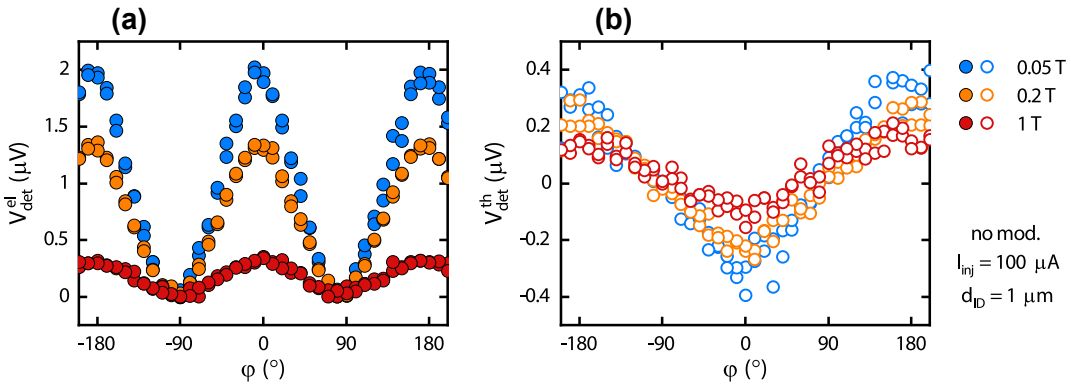

Fig. 5.2: Angle-dependent magnon transport measurements for a two-electrode device and different magnetic fields: **(a)** electric-contribution of the detector signal $V_{\mathrm{det}}^{\mathrm{el}}$, **(b)** thermal-contribution of the detector signal $V_{\mathrm{det}}^{\mathrm{th}}$. The specific parameters are indicated in the plot, with $T = 280\,\mathrm{K}$. The YIG sample thickness is $10\,\mathrm{nm}$.

for an extraction of the magnon conductivity change in the YIG as a function of the applied modulator current bias. Potential differences between magnon conductivity changes of electrically and thermally excited magnons from the injector will be discussed within this Chapter. All measurements were conducted at $T = 280\,\mathrm{K}$ for the in-plane (IP) configuration as shown in Fig. 5.1 **(b)**.

This Chapter is organized as follows: in Chap. 5.1, we present the angle dependent magnon transport measurements of a two-electrode device, showcasing the principles of magnon transport described in Chap. 2.4. Furthermore, we demonstrate the change of the detector signal amplitude upon applying a current I_{mod} to the modulator electrode for a three-electrode device in Chap. 5.1.1. A more systematic analysis of the same effect, where we discuss the observed features in great detail, is offered in Chap. 5.2.

5.1 Angle-dependent Magnon Transport Measurements

In order to fully understand the effect of altering the magnon conductivity by utilizing a modulator electrode, we will first consider the case of magnon transport as demonstrated in Ref. [22, 23]. We therefore investigate a reference device consisting of two parallel, electrically isolated Pt electrodes, as illustrated in Fig. 5.1 **(a)**, without a patterned modulator electrode. In Fig. 5.2, we present angle-dependent magnon transport measurements for both electrical **(a)** and thermal **(b)** contributions to the detector voltage of a two-electrode device. Let us first consider the electrical contribution. The signal modulates like $\cos^2(\varphi)$ [22], where φ corresponds to the angle defined by the external field direction $\boldsymbol{H}$ ($\boldsymbol{h} = \boldsymbol{H}/|\boldsymbol{H}|$; we hereby consider large enough external magnetic fields, such that the magnetization is collinear to the external field: $\boldsymbol{M} \parallel \boldsymbol{H}$) and the $\mathbf{t}$-direction (c.f. Fig. 5.1). Due to the SHE, a charge current flowing through the Pt injector induces a spin accumulation $\boldsymbol{\mu}_{\mathrm{s}}$ at the interface, which in turn gives rise to a magnon accumulation in YIG. For $\varphi = \pm 90°$: $\boldsymbol{M} \perp \boldsymbol{\mu}_{\mathrm{s}}$, the spin accumulation exerts maximal SOT on the magnetization, generating transverse spin excitations (perpendicular to the magnetization). Magnons, however, correspond to excitations carrying angular momentum parallel to the magnetization, hence the transverse spin excitations dephase on a length scale comparable to the magnetic exchange length of YIG ($\sim 10\,\mathrm{nm}$ [111]) and cannot reach the detector for the typical length scales conside-

red. Thus, for $\boldsymbol{M} \perp \boldsymbol{\mu}_\mathrm{s}$, we expect no voltage signal at the detector. However, for $\boldsymbol{M} \parallel \boldsymbol{\mu}_\mathrm{s}$, spin flip scattering of electron spins at the interface occurs [22, 57, 58], causing creation or annihilation of magnons (c.f. Chap. 2.4 and Fig. 5.1 **(c)**, **(d)**). In other words, the SOT now acts on the thermal fluctuations of the magnetization, enhancing or reducing these fluctuations and thus generating or annihilating magnons locally at the interface. These non-equilibrium magnons then diffuse giving rise to a magnonic spin current, which induces a spin accumulation at the second Pt/YIG (detector) interface. Thus, only the spin accumulation component parallel to the magnetization ($\propto \cos\varphi$) contributes to magnon transport. Furthermore, the detection is implemented by means of the ISHE, accounting for another $\cos\varphi$ dependence. Finally, we obtain the observed $\cos^2(\varphi)$-dependence. Considering the thermal contribution, we observe a $\cos\varphi$-shaped modulation. Due to Joule heating at the injector, magnons will be excited thermally, independent of the magnetization direction (c.f. Fig. 5.1 **(e)**), and diffuse to the detector. However, the detection is still governed by the ISHE-symmetry, causing the observed $\cos\varphi$ behavior.

For both contributions, the detector signals decrease with increasing magnetic field intensity. Since this effect was observed and explained before [112], we are going to offer a very simple qualitative explanation: a higher external field causes a stiffer magnetic lattice in our sample, thereby suppressing propagation of spin waves. It is important to point out that the actual underlying field dependence is a combination of the dependencies of all processes and phenomena contributing to the type of measurements carried out in the magnon transport experiment, therefore not being trivial as one might conclude after the offered qualitative explanation [112]. Furthermore, the deviation from a perfect $\cos^2(\varphi)$ in form of a triangular shape, which is pronounced for lower fields, is a consequenece of the cubic anisotropy of our YIG sample [34]. It is of crucial importance to point out that this kind of transport is only possible for finite temperatures $T \neq 0$. This can also be elucidated intuitively: at finite temperatures the entropy of the system will be finite, thus causing fluctuations of the magnetization and a finite thermal magnon occupation. These fluctuations will allow the aforementioned spin flip scattering (for $\boldsymbol{M} \parallel \boldsymbol{H}$) in the first place. Furthermore, for the limiting case $T = 0$, the magnetization is constituted of perfectly aligned moments, therefore totally inhibiting magnon transport induced via SHE effects. The actual temperature dependence for magnon transport in such a geometry is constituted of dependencies of the electronic and magnonic system, as well as of the spin conversion processes at the interfaces [23, 57, 59, 113]. Therefore, all measurements presented in this Chapter were conducted at $T = 280\,\mathrm{K}$, which was empirically shown to be the optimal operating temperature due to an improved temperature stability of our measurement setup.

Finally, we want to point out that we used a reversed contact polarity for the voltage measurement at the detector as compared to the injector, as shown in Fig 5.1 **(a)**. For injector and detector electrodes made of material with equal sign of the spin Hall angle, the ISHE-induced charge current caused by SHE-induced magnons flows parallel to the charge current applied to the injector. Since we are recording the detector voltage using open boundary conditions, the ISHE charge current is balanced out by an electric potential of opposite sign [23]. Therefore, our measurement scheme yields a positive electrical contribution signal.

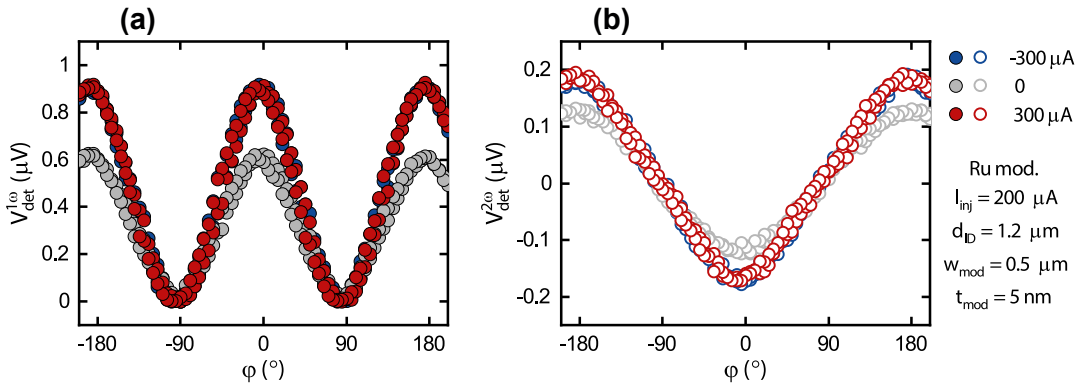

Fig. 5.3: Angle-dependent magnon transport measurements for a three-electrode device and different modulator (Ru) currents: **(a)** first harmonic detector signal $V_{\mathrm{det}}^{1\omega}$, **(b)** second harmonic detector signal $V_{\mathrm{det}}^{2\omega}$. The specific parameters are indicated in the plot, with $\mu_0 H = 50\,\mathrm{mT}$. The YIG sample thickness is $13.8\,\mathrm{nm}$.

5.1.1 Magnon Transistor Device

The previously described diffusive magnon transport is mainly limited by the fact that the number of magnons in a magnetic system is not conserved. Since the transport in our multiterminal NM/YIG structures is mediated by magnons, a decrease of the number of excited magnons inevitably causes a decrease of the macroscopic magnon conductivity. Similar to the Drude conductivity for mobile charge carriers, the magnon conductivity σ_{m} of an out-of-equilibrium magnon gas with parabolic dispersion can be written as [17]:

$$\sigma_{\mathrm{m}} = \hbar \frac{n_{\mathrm{m}} \tau_{\mathrm{m}}}{m_{\mathrm{m}}}, \tag{5.1}$$

where n_{m}, τ_{m} and m_{m} represent the magnon density, total momentum scattering time and effective mass, respectively. Increasing the magnon density therefore offers a simple way to increase the magnon conductivity. This qualitatively explains the observed increase of modulation efficiency with decreasing YIG thickness [17, 18, 106], since the same number of externally excited magnons in a thin sample causes a higher density of magnons, as compared to a thicker sample. We harnessed this fact maximally, using ultrathin YIG samples with $t_{\mathrm{YIG}} \sim 10\,\mathrm{nm}$. By introducing the transistor design, i.e. by adding an additional electrode (modulator) between injector and detector, we are able to manipulate the conduction channel in similar fashion to a gate electrode in a semiconductor transistor. We are now able to excite magnons by means of SHE and thermal injection, thus altering the conductivity. As already pointed out, the used measurement techniques were tailored to disregard the spin accumulation arriving at the detector, originating from the modulator. Choosing from a variety of NMs (c.f. Tab. 3.1) used for the modulator, we are able to gradually reduce SHE contribution to the transport modulation, while maintaining the thermal injection of magnons due to Joule heating.

In order to visualize the effect of varying spin Hall efficiencies of different modulator materials, we performed angle-dependent measurements of transistor devices with modulators made of Ti/Al, Ru, Ir, PtAu, and Pt (c.f. Fig. 4.11 for SMR measurements of these devices). The measurements were conducted for zero modulator current as well as for finite current biases of both polarities ($\pm I_{\mathrm{mod}}$) at $\mu_0 H = 50\,\mathrm{mT}$. The corresponding results for

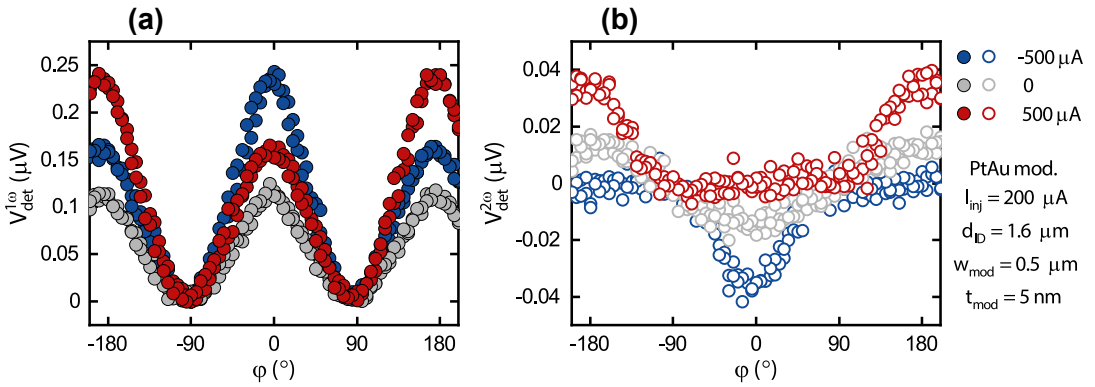

Fig. 5.4: Angle-dependent magnon transport measurements for a three-electrode device and different modulator ($Pt_{0.75}Au_{0.25}$) currents: **(a)** first harmonic detector signal $V_{\mathrm{det}}^{1\omega}$, **(b)** second harmonic detector signal $V_{\mathrm{det}}^{2\omega}$. The specific parameters are indicated in the plot, with $\mu_0 H = 50\,\mathrm{mT}$. The YIG sample thickness is $20\,\mathrm{nm}$.

a device with a Ru modulator are shown in Fig. 5.3 for the first **(a)** and second **(b)** harmonic detector signals. We observe relative increases of 38% and 66% for the amplitudes of the first and second harmonic signal, respectively. Applying a finite I_{mod} is causing an increase of the signal amplitude in both contributions **(a)** and **(b)**, with the angle dependence for $I_{\mathrm{mod}} = 0$ (grey data points) being preserved regardless of the current polarity (red and blue data points). Furthermore, the measurements for the opposite current directions are perfectly overlapping (in limits of the noise level). The obtained measurements are, indeed, confirming our predictions. Since Ru is shown to have a negligible spin Hall efficiency (c.f. Fig. 4.11), applying a finite current to the Ru modulator causes a modulation of the spin transport due to excitation of thermal magnons exclusively, as depicted in Fig. 5.1 **(e)**. Since the thermal excitation is present regardless of the field orientation and current direction, it is not giving rise to additional angle dependencies, as compared to the zero-current case. Both current polarizations applied to the modulator yield the same result, since the Joule heating scales with I_{mod}^2. These findings can also be applied for the device with a Ti/Al modulator, due to its negligible spin Hall efficiency (c.f. Fig. 4.11).

Next, we consider a transistor device with a PtAu modulator, exhibiting finite, relatively small, spin Hall efficiency (c.f. Fig. 4.11). In this case, we expect a combination of all three scenarios depicted in Fig. 5.1: SHE-induced accumulation **(c)**, SHE-induced depletion **(d)** and thermal excitation **(e)**. The corresponding measurements are shown in Fig. 5.4. Let us start by considering the first harmonic signal **(a)**. We see that the signal is amplified for both current polarizations, however an additional angle dependence, for a finite modulator current, is induced. For $I_{\mathrm{mod}} > 0$ (red data points), we observe a significant relative increase of 118% of the signal amplitude for $\varphi = \pm 180°$, corresponding to the $\boldsymbol{H} \parallel \boldsymbol{\mu}_{\mathrm{s}}$ case. Since the magnetic moment associated with $\boldsymbol{\mu}_{\mathrm{s}}$ is pointing in the opposite direction, magnon creating spin flip scattering will occur, giving rise to an SHE-induced magnon accumulation underneath the modulator. Furthermore, combined with the magnetization direction independent thermal excitation, the conductivity will be enhanced even more. Accordingly, we expect a decrease of the signal for $\varphi = 0°$ due to SHE-induced magnon depletion. However, the thermal excitation is counterbalancing and even overcompensating this effect, yet leading to a finite amplification of the signal, as compared to the $I_{\mathrm{mod}} = 0$ measure-

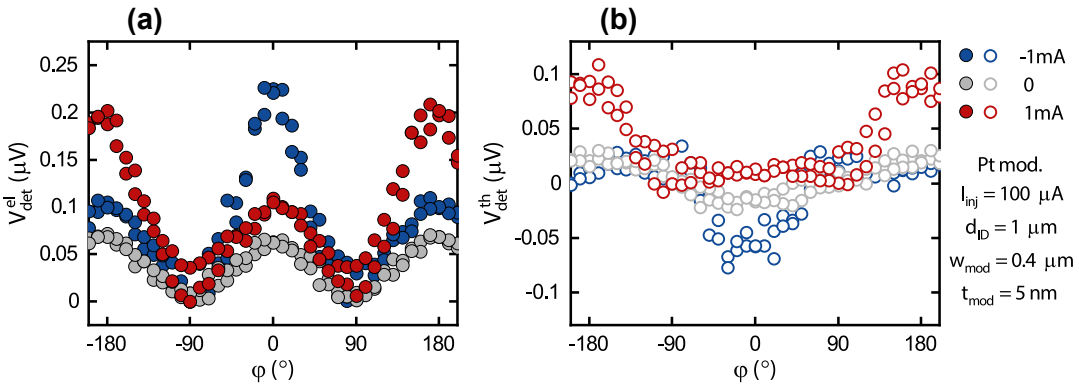

Fig. 5.5: Angle-dependent magnon transport measurements for a three-electrode device and different modulator (Pt) currents: **(a)** electric contribution detector signal $V_{\mathrm{det}}^{\mathrm{el}}$, **(b)** thermal contribution detector signal $V_{\mathrm{det}}^{\mathrm{th}}$. The specific parameters are indicated in the plot, with $\mu_0 H = 50\,\mathrm{mT}$. The YIG sample thickness is $20\,\mathrm{nm}$.

ments (grey data points), with a relative increase of 50%. For $I_{\mathrm{mod}} < 0$ (blue data points), we observe a pronounced signal increase for $\varphi = 0$, whereas a slight increase arises for $\varphi = \pm 180°$. This reflects the symmetry of the SHE upon current reversal (c.f. Fig. 2.3), since compared to the $I_{\mathrm{mod}} > 0$ case, $\boldsymbol{\mu}_{\mathrm{s}}$ will point in the opposite direction. As a result, SHE-induced magnon accumulation and depletion occur for $\varphi = 0°$, and $\varphi = \pm 180°$, respectively. This observation is consistent with our theory, furthermore corroborating the prediction of SHE-induced magnons. The same holds for the second harmonic signal **(b)**. We observe a signal increase/decrease for the relative orientation of current and field causing magnon accumulation/depletion underneath the modulator. The relative increase of the amplitude for $I_{\mathrm{mod}} > 0$ and $\varphi = \pm 180°$ is about 100%, whereas the signal is totally diminished for $\varphi = 0$, arguably even showing a change of sign, thus the relative change of the amplitude is $\leq -100\%$. Again, the opposite holds for $I_{\mathrm{mod}} < 0$. We can conclude that in both cases **(a)** and **(b)**, an additional angle dependence caused by the finite SHE efficiency of the modulator is superimposed to the $I_{\mathrm{mod}} = 0$ case. Hereby, we confirm the observations from Refs. [18, 106]. The observation made for the device with a PtAu modulator are as well applicable to devices with Ir modulators, due to comparable spin Hall efficiency (c.f. Fig. 4.11).

Finally, considering the measurements with a Pt modulator depicted in Fig. 5.5, we qualitatively observe the same effects as for the PtAu modulator. In the electrical/thermal contribution signal **(a)**/**(b)** for $I_{\mathrm{mod}} > 0$ (red data points) we observe a relative amplitude increase of of $233\%/300\%$ for $\varphi = \pm 180°$ and $75\%/\leq -100\%$ for $\varphi = 0$. We also observe a considerable mismatch of the enhancements for the different current polarizations in both **(a)** (233% versus 275% for $I_{\mathrm{mod}} > 0$ and $I_{\mathrm{mod}} < 0$, respectively) and **(b)** (300% versus 200% for $I_{\mathrm{mod}} > 0$ and $I_{\mathrm{mod}} < 0$, respectively). Furthermore, in the electric contribution signal **(a)**, an additional hysteretic effect can be observed at $\varphi = \pm 90°$, in a way that the signal is lifted at $\varphi = 90°$ for the forward and at $\varphi = -90°$ for the backward rotation of the field orientation.

In order to quantitatively describe the observed phenomena, we introduce a model for the magnon conducivity σ_{m}, containing the superposition of SHE (linear in I_{mod}) and ther-

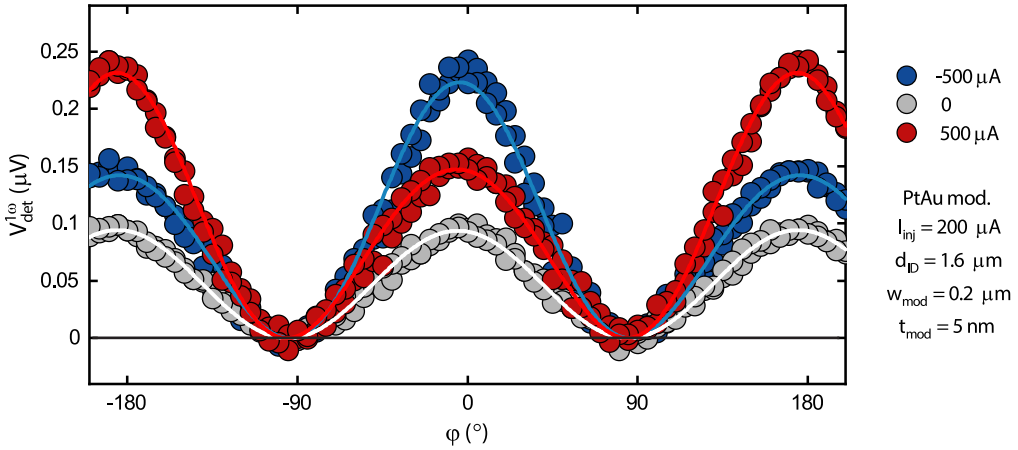

Fig. 5.6: First harmonic detector signal $V_{\mathrm{det}}^{1\omega}$ as a function of the rotation angle φ for a PtAu modulator device at $\mu_0 H = 50\,\mathrm{mT}$. Solid lines are fits to Eq. 5.5.

mal (quadratic in I_{mod}) effects induced by the modulator electrode [17]:

$$\sigma_{\mathrm{m}} = \sigma_{\mathrm{m}}^{0} + \Delta\sigma_{\mathrm{SHE}} I_{\mathrm{mod}} + \Delta\sigma_{\mathrm{th}} I_{\mathrm{mod}}^{2}, \tag{5.2}$$

with σ_{m}^{0} corresponding to the equilibrium magnon conductivity for the zero-current case ($I_{\mathrm{mod}} = 0$), and σ_{SHE} and σ_{th} representing the SHE- and thermally-induced change of the magnon conductivity for finite modulator currents, respectively. Since the detector voltage is proportional to the magnon conductivity, we are able to rewrite Eq. 5.2 and account for the angle-dependent detector voltages $V_{\mathrm{det}}^{1\omega/\mathrm{el}}$ and $V_{\mathrm{det}}^{2\omega/\mathrm{th}}$. However, we must keep in mind that the thermal injection is not dependent on magnetization orientation, whereas the SHE-induced injection scales with $I_{\mathrm{mod}}(-\cos\varphi)$. Thus, we obtain:

$$V_{\mathrm{det}}^{1\omega/\mathrm{el}}(\varphi, I_{\mathrm{mod}}) = \cos^2(\varphi - \varphi_1)\left(\Delta V_{\mathrm{det},0}^{1\omega/\mathrm{el}} + \Delta R_{\mathrm{SHE}}^{1\omega/\mathrm{el}} I_{\mathrm{mod}}(-\cos(\varphi - \varphi_1)) + \Delta R_{\mathrm{th}}^{1\omega/\mathrm{el}} I_{\mathrm{mod}}^{2}\right), \tag{5.3}$$

$$V_{\mathrm{det}}^{2\omega/\mathrm{th}}(\varphi, I_{\mathrm{mod}}) = -\cos(\varphi - \varphi_2)\left(\Delta V_{\mathrm{det},0}^{2\omega/\mathrm{th}} + \Delta R_{\mathrm{SHE}}^{2\omega/\mathrm{th}} I_{\mathrm{mod}}(-\cos(\varphi - \varphi_2)) + \Delta R_{\mathrm{th}}^{2\omega/\mathrm{th}} I_{\mathrm{mod}}^{2}\right). \tag{5.4}$$

Note that the given expressions differ only in the terms in front of the parenthesis, reflecting the angle dependencies of the magnon transport in absence of a modulator as described in Chap. 5.1. The coefficients $\Delta V_{\mathrm{det},0}^{\mathrm{i}}$, $\Delta R_{\mathrm{SHE}}^{\mathrm{i}}$ and $\Delta R_{\mathrm{th}}^{\mathrm{i}}$ correspond to σ_{m}^{0}, σ_{SHE} and σ_{th} from Eq. 5.2, respectively, and serve as proportionality factors accounting for the conversion into voltages [34], where we generally assume that the transport mechanisms for SHE- and thermally-excited magnons are different: $\mathrm{i} = \{1\omega/\mathrm{el}, 2\omega/\mathrm{th}\}$. φ_1 and φ_2 represent the finite angle offsets. Rewriting Eqs. 5.3 and 5.4 with separation of terms with respect to the different angle symmetries, we obtain the fitting equations for the angle dependencies in form of:

$$V_{\mathrm{det}}^{1\omega/\mathrm{el}}(\varphi) = A_1 \cos^2(\varphi - \varphi_1) + B_1 \cos^3(\varphi - \varphi_1), \tag{5.5}$$

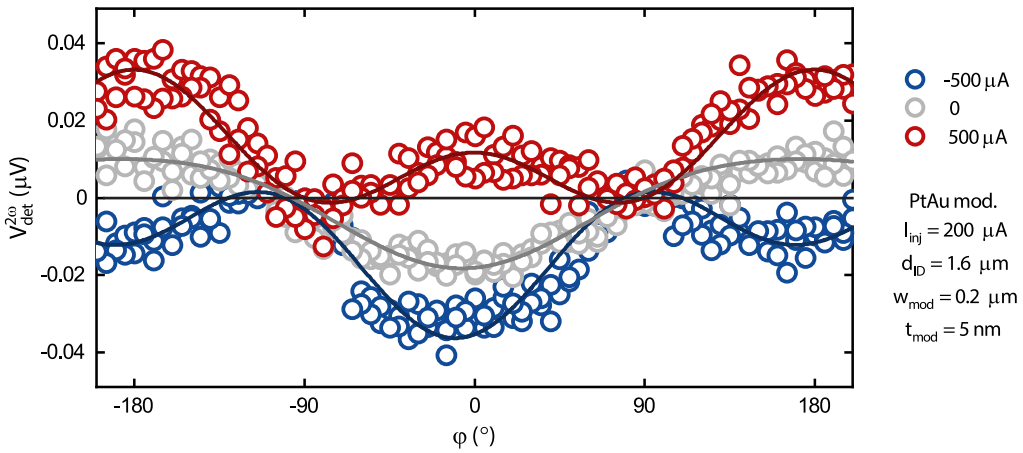

Fig. 5.7: Second harmonic detector signal $V_{\mathrm{det}}^{2\omega}$ as a function of the rotation angle φ for a PtAu modulator device at $\mu_0 H = 50\,\mathrm{mT}$. Solid lines are fits to Eq. 5.6.

$$V_{\mathrm{det}}^{2\omega/\mathrm{th}}(\varphi) = A_2 \cos(\varphi - \varphi_2) + B_2 \cos^2(\varphi - \varphi_2), \tag{5.6}$$

where $A_1 = \Delta V_{\mathrm{det},0}^{1\omega/\mathrm{el}} + \Delta R_{\mathrm{th}}^{1\omega/\mathrm{el}} I_{\mathrm{mod}}^2$, $B_1 = -\Delta R_{\mathrm{SHE}}^{1\omega/\mathrm{el}} I_{\mathrm{mod}}$, $A_2 = -\Delta V_{\mathrm{det},0}^{2\omega/\mathrm{th}} + \Delta R_{\mathrm{th}}^{2\omega/\mathrm{th}} I_{\mathrm{mod}}^2$ and $B_2 = \Delta R_{\mathrm{SHE}}^{2\omega/\mathrm{th}} I_{\mathrm{mod}}$ are used as fit parameters. Figures 5.6 and 5.7 illustrate the angle-dependent electrical $V_{\mathrm{det}}^{1\omega}$ and thermal $V_{\mathrm{det}}^{2\omega}$ contributions, respectively, obtained for measurements of a PtAu modulator device. In both cases, we fitted the corresponding angle dependence from Eqs. 5.5 and 5.6, with the fit results indicated by solid lines and the extracted fit parameters presented in Tab. 5.1. Substituting the values from the obtained parameters for the coefficients from Eqs. 5.3 and 5.4 yields the following values: $\Delta R_{\mathrm{SHE}}^{1\omega} = 82.7\,\mathrm{nV/mA}$, $\Delta R_{\mathrm{th}}^{1\omega} = 368\,\mathrm{nV/mA^2}$ for the electrical contribution and $\Delta R_{\mathrm{SHE}}^{2\omega} = 46.7\,\mathrm{nV/mA}$, $\Delta R_{\mathrm{th}}^{2\omega} = 10.8\,\mathrm{nV/mA^2}$ for the thermal contribution [3)]. The pronounced difference of the parameters obtained from the electrical and thermal contributions implies that the underlying physics for transport of electrically and thermally induced magnons is different, corroborating the results from Ref. [22]. Nevertheless, the phenomenological models presented in Eqs. 5.5 and 5.6 clearly reproduce the measured angle dependence very well, therefore strongly corroborating the theoretical predictions [34, 106].

We must point out that the particular device geometry, as well as the interface quality and durability towards high currents play a crucial role for the transport. The devices used for demonstration are not of equal geometries, therefore causing considerable differences in the magnon transport signals: even if we assume that all Pt injectors/detectors exhibit equal spin Hall efficiency as well as spin current transparency at their interfaces, different distances between injector and detector will alter the transport signal magnitude. For injector-detector distances longer than the magnon diffusion length, we can assume the magnonic spin current to be well described by an exponential-like decay behavior [22] (c.f. Chap. 2.4), causing a strong attenuation of the measured voltage with increasing separation of injector and detector. Due to different modulator geometries and materials, the corresponding heating powers differ significantly from device to device, strongly impac-

[3)] The values are obtained by averaging the values calculated for the opposite I_{mod} polarizations.

Tab. 5.1: Extracted fit parameters for Eqs. 5.5 and 5.6 applied to the data displayed in Figs. 5.6 and 5.7, respectively.

	SHE			thermal		
I_{mod}	A_1(nV)	B_1(nV)	$\varphi_1(^\circ)$	A_2(nV)	B_2(nV)	$\varphi_2(^\circ)$
$-500\,\mu$A	183.0 ± 1.3	40.6 ± 1.4	-4.1 ± 0.4	-12.1 ± 0.5	-24.3 ± 0.6	-10.2 ± 1.2
0	94.0 ± 0.7	0.3 ± 0.7	-5.1 ± 0.4	-14.1 ± 0.4	-4.1 ± 0.4	-6.8 ± 1.6
$500\,\mu$A	189.0 ± 1.1	-42.1 ± 1.2	-5.5 ± 0.3	-10.7 ± 0.5	22.4 ± 0.6	-0.2 ± 1.3

ting all transport parameters. Furthermore, we expect that a larger modulator/YIG interface gives rise to higher spin absorption and a corresponding reduction of the transported magnon spin [17]. Last but not least, the devices were fabricated on different YIG films (c.f. Tab. A.1), which are typically of varying quality in terms of Gilbert damping. That being said, we conclude that it is not straightforward to compare these measurements quantitatively. However, by extracting the signal amplitudes as a function of I_{mod}, we can examine the influence of magnons excited at the modulator on the transport channel of magnons stemming from the injector, as we are going to show in the next Chapter.

5.2 Current-dependent Magnon Transport Measurements

In the previous Section, we reproduced a phenomenological model established in Ref. [17], describing the effects induced by altering the magnon transport due to application of a charge current to a modulator electrode acting as a magnon source/sink. We demonstrated that the predictions of the model are in good agreement with the experiments. However, in order to gain deeper insight about the underlying physics, we strive to gain a deeper insight into the bias current dependence of the magnon transport modulation effect. Since we are already familiar with the angle-dependent behavior, the point of interest for the following type of measurements lies exclusively in the signal amplitudes: we thus measure the amplitudes $\Delta V_{\mathrm{det}}^{1\omega/\mathrm{el}}(\varphi = 0)$ and $\Delta V_{\mathrm{det}}^{1\omega/\mathrm{el}}(\varphi = \pm 180^\circ)$ [$\Delta V_{\mathrm{det}}^{2\omega/\mathrm{th}}(\varphi = 0)$ and $\Delta V_{\mathrm{det}}^{2\omega/\mathrm{th}}(\varphi = \pm 180^\circ)$] for the SHE [thermally] excited magnons as a function of the applied modulator current I_{mod} (c.f. Fig. 5.8 **(a)** and **(d)**). For a particular applied magnetic field direction pointing perpendicular to the electrodes of the device ($\mu_0 \boldsymbol{H}$ or $-\mu_0 \boldsymbol{H}$), an inversion of the modulator current polarization has the same effect as rotating the field by 180°, thus allowing to measure both $\boldsymbol{\mu}_{\mathrm{s}} \parallel \mu_0 \boldsymbol{H}$ and $\boldsymbol{\mu}_{\mathrm{s}} \parallel -\mu_0 \boldsymbol{H}$ cases in one run. It is important to point out that these two cases represent the two limiting cases in terms of magnon transport modulation at the modulator electrode by means of the SHE. The parallel alignment $\boldsymbol{\mu}_{\mathrm{s}} \parallel \mu_0 \boldsymbol{H}$ resembles the case of magnon accumulation illustrated in Fig. 5.1 **(c)** and will be referred to as the *magnon accumulation regime*, whereas the antiparallel alignment $\boldsymbol{\mu}_{\mathrm{s}} \parallel -\mu_0 \boldsymbol{H}$ resembles the case of magnon depletion illustrated in Fig. 5.1 **(d)** and will be referred to as the *magnon depletion regime* [4]. For the sake of clarity, we redefine the amplitudes with respect to the field polarization (perpendicular to the electrodes of the device): $\Delta V_{\mathrm{det}}^{1\omega/\mathrm{el}}(\mu_0 H)$ and $\Delta V_{\mathrm{det}}^{1\omega/\mathrm{el}}(-\mu_0 H)$ /$\Delta V_{\mathrm{det}}^{2\omega/\mathrm{th}}(\mu_0 H)$ and $\Delta V_{\mathrm{det}}^{2\omega/\mathrm{th}}(-\mu_0 H)$, as depicted in Fig. 5.8 **(a)**/**(d)** ($\mu_0 H : \varphi = \pm 180^\circ$,

[4] Note, that in Fig. 5.1 we illustrated the magnetic moment associated with the SHE-induced spin accumulation, rather than the spin accumulation itself. The associated magnetic moment is always pointing in the opposite direction, as compared to the spin accumulation.

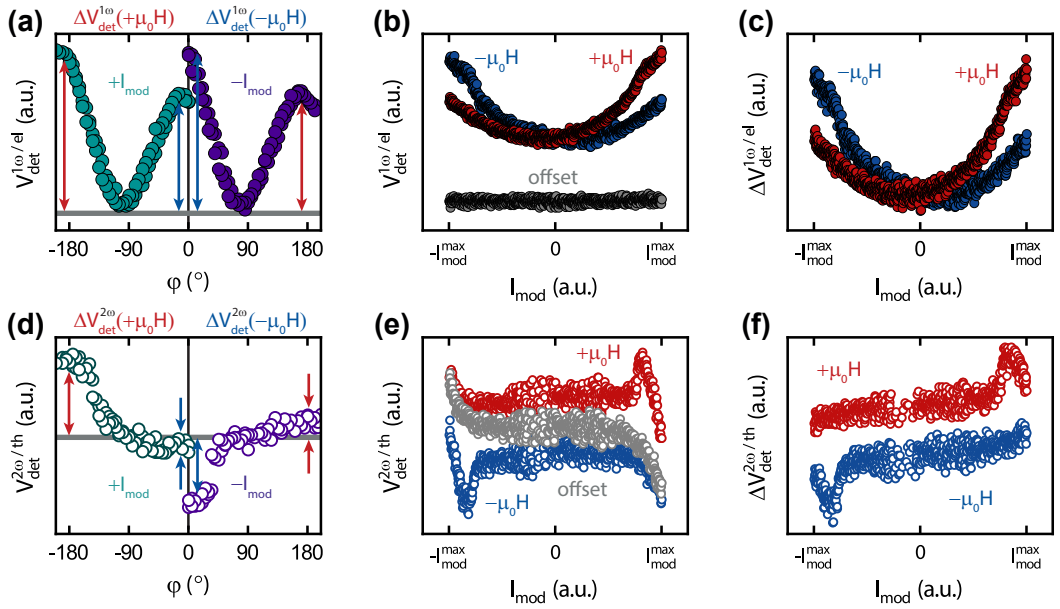

Fig. 5.8: Procedure for obtaining current dependent measurements: **(a)** and **(d)** illustrate the definition of amplitudes with respect to the field direction φ for SHE and thermally injected magnons from the injector, respectively. Note that in case of a non-SHE active material the asymmetry for opposite fields/modulator currents vanishes. **(b)** and **(e)** correspond to the measurements for positive ($\varphi = \pm 180°$) and negative ($\varphi = 0°$) fields (red and blue data points, respectively). Additionally, magnon transport is switched off for the offset sweep ($\varphi = 90°$, grey data points), as indicated by the grey base line in **(a)** and **(b)**, respectively. The magnon transport signal amplitudes are obtained by subtracting the offset from the measurements for positive and negative fields, as shown in **(c)** and **(f)**.

$-\mu_0 H : \varphi = 0$). Nevertheless, the process is always repeated for both field directions, allowing to deduce further information due to symmetries.

As a matter of fact, each of the devices exhibits a finite offset voltage induced by various factors (e.g. influence of measurement setup, conventional Seebeck effect between bondpad and bondwire, etc.). Therefore, a current-dependent measurement actually consists of two separate measurements: we first measure the detector signal with the external field aligned perpendicular to the electrodes, enabling magnon transport with $\varphi = 0, \pm 180°$ (corresponding to $-\mu_0 H$ and $\mu_0 H$, respectively, c.f. Fig. 5.8 **(a)**, **(d)**). Subsequently, we measure the offset signal, where the field is aligned parallel to the electrodes ($\varphi = \pm 90°$), as illustrated in Fig. 5.8 **(b)**, **(e)**. We then obtain the signal amplitudes as $\Delta V_{\mathrm{det}} = V_{\mathrm{signal}} - V_{\mathrm{offset}}$ ($V_{\mathrm{signal}} = V_{\mathrm{det}}(\varphi = 0, \pm 180°)$, $V_{\mathrm{offset}} = V_{\mathrm{det}}(\varphi = \pm 90°)$), as shown in Fig. 5.8 **(c)** and **(f)**. The amplitudes are normalized to the zero current amplitudes $\Delta V^{1\omega/\mathrm{el}}_{\mathrm{det,I_{mod}=0}}$ and $\Delta V^{2\omega/\mathrm{th}}_{\mathrm{det,I_{mod}=0}}$ for the electrical and thermal signal, respectively: $\Delta V^{1\omega/\mathrm{el}}_{\mathrm{det,0}} = \Delta V^{1\omega/\mathrm{el}}_{\mathrm{det}} / \Delta V^{1\omega/\mathrm{el}}_{\mathrm{det,I_{mod}=0}}$ and $\Delta V^{2\omega/\mathrm{th}}_{\mathrm{det,0}} = \Delta V^{2\omega/\mathrm{th}}_{\mathrm{det}} / |\Delta V^{2\omega/\mathrm{th}}_{\mathrm{det,I_{mod}=0}}|$, for SHE and thermally excited magnons, respectively, in order to account for the varying signal amplitudes due to different YIG films and interface spin transparencies, allowing a clearer comparison. Note that the amplitude of the second harmonic signal changes sign, depending on the external field direction (c.f. Fig. 5.8 **(d)**), hence the signal was normalized to the absolute value of the zero current amplitude in order to preserve the original voltage signs. The nanostructured electrodes have shown to be very fragile upon applying charge currents. Moreover, long exposure to large current

densities also lowered the interface quality [106, 115] [5)]. In the following, we are going to separately discuss the modulation of the SHE- and thermally-induced transport.

5.2.1 Transport Modulation of Spin Hall Effect Induced Magnons

In order to discern between electrically (SHE) and thermally induced effects, current dependent magnon transport measurements for a series of devices with different modulator materials were conducted in this thesis. As discussed in Chap. 4.5 and depicted in Fig. 4.11, we covered the range from highly inefficient (Ru and Ti/Al), over relatively efficient (Ir and PtAu) and finally highly efficient (Pt) materials in terms of SHE-based charge-to-spin conversion. The conducted current-dependent measurements are presented in Fig. 5.9. For the sake of a qualitative understanding of the measurements, we fit Eq. 5.3 to the data depicted in Fig. 5.10, with $\varphi = 0, \pm 180°$ for negative and positive magnetic fields, respectively. The angles φ_1 and φ_2 are obtained from fits to the angle-dependent measurements via Eq. 5.5 and are taken into account for the fitting of the current dependent measurements (the signal and offset positions, corresponding to V_{signal} and V_{offset} were corrected for these phases), therefore we set them to zero for the fitting of the current dependent measurements. Furthermore, since the data illustrated in Fig. 5.9 is normalized with respect to the zero current signal $\Delta V_{\mathrm{det},0}^{1\omega/\mathrm{el}}$, we now use the reduced fitting parameters for Eq. 5.3 $\Delta V_{\mathrm{det},0,\mathrm{norm}}^{1\omega/\mathrm{el}} = \Delta V_{\mathrm{det},0}^{1\omega/\mathrm{el}}/\Delta V_{\mathrm{det},0}^{1\omega/\mathrm{el}}$, $\Delta R_{\mathrm{SHE,norm}}^{1\omega/\mathrm{el}} = \Delta R_{\mathrm{SHE}}^{1\omega/\mathrm{el}}/\Delta V_{\mathrm{det},0}^{1\omega/\mathrm{el}}$ and $\Delta R_{\mathrm{th,norm}}^{1\omega/\mathrm{el}} = \Delta R_{\mathrm{th}}^{1\omega/\mathrm{el}}/\Delta V_{\mathrm{det},0}^{1\omega/\mathrm{el}}$. Note that the first parameter is by definition: $\Delta V_{\mathrm{det},0,\mathrm{norm}}^{1\omega/\mathrm{el}} = 1$, however we keep it as a free parameter to ensure a more accurate modeling. The fitting range is indicated by the orange arrowheads, roughly corresponding to the region where the model given by Eq. 5.2 well describes the measurements [18, 106]. For larger I_{mod} currents, we observe effects which cannot be described by this model. For the sake of clarity, only the fits for positive fields (red data points) are shown.

Let us now take a closer look at Fig. 5.9. Starting with the Ti/Al modulator device **(a)**, we first verify that the modulator shows no visible SHE contribution, since the measurements for opposite field and current directions overlap perfectly, therefore indicating an exclusive thermal modulation of the transport (which is symmetric under field reversal). The curve fitted in the low current regime is extrapolated to larger currents, reproducing the measured data well. The same holds for the Ru device, where the corresponding measurement is illustrated in **(b)**. However, due to the significantly larger heating power (as a result of a large resistance of Ru), the quadratic coefficient in Eq. 5.3 is considerably larger compared to the previous case, thus causing a larger increase of the magnon conductivity. For larger currents we observe a local maximum at $I_{\mathrm{mod}} \sim 1.2\,\mathrm{mA}$ for both current and field directions and a subsequent rapid decrease of the signal, even crossing the zero line and inverting its sign. The fit, however, is describing the data well until the signal starts diminishing. In the case of Ir **(c)**, we observe a slight asymmetry for opposite field/current directions, verifying that Ir is exhibiting small but finite SHE efficiency (confirming the finite SMR amplitude extracted for Ir/YIG in Chap. 4.5). Similar to Ru, we observe lo-

[5)] A relatively small maximum charge current was used for the first measurements of a particular device, gradually increasing the maximum current for every successive measurement, and lowering the resolution of the applied current for an already measured current region in order to reduce the device's exposure. For every measurement, the whole range $(-I_{\mathrm{mod}}^{\mathrm{max}}, I_{\mathrm{mod}}^{\mathrm{max}})$ was covered for opposite directions of the external field.

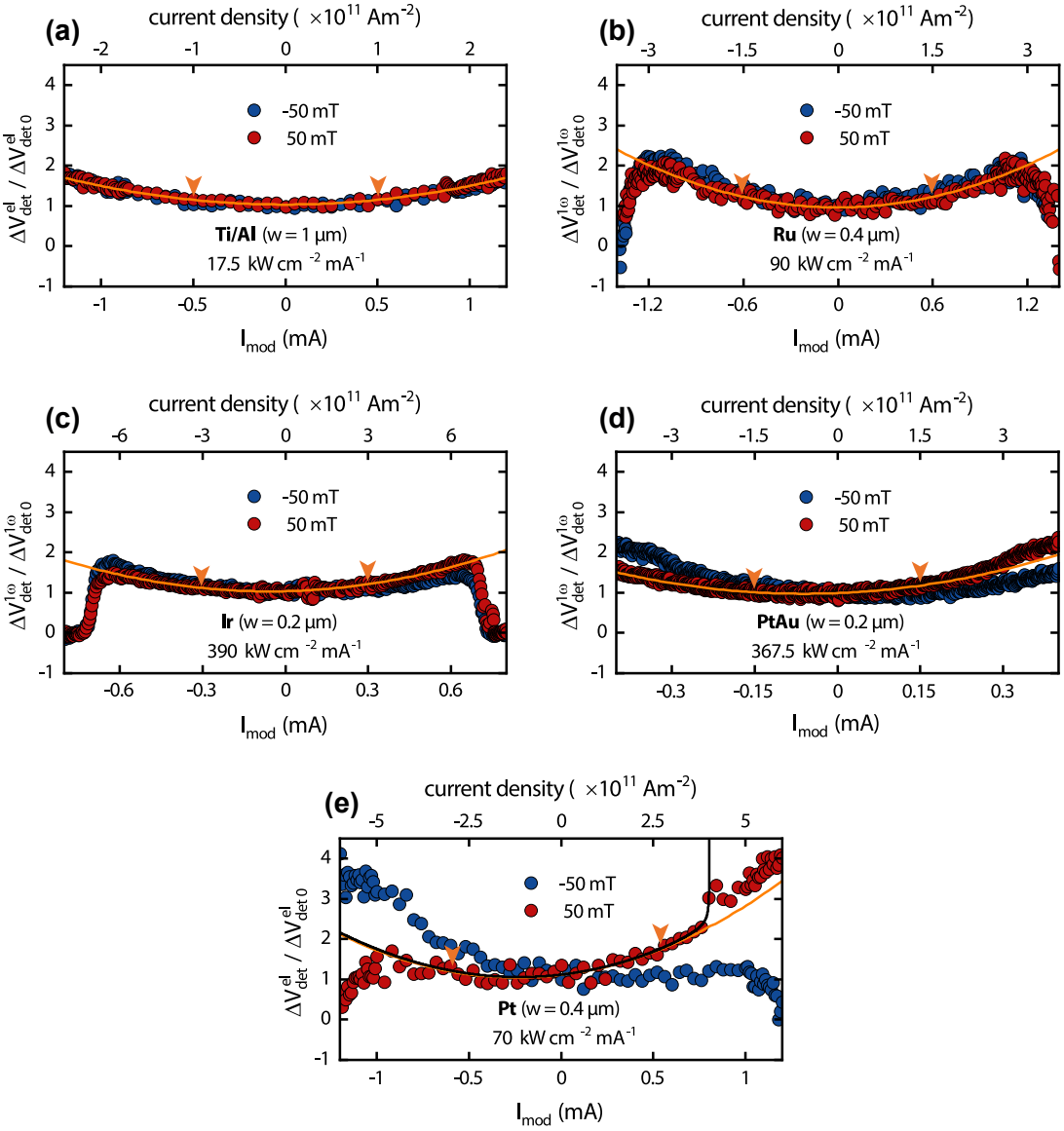

Fig. 5.9: Current dependent normalized signal amplitudes $\Delta V_{\mathrm{det}}^{1\omega/\mathrm{el}}/\Delta V_{\mathrm{det},0}^{1\omega/\mathrm{el}}$ corresponding to the SHE induced magnons at the injector. **(a)**, **(b)**, **(c)**, **(d)** and **(e)** depict the measurements for devices with Ti/Al, Ru, Ir, PtAu and Pt modulator, respectively. The orange solid lines represent fits to Eq. 5.3, with the fitting region being indicated by the orange arrowheads. The black line in **(e)** represents a fit to 5.8. In each panel, the corresponding heat power density (with respect to the interface area and maximal applied current) at the modulator is indicated. In order to keep the plot synoptic, the fits are shown only for the positive field measurements.

cal maxima, after which the signal decreases with increasing modulator current. Different to the Ru device, however, the signal eventually saturates at zero and does not change sign. Again, the fitted curve portrays the data very well until the sudden signal drop. In principle, we can use the temperature-dependence of the resistance of the modulator (injector/detector) to extract the temperature change as a function of applied charge current bias to the modulator. Due to time restrictions, we did not carry out such (thermometry) measurements. However, we can compare our data with the thermometry measurements from Ref. [18] since the YIG samples are of similar thickness and quality and the electrodes are deposited in the same fashion. Our Ir modulator exhibits an approximately 8 times

larger heating power compared to the Pt modulator (for equal applied modulator current bias) from Ref. [18]. Utilizing the values obtained in Ref. [18], we extract for the Ir modulator at maximum current a temperature well above the Curie temperature $T_\mathrm{c} = 559\,\mathrm{K}$ of YIG [116]. Therefore, we conclude that the sudden signal decrease observed in the magnon transport signals corresponds to a phase transition effect of the magnetic system in the YIG layer (at least underneath the modulator electrode): above the ordering temperature, YIG (locally) behaves as a paramagnet, thus long distance magnon transport is no longer possible, resulting in a zero magnon transport signal. Applying the same arguments for the Ru structure, we obtain a similar heating power as for the Pt reference sample from Ref. [18], therefore arguably not reaching the Curie temperature for the Ru device (the approximated temperature underneath the Ru modulator is $480\,\mathrm{K}$). It is important to point out that the devices were fabricated on two different YIG samples, slightly thicker than the reference sample from Ref. [18], where the one with the Ru structure is the thickest one, thus a variation in T_c is plausible for the different devices. The rapid decrease of the signal observed for the Ru device might therefore be rationalized by an additional electric leakage current [117] across YIG itself (c.f. Chap. 5.2.3). The two effects, namely electric leakage currents and magnetic ordering transitions, can both occur in one and the same device in general, we will however see that this observation is indeed due to leakage currents for the Ru device (see Chap. 5.2.3 for details). Owing to the larger SHE efficiency in the PtAu structure **(d)**, the asymmetry for the opposite current/field directions is more distinct as compared to Ir. The data points above $0.3\,\mathrm{mA}$ for the positive field (red data points) deviate from the fitting curve, where the signal changes its slope and increases above the fitting curve. In Ref. [18], this deviation from the expected behavior is characterized by the onset current, where the magnon conductivity modulation enters the critical regime and thus cannot be rationalized within the model given by Eq. 5.2. We conclude that the SHE efficiency in PtAu is sufficient to enter this regime. Finally, considering the Pt structure **(e)**, we observe the same behavior with an even more pronounced asymmetry due to the stronger SHE efficiency. Compared with the other devices, we observe the largest signal amplification. This amplification, however, becomes pronounced only at higher current values (approx. $0.7\,\mathrm{mA}$), where the transport enters the nonlinear regime. By further increasing the modulator current, the signal exhibits a steep rise, corresponding to the maximum slope of the curve. In Ref. [18], the corresponding current is defined as the critical current at which the magnetic damping of YIG is fully compensated and the effective magnon conductivity/resistance diverges/becomes minimal. For materials exhibiting relatively high SHE efficiency, the model described by Eq. 5.2 fails for large modulator currents. In a recent theoretical study [109], this observation of non-linear conductivity modulation was attributed to the formation of a magnon Bose-Einstein Condensate (BEC). An earlier related theory work also considered the threshold behavior of this spin current induced formation of a magnon BEC [107], further corroborating this idea. Without arguing about the possibility of forming a magnon BEC in our samples, we can adapt the additional divergence term $(\mu_\mathrm{crit} - \mu_\mathrm{s})^{-1/2}$ introduced in [109], accounting for the nonlinear behavior in vicinity

of the critical spin chemical potential μ_{crit}[34]:

$$\sigma_{\mathrm{m}} = \sigma_{\mathrm{m}}^{0'} + \Delta\sigma_{\mathrm{SHE}}^{'} I_{\mathrm{mod}} + \Delta\sigma_{\mathrm{th}}^{'} I_{\mathrm{mod}}^{2} + \Delta\sigma_{\mathrm{crit}} \frac{1}{\sqrt{\mu_{\mathrm{crit}} - \mu_{\mathrm{s}}}}, \tag{5.7}$$

where the primed coefficients are slightly deviating from the coefficients defined in Eq. 5.2, due to the additional divergence term. The new coefficient $\Delta\sigma_{\mathrm{crit}}$ reflects the critical magnon conductivity change. As shown in Ref. [34], we can, without loss of generality, exchange $(\mu_{\mathrm{crit}} - \mu_{\mathrm{s}})^{-1/2}$ with $(I_{\mathrm{crit}} - I_{\mathrm{mod}})^{-1/2}$:

$$\sigma_{\mathrm{m}} = \sigma_{\mathrm{m}}^{0'} + \Delta\sigma_{\mathrm{SHE}}^{'} I_{\mathrm{mod}} + \Delta\sigma_{\mathrm{th}}^{'} I_{\mathrm{mod}}^{2} + \Delta\sigma_{\mathrm{crit}}^{'} \frac{1}{\sqrt{I_{\mathrm{crit}} - I_{\mathrm{mod}}}}, \tag{5.8}$$

where $\Delta\sigma_{\mathrm{crit}}^{'}$ represents the coefficient for the critical magnon conductivity change accounting for the conversion to units of magnon conductivity. Rewriting the last equation in a similar fashion as Eq. 5.3, with $\Delta V_{\mathrm{det},0}^{1\omega/\mathrm{el}'}$, $\Delta R_{\mathrm{SHE}}^{1\omega/\mathrm{el}'}$, $\Delta R_{\mathrm{th}}^{1\omega/\mathrm{el}'}$ and $\Delta R_{\mathrm{crit}}^{'}$ corresponding to $\sigma_{\mathrm{m}}^{0'}$, $\sigma_{\mathrm{SHE}}^{'}$, $\sigma_{\mathrm{th}}^{'}$ and $\Delta\sigma_{\mathrm{crit}}^{'}$, respectively, acting as proportionality factors accounting for the conversion into voltages and considering the particular field direction, yields the fitting function used in Fig. 5.9 **(e)**[6]:

$$V_{\mathrm{det}}^{1\omega/\mathrm{el}}(I_{\mathrm{mod}}) = \Delta V_{\mathrm{det},0}^{1\omega/\mathrm{el}'} + \Delta R_{\mathrm{SHE}}^{1\omega/\mathrm{el}'} I_{\mathrm{mod}} + \Delta R_{\mathrm{th}}^{1\omega/\mathrm{el}} I_{\mathrm{mod}}^{2} + \Delta R_{\mathrm{crit}}^{'} \frac{1}{\sqrt{I_{\mathrm{crit}} - I_{\mathrm{mod}}}} \tag{5.9}$$

Evidently, the model presented in Eq. 5.8 agrees well with the data in Fig. 5.9 **(e)**, up to I_{crit}. However, in the data presented here only one data point directly corresponding to I_{crit} is supporting the model, such that the agreement is not fully warranted by the present measurements. In a further data analysis of Ref. [18] presented in Ref. [34], the diverging square root term nicely explains the observed current dependece in the Pt modulator structures. Furthermore, the fitted curve is also in good agreement with the curve corresponding to the thermal and SHE superposition model for lower currents (c.f. 5.2). It is important to notice that the Pt device in the magnon depletion regime (opposite signs of current and field for the used convention) shows a signal dropping to zero for high currents. In the magnon accumulation regime, however, this is not the case. This observation will be addressed in Chap. 5.2.3. In the case of PtAu we did not observe a critical current, even though a clear onset can be recognized, thus indicating that we were not able to reach the current values necessary to acheive a diverging magnon conductance. We must point out that the device broke before higher currents were reached, and it remains unclear whether such a current can be achieved for a PtAu modulator. We can, however, conclude that contrary to the assumptions made in Ref. [106], the observed onset and critical currents cannot be a consequence of the SSE, since the corresponding effects are not obtained for materials exhibiting no or even low SHE efficiency. Thus, our observations support the theoretical prediction of thermally occupied magnons reaching the regime of damping compensation beneath the modulator via the SHE. A pure thermal excitation of magnons via the spin Seebeck torque in the modulator, on the other hand, is not sufficient to induce damping compensation, which is in accordance with Refs. [109, 107].

[6] Again, we take into consideration that the illustrated data is normalized with respect to the zero current signal $\Delta V_{\mathrm{det},0}^{1\omega/\mathrm{el}}$.

5.2.2 Transport Modulation of Thermally Induced Magnons

Figure 5.10 depicts the current dependent measurements of thermally induced magnons corresponding to the same structures discussed in Fig. 5.9. Compared to their electrical counterparts, we immediately notice the opposite signs of the signals for opposite field directions, as well as the fact that the curves exhibit a rather flat structure in the low current regime. An investigation of the behavior of thermally induced magnons will, however, shed light on the features observed for the SHE induced magnons. Let us therefore address the observed effects. First of all, the Ti/Al device **(a)**, does not show any characteristic features, remaining constant over the whole current range investigated. This is in perfect agreement with the SHE induced signal (c.f. Fig. 5.9 **(a)**), where we only observed a weak quadratic increase. Continuing with Ru **(b)**, the signal is first constant, until we reach currents $I_{\mathrm{mod}} > 1\,\mathrm{mA}$ corresponding to the regime at which we observed an abrupt voltage drop in Fig. 5.9 **(b)** for the electrically induced magnons. In this case, however, the signal exhibits an abrupt increase, with the signal sign following the current sign for both field directions. From the discussion following in Chap. 5.2.3 we attribute this to an electrical leakage current flowing in the YIG layer. This observation corroborates the conjecture we put forward for the electrical signals of the Ru device in the previous Section.

In the case of Ir **(c)**, the signal is again constant for low modulator currents. Reaching higher current intensities, we observe a highly interesting behavior: the signals for both field directions exhibit a very steep increase, immediately followed by a very steep decrease. This characteristic peak is more pronounced for the magnon accumulation regime as compared to the magnon depletion case, indicating that the SHE induced effects are playing a considerable role. Furthermore, we observe a change of the signal sign for the peaks. As already discussed, the comparison of the Ir sample with the reference sample from Ref. [18] clearly indicates that the high heating power of the Ir modulator accounts for temperatures above the ordering temperature of YIG (c.f. 5.2.1). The observed characteristic peaks, indicative for phase transitions, additionally verify our assumptions. In this regard, this observation yields an interesting finding. Let us therefore recapitulate the effects observed in the first and second harmonic measurements for the Ir device (c.f. Figs. 5.9 **(c)** and 5.10 **(c)**), which we plot again in Fig. 5.11 **(a)** and **(c)**, in order to allow a clearer overview. For the electrical contribution of the Ir device **(a)** the signal exhibited a very steep but continuous change, whereas in the thermal contribution **(c)**, for equal modulator currents, the signal exhibits a discontinuous but finite peak behavior. This is in perfect agreement with the proposal made in Ref. [34], assuming that the first harmonic signal might be thought of as a measure of the system's entropy, while the second harmonic subsequently could reflect the system's heat capacity [114]. A magnetic second order transition from a ferromagnetic to a paramagnetic state is always accompanied by an increase of the system's entropy, since the ferromagnetic state is by definition more ordered than the paramagnetic state. The continuous increase of entropy subsequently induces a reduction of the magnon conductivity, which we measure as a decrease of $\Delta V_{\mathrm{det}}^{1\omega/\mathrm{el}}$ (c.f. Fig. 5.11 **(a)**). The magnons of the systems are not clearly defined in the paramagnetic state, thus no magnon transport can be observed. The heat capacity of the system reflects the change of entropy during a phase transition in form of a characteristic lambda-shaped peak, with the apex correspon-

ding to the point of the most rapid change of entropy. The asymmetry in **(c)** for opposite current polarization for a particular applied field (positive or negative), again reflects the SHE-symmetry. In the magnon accumulation regime (i.e. more pronounced peak), there are more available particles (magnons and phonons) contributing to the specific heat therefore accounting for a larger change in heat capacity. In the depletion regime (i.e. less pronounced peak), this number is partially reduced (due to depletion of magnons), explaining the comparably lower peak.

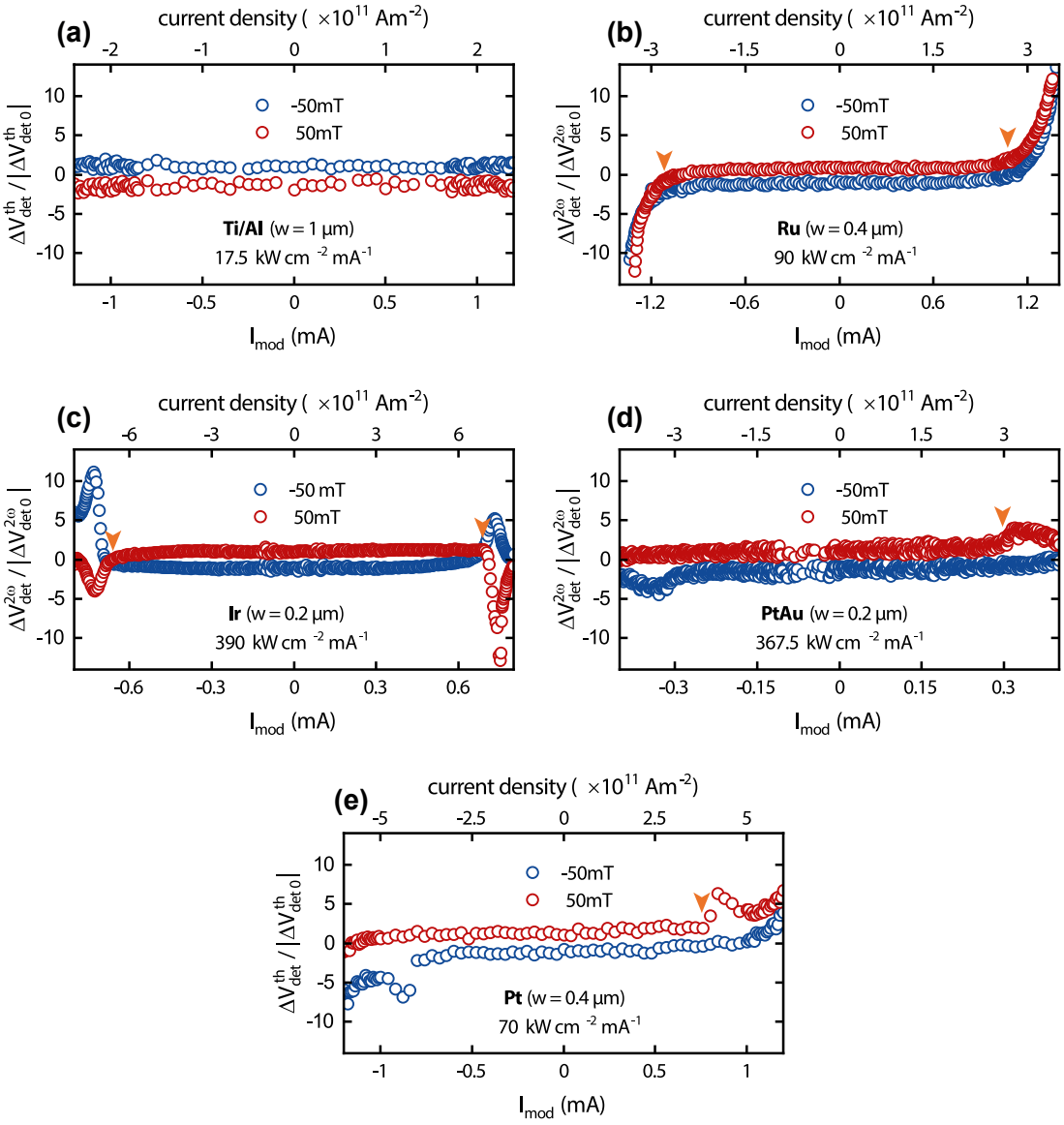

Fig. 5.10: Current dependent normalized signal amplitudes $\Delta V_{\mathrm{det}}^{2\omega/\mathrm{th}}/|\Delta V_{\mathrm{det},0}^{2\omega/\mathrm{th}}|$ corresponding to thermally induced magnons at the injector. **(a)**, **(b)**, **(c)**, **(d)** and **(e)** depict the measurements for devices with Ti/Al, Ru, Ir, PtAu and Pt modulators, respectively. The orange arrowheads indicate the modulator current values at which we start observing the characteristic features in the SHE counterparts shown in Fig. 5.9. In order to keep the plot synoptic, the marks are shown only for the positive field measurements.

This proposal [34] arose for measurements qualitatively corresponding to our measurements of the PtAu **(d)** and Pt **(e)** devices shown in Fig. 5.10. Obviously, Pt and PtAu exhibit mutually equal features in the thermal contribution, thus we are going to restrict the dis-

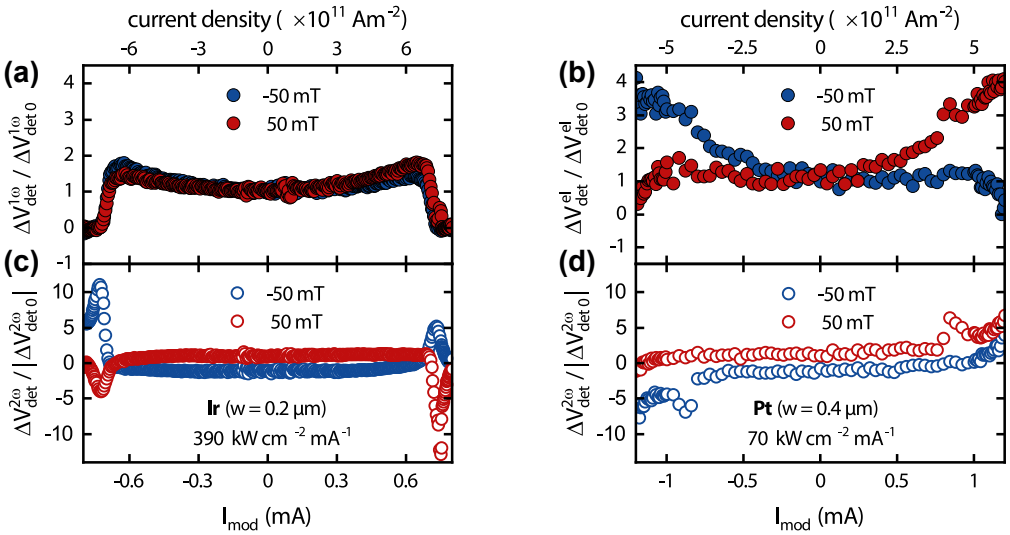

Fig. 5.11: Current dependent normalized signal amplitudes $\Delta V_{\mathrm{det}}^{1\omega/\mathrm{el}}/\Delta V_{\mathrm{det},0}^{1\omega/\mathrm{el}}$ and $\Delta V_{\mathrm{det}}^{2\omega/\mathrm{th}}/|\Delta V_{\mathrm{det},0}^{2\omega/\mathrm{th}}|$) corresponding to the SHE and thermally induced magnons at the injector, respectively. **(a)** and **(c)**/ **(b)** and **(d)** are showing the SHE and thermal contributions for an Ir/Pt device, respectively.

cussion to the Pt device. For the sake of better comparison, the electrical (c.f. Fig. 5.9 **(e)**) and thermal (c.f. Fig. 5.10 **(e)**) contributions of the Pt device are replotted in Fig. 5.11 **(b)** and **(d)**. In the thermal contribution **(d)**, we observe a characteristic peak for both positive (red data points) and negative (blue data points) field measurements. However, the characteristic peaks appear only in the magnon accumulation regime. Furthermore, the signal signs are preserved, with the signal exhibiting no sign change for the arising peaks. A comparison with the electrical contribution **(b)** reveals that the characteristic peaks in the thermal contribution occur for I_{mod} at which we observe the onset of nonlinear behavior in the electrical contribution. Attributing this nonlinearity to the damping compensation, we would expect a decrease of the entropy of the system, leading to an increase of the magnon conductivity. We confirm this by measuring an increased $\Delta V_{\mathrm{det}}^{1\omega/\mathrm{el}}$ (c.f. 5.11 **(b)**). The thermal contribution, if considered as a measure of the system's heat capacity, should then exhibit the observed characteristic (lambda-shaped) peak. By this, we assume that the damping compensation can be regarded as a phase transition within the magnon system, but is not to be mistaken with a second order magnetic phase transition at T_{c}.

It is important to point out that further measurements must be carried out in order to verify the hereby offered assumptions, nevertheless the overall picture seems to be consistent.

5.2.3 Leakage Currents

In this Section, we address the impact of electric leakage currents on the magnon transport modulation measurements discussed in the preceeding Sections. Sizable contributions from electric currents flowing between the metallic electrodes across YIG should be suppressed due to the insulating nature of YIG [118] and the GGG substrate [119]. It is known, however, that doping performed as for semiconductors (i.e. intentional implanting of impurities introducing energy levels inside and close to the edges of the forbidden gap,

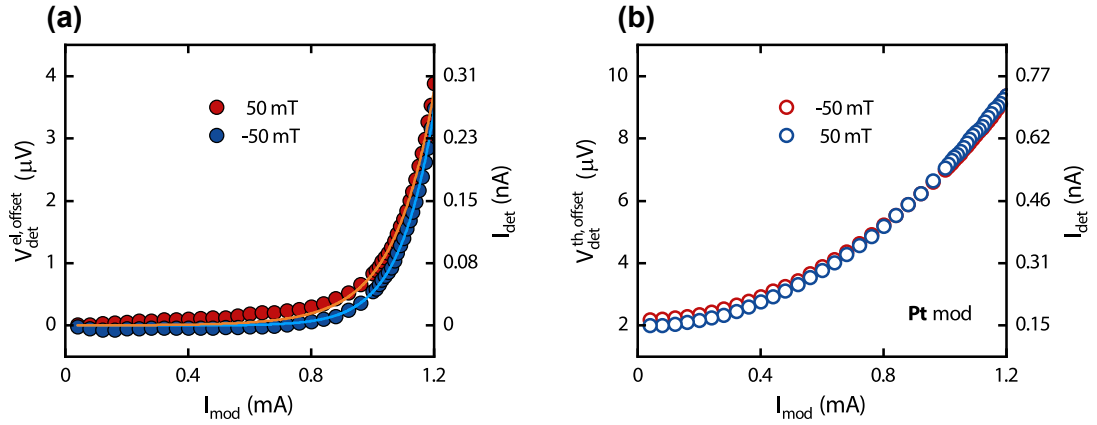

Fig. 5.12: Offset voltage measurements of the Pt device shown in Figs. 5.9 **(e)** and 5.10 **(e)**. The hereby presented measurements are obtained by setting $I_{\mathrm{inj}} = 0$ and applying I_{mod} to the modulator electrode while simultaneously measuring the voltage response V_{det} at the detector electrode. **(a)** and **(b)** show the corresponding electric and thermal detector signals. The solid lines in **(a)** are fits to Eq. 5.12.

therefore mitigating the interband transition of charge carriers) can lead to a substantial increase of conductivity for YIG [120, 121, 122]. In the case of ultrathin films, as used for our magnon transport experiments, defects could be introduced as a consequence of the fabrication, due to the usage of resists or even due to the NM/YIG interfaces. A recent study [117] reported that the electrical conductivity in a 19 nm-thick YIG sample increased exponentially with increasing temperature, following an activated semiconductor-like behavior corresponding to a band gap of $E_{\mathrm{g}} \approx 2\,\mathrm{eV}$. In our corresponding experiment, we experience a large temperature increase of the sample due to the application of very large modulator current densities leading to Joule heating of the devices [18]. Thus, we are going to treat our YIG sample as an intrinsic semiconductor allowing for an explanation of the experimentally observed behavior at large current densities. The obtained model will be applied quantitatively to the experiments and the results will be discussed.

For an intrinsic semiconductor, we can introduce the temperature dependent charge carrier density as [123]:

$$n_{\mathrm{i}} \propto T^{3/2} \exp\left(-\frac{E_{\mathrm{g}}}{2k_{\mathrm{B}}T}\right) \tag{5.10}$$

Since the corresponding conductivity σ is given as the product of the carrier density, carrier mobility and elementary charge, i.e. $\sigma = n_{\mathrm{i}}\mu e$, with the mobility exhibiting a $\mu \propto T^{-3/2}$ temperature dependence [123], we obtain:

$$\sigma \propto \exp\left(-\frac{E_{\mathrm{g}}}{2k_{\mathrm{B}}(T_0 + c_{\mathrm{JH}}I_{\mathrm{mod}}^2)}\right), \tag{5.11}$$

where $T = T_0 + c_{\mathrm{JH}}I_{\mathrm{mod}}^2$ accounts for the current induced Joule heating of the modulator electrode, with $T_0 = 280\,\mathrm{K}$ in our experiments and c_{JH} parametrizing the electrode's current-heating coefficient. Let us first consider the case where a DC current is applied to the modulator and a voltage is measured simultaneously at the detector (here, we apply an external field parallel to the electrodes, which suppresses magnon transport and thus enables the investigation of purely electrical leakage effects between the modulator and detector). This corresponds to the experiment conducted in Ref. [117]. Upon increasing the

applied current, the system heats as dictated by Joule's heating law and thus causes an increase of the available charge carriers in the YIG semiconductor. Similar to our magnon transport measurements, where the increased detector voltage indicates an increased conductivity of the magnonic system rather than an increase of the resistivity, the detector signal is also going to increase with increasing conductivity of YIG:

$$V_{\mathrm{det}}(I_{\mathrm{mod}}) \propto I_{\mathrm{mod}} \cdot \sigma(I_{\mathrm{mod}}) \propto I_{\mathrm{mod}} \exp\left(-\frac{E_{\mathrm{g}}}{2k_{\mathrm{B}}(T_0 + c_{\mathrm{JH}} I_{\mathrm{mod}}^2)}\right). \tag{5.12}$$

Therefore, we expect a thermally activated behavior for temperatures close to $T \sim E_{\mathrm{g}}/(2k_{\mathrm{B}})$. In general, we can write the detector voltage as a Taylor series expansion with respect to the applied current I:

$$V_{\mathrm{det}}(I_{\mathrm{mod}}) = V_0 + \frac{\mathrm{d}V_{\mathrm{det}}}{\mathrm{d}I_{\mathrm{mod}}} I_{\mathrm{mod}} + \frac{1}{2}\frac{\mathrm{d}^2 V_{\mathrm{det}}}{\mathrm{d}I_{\mathrm{mod}}^2} I_{\mathrm{mod}}^2 + \dots \tag{5.13}$$

If we now consider the case of leakage currents for our three-electrode magnon transport experiments, it is important to point out that all electrodes will be mutually shorted when the YIG becomes conducting. Hence, in a simplified picture the total electric leakage current can be thought as a superposition of the injector and modulator currents. The electrical and thermal signal contributions originating from leakage current effects, as defined in Chap. 3.3.2, are then proportional to the first and second derivative of the detector voltage with respect to the applied modulator current as written in Eq. 5.13, respectively. For the electrical signal contribution we therefore obtain:

$$V_{\mathrm{det}}^{1\omega/\mathrm{el}} \propto \frac{\mathrm{d}V_{\mathrm{det}}}{\mathrm{d}I_{\mathrm{mod}}} \propto \left(1 + \frac{E_{\mathrm{g}} c_{\mathrm{JH}}}{k_{\mathrm{B}}}\left(\frac{I_{\mathrm{mod}}}{T_0 + c_{\mathrm{JH}} I_{\mathrm{mod}}^2}\right)^2\right) \exp\left(-\frac{E_{\mathrm{g}}}{2k_{\mathrm{B}}(T_0 + c_{\mathrm{JH}} I_{\mathrm{mod}}^2)}\right), \tag{5.14}$$

wheras for thermal contribution we compute:

$$V_{\mathrm{det}}^{2\omega/\mathrm{th}} = \frac{\mathrm{d}^2 V_{\mathrm{det}}}{\mathrm{d}I_{\mathrm{mod}}^2} \propto \left(1 + \frac{2T_0}{T_0 + c_{\mathrm{JH}} I_{\mathrm{mod}}^2} + \frac{c_{\mathrm{JH}} I_{\mathrm{mod}}^2}{T_0 + c_{\mathrm{JH}} I_{\mathrm{mod}}^2}\left(\frac{E_{\mathrm{g}}}{k_{\mathrm{B}}(T_0 + c_{\mathrm{JH}} I_{\mathrm{mod}}^2)} - 2\right)\right) \times \\ \times \frac{E_{\mathrm{g}} c_{\mathrm{JH}} I_{\mathrm{mod}}}{k_{\mathrm{B}}(T_0 + c_{\mathrm{JH}} I_{\mathrm{mod}}^2)^2} \exp\left(-\frac{E_{\mathrm{g}}}{2k_{\mathrm{B}}(T_0 + c_{\mathrm{JH}} I_{\mathrm{mod}}^2)}\right). \tag{5.15}$$

To conclude, according to Eq. 5.12 we expect the electrical leakage current in the modulator-detector configuration to show a thermally activated behavior given by the exponential term multiplied by the modulator current. The first and second harmonic signals should exhibit the same thermally activated behavior with different symmetries with respect to the modulator current according to Eqs. 5.14 and 5.15. We thus expect the first and second harmonic signals to be even and odd in terms of the modulator current, respectively. In order to verify these findings, we extracted the offset detector voltages $V_{\mathrm{det}}^{\mathrm{el,offset}}$ and $V_{\mathrm{det}}^{\mathrm{th,offset}}$ (where magnon transport is suppressed) for an exclusively applied modulator current (i.e. $I_{\mathrm{inj}} = 0$) from our DC measurements of the Pt modulator device corresponding to the measurements displayed in Figs. 5.9 **(e)** and 5.10 **(e)**, moreover showcasing the versatility of the DC measurement method introduced in Chap. 3.3.1. As illustrated in Fig. 5.12 **(a)**, the detec-

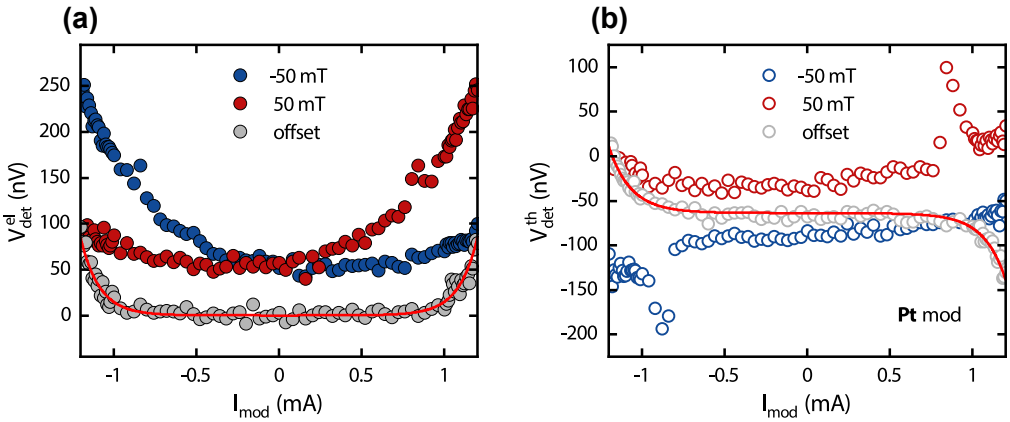

Fig. 5.13: Current dependent measurements of the Pt device shown in Fig. 5.12, in the standard measurement configuration. **(a)** and **(b)** represent the electric and thermal detector signals, respectively, obtained for magnon transport (blue and red data points, corresponding to negative and positive fields, respectively) as well as for the offset (grey data points) measurements. The solid red lines overlapping the offset data points in **(a)** and **(b)** correspond to fits to Eqs. 5.14 and 5.15, respectively. By subtracting the offset from the magnon transport signals, for **(a)** and **(b)**, we obtain Figs. 5.9 **(e)** and 5.10 **(e)**, respectively.

tor signal corresponding to an electrical leakage current is well described by the solid lines representing fits to Eq. 5.12. Furthermore, both electric **(a)** and thermal **(b)** contributions are in perfect agreement with the results from Ref. [117]. By fitting the data corresponding to the electric contribution with the curve described by Eq. 5.12 we extract a bandgap value of $E_g = (0.95 \pm 0.06)\text{eV}$ and heating power of $c_{JH} = (139.8 \pm 37.7)\text{KmA}^{-2}$. The smaller bandgap value of our sample, compared to the findings from Ref. [117] ($E_g \approx 2\,\text{eV}$), indicates that our sample was most probably more contaminated by impurities. This could offer an explanation why leakage currents are observed randomly, i.e. for the Pt device (Fig. 5.9 **(e)**) we unambiguously observe a leakage current, while we cannot point out the same for the Ir device (Fig. 5.9 **(c)**) being a clearly more effective heater. On the other hand, NM/YIG interfaces impose potential barriers for conducting electrons, which could considerably differ depending on the choice of the NM, since the interface quality is clearly affected by the choice of the NM. The heating power coefficient extracted from the fit is in excellent agreement with the heating power $c'_{JH} \approx 133\,\text{KmA}^{-2}$ obtained by comparison with the thermometry measurements from Ref. [34]. It is not straightforward to describe the real leakage current path, which is of crucial importance for the exact determination of the YIG's conductivity, but we can compare the modulator and detector currents by assuming that they are proportional to the conductivities of Pt and YIG, respectively, as a first approximation. In doing so, we obtain $\sigma_{YIG} \approx 0.15\,\text{Sm}^{-1}$ ($\sigma_{Pt} = 2.15\,\text{MSm}^{-1}$) for $I_{mod} = 1.05\,\text{mA}$, corresponding to $T \approx 400\,\text{K}$. Compared to the value $\sigma_{YIG} \approx 0.02\,\text{Sm}^{-1}$ from Ref. [117] obtained at the same temperature, and taking into account the smaller bandgap, we can conclude that our approximation is good enough for obtaining a qualitative picture. Let us now take a look at the current dependent measurement of the Pt structure presented in Figs. 5.9 **(e)** and 5.10 **(e)**. In Fig. 5.13, measurements of the detector signals $V_{det}^{1\omega}$ **(a)** and $V_{det}^{2\omega}$ **(b)**, without subtraction of the indicated offset signals, are presented. Our semiconductor model is describing the offset in the electric contribution **(a)** (Eq. 5.14) as well as the offset in the thermal

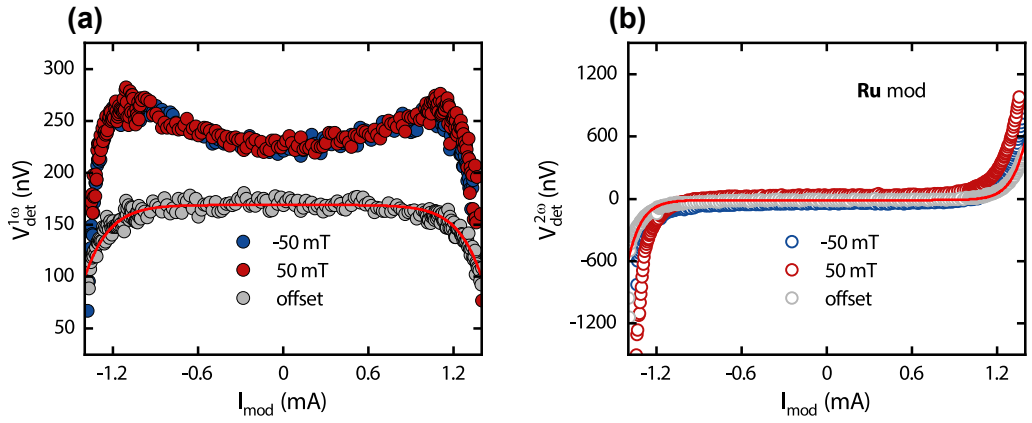

Fig. 5.14: Current dependent measurements of the Ru device shown in Figs. 5.9 **(b)** and 5.10 **(b)**, prior subtracting the offset. **(a)** and **(b)** represent the electric and thermal detector signals, respectively, obtained for magnon transport (blue and red data points, corresponding to negative and positive fields, respectively) as well as for the offset (grey data points) measurements. The solid red lines overlapping the offset data points in **(a)** and **(b)** correspond to fits to Eqs. 5.14 and 5.15, respectively. Contacts on the modulator electrode were interchanged, as compared to the convention used in this thesis (c.f. 5.1 **(a)**). For the opposite polarization of I_{mod}, we see an inversion of the leakage currents effects, compared to 5.13.

contribution **(b)** (Eq. 5.15) up to high accuracy (grey data points). As expected, the offset in the electric contribution is even, whereas the offset in the thermal contribution is odd with respect to the modulator current. In order to ultimately prove the leakage current assumption, we conducted the same measurements with mutually interchanging the contacts of the modulator electrode. This was carried out for the current dependent measurements of a device with a Ru modulator, shown in Fig. 5.14. In the first harmonic contribution **(a)** we observe a sign change for the high current part, as compared to the Pt device in Fig. 5.13, with the symmetry with respect to the current being preserved. The same can be observed for the offset in the second harmonic contribution **(b)**. This is in perfect agreement with our expectations, since the first harmonic, as defined in Eq. 5.14, is proportional to the first derivative of the voltage with respect to the applied current. Even though the signal itself is even with respect to the modulator current, we obtain a minus sign when calculating the first derivative. As for the second harmonic offset, the change of sign is reflecting the odd symmetry with respect to the current. That being said, we can conclude that our model is justified.

Finally, it is important to address the issue of finite alteration of the magnon transport due to leakage currents. Since the idea of an offset measurement is to gain the ability to subtract the eventual offset, one would expect that the magnon transport signal should be cleared of all other possible effects. However, in the previously presented measurement, we saw that this is not the case, since we still see features caused by the leakage currents (c.f. **(b)**, **(e)** of Figs. 5.9 and 5.10). The first candidate for such a behavior is the $180°$-symmetric AMR. Under usual conditions, YIG is a ferromagnetic insulator and therefore not susceptible to AMR. However, in the presence of leakage currents, YIG may act as a semiconducting ferromagnet, therefore possibly exhibiting AMR. In order to check whether AMR is the cause of our issue, we plotted $(V_{\mathrm{det}}^{\mathrm{el}} - V_{\mathrm{det}}^{\mathrm{el,offset}})/V_{\mathrm{det}}^{\mathrm{el}}$ as a function of the modulator current, for the previously shown Pt device. The result is plotted in Fig. 5.15: for high current inten-

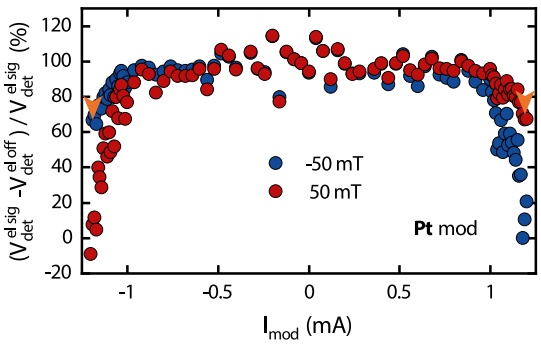

Fig. 5.15: Relative size of the offset voltages, compared to the magnon transport signal corresponding to the measurements portrayed in Fig. 5.13. The orange arrowheads indicate the magnon accumulation regime for the largest applied modulator currents I_{mod}.

sities in the magnon accumulation regime (as indicated by the arrows), the offset signal is almost half as large as the magnon transport signal, with an approximately 40% amplitude. In the magnon depletion regime where the transport signal is reduced, the offset is of equal amplitude as the transport signal, therefore totally suppressing the transport. However, reported AMR amplitudes for semiconducting ferromagnets are in the few-percent regime [124], thus we can very likely rule out AMR as the main cause of the observed effect.

Another possible cause are aging effects of the device. Since it is not possible to simultaneously measure transport and the offset signal, we expect the NM/YIG interface to lower in quality for every successive measurement, when applying high current densities to the electrodes. This is indeed observed during this research, as well as in previous projects [125]. Furthermore, taking into account that applying high currents to the modulator electrode gives rise to Oersted fields of amplitudes up to few mT [126], we can state that the sample's magnetization is not perfectly aligned along the external field's direction. However, additional measurement sensitive to these effect should be conducted, which is beyond the scope of this thesis.

5.2.4 Modulation efficiency

In the previous Section, we discussed and illustrated magnon conductivity measurements, where the conductivity was tuned by altering the number of magnons. This was achieved by utilizing thermal generation of magnons and SHE-induced magnon accumulation or depletion in a modulator electrode. In this Section, we want to disentangle the thermal and SHE contribution. As we already stated, the thermal contribution is odd, and the SHE contribution even under current reversal. However, the same symmetry is reflected in the field symmetry- therefore we are able to extract the modulation amplitudes of the particular effect, without losing information for the opposite current polarization. Thus, we can obtain the modulation amplitude due to SHE and thermal injection as [34, 17]:

$$\Delta V_{\mathrm{det}}^{\mathrm{SHE}} = \frac{\Delta V_{\mathrm{det}}^{1\omega/\mathrm{el}}(+\mu_0 H) - \Delta V_{\mathrm{det}}^{1\omega/\mathrm{el}}(-\mu_0 H)}{2} \propto \Delta\sigma_{\mathrm{SHE,j}} j_{\mathrm{mod}}, \tag{5.16}$$

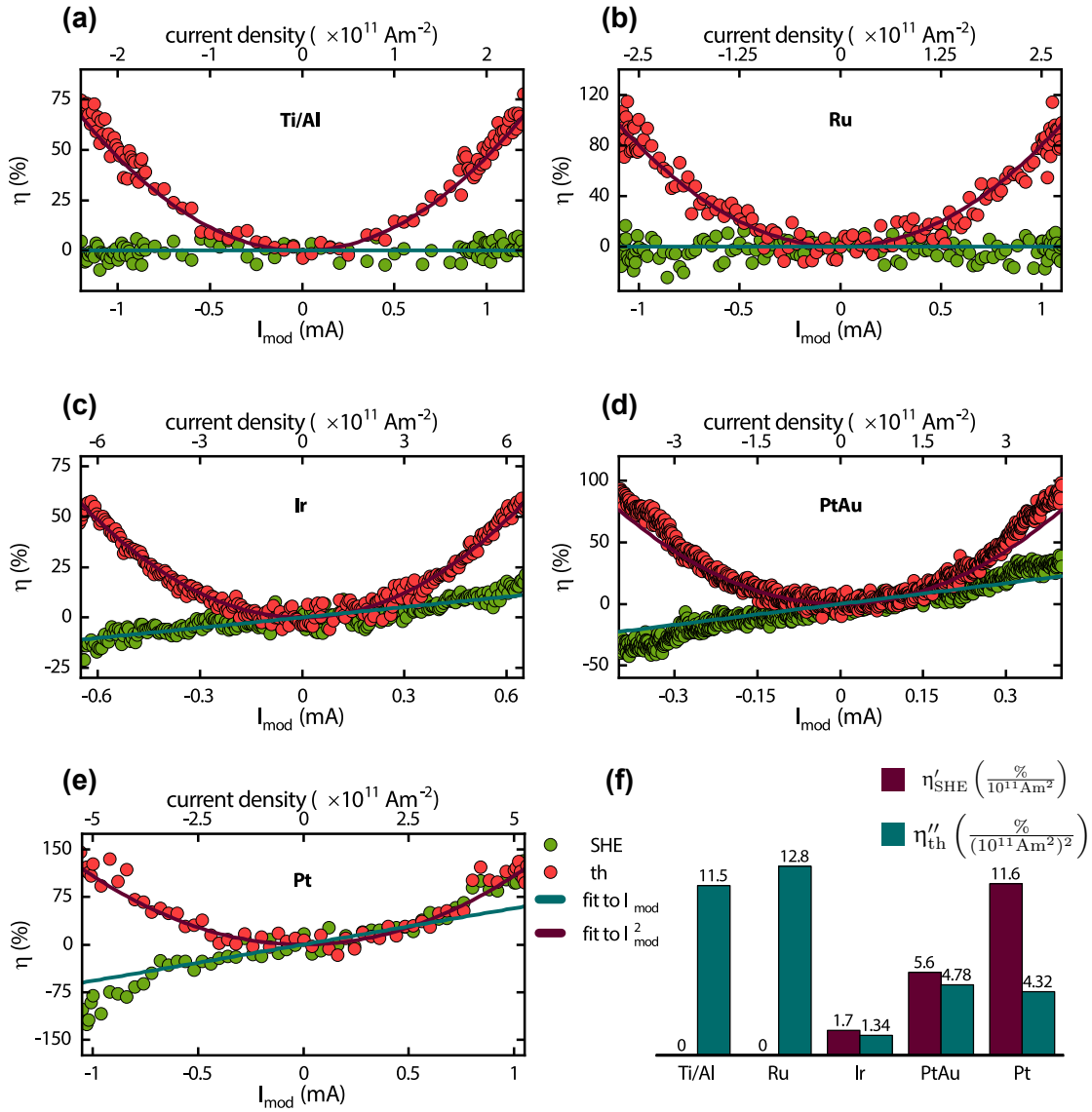

Fig. 5.16: Modulation strengths extracted from the measurements shown in Fig. 5.9, following the formalism given by Eqs. 5.18 and 5.19, for SHE and thermal injection, respectively. **(a)**, **(b)**, **(c)**, **(d)** and **(e)** correspond to Ti/Al, Ru, Ir, PtAu and Pt devices. The modulation efficiencies extracted by fitting the corresponding current density dependence are summarized in **(f)**.

$$\Delta V_{\mathrm{det}}^{\mathrm{th}} = \frac{\Delta V_{\mathrm{det}}^{1\omega/\mathrm{el}}(+\mu_0 H) + \Delta V_{\mathrm{det}}^{1\omega/\mathrm{el}}(-\mu_0 H)}{2} \propto \sigma_0 + \Delta\sigma_{\mathrm{th,j}} j_{\mathrm{mod}}^2, \tag{5.17}$$

respectively. By normalizing these modulation amplitudes according to:

$$\eta_{\mathrm{SHE}} = \frac{\Delta V^{\mathrm{SHE}}}{\Delta V_{\mathrm{det},0}^{1\omega/\mathrm{el}}} = \frac{\Delta\sigma_{\mathrm{SHE,j}} I_{\mathrm{mod}}}{\sigma_0} = \frac{\sigma_{\mathrm{m}}^{\mathrm{SHE}}}{\sigma_{\mathrm{m}}^{0}}, \tag{5.18}$$

$$\eta_{\mathrm{th}} = \frac{\Delta V^{\mathrm{th}} - \Delta V_{\mathrm{det},0}^{1\omega/\mathrm{el}}}{\Delta V_{\mathrm{det},0}^{1\omega/\mathrm{el}}} = \frac{\Delta\sigma_{\mathrm{th,j}} I_{\mathrm{mod}}^2}{\sigma_0} = \frac{\sigma_{\mathrm{m}}^{\mathrm{th}}}{\sigma_{\mathrm{m}}^{0}}, \tag{5.19}$$

where $\Delta V_{\mathrm{det},0}^{1\omega/\mathrm{el}} \propto \sigma_{\mathrm{m}}^{0}$, we obtain the relative modulation strengths for SHE and thermal magnons, which are defined as the ratios of the corresponding induced magnon conductivity ($\Delta\sigma_{\mathrm{SHE,j}} j_{\mathrm{mod}}$ and $\Delta\sigma_{\mathrm{th,j}} j_{\mathrm{mod}}^{2}$, for SHE and thermal induction, respectively) and the magnon conductivity in thermal equilibrium σ_{m}^{0}. Contrary to the previous Sections, where the figure of merit for the transport modulation was the modulator current intensity I_{mod}, in this Section we rather use the modulator current density j_{mod}, since we now want to quantitatively compare the modulation strengths and efficiencies for different modulator geometries. We calculated the relative modulation strengths only for the current dependent measurements of the electrical contribution, since the thermal contribution has shown to be less influenced by the modulator in general (recall the flat structure for the low current bias in Fig. 5.10). In Fig. 5.16 we present the modulation strengths as a function of the modulator current (density) for the devices discussed in the previous Sections. We can see that all devices have a pronounced thermal modulation, following the expected quadratic current dependence. Beside the SHE inefficient Ti/Al and Ru devices, the linear current dependence is fulfilled as well, at least in the low modulator current regime. We can then define the modulation efficiencies as:

$$\frac{\mathrm{d}\eta_{\mathrm{SHE}}}{\mathrm{d}j_{\mathrm{mod}}} = \frac{\Delta\sigma_{\mathrm{SHE,j}}}{\sigma_{\mathrm{m}}^{0}}, \tag{5.20}$$

$$\frac{1}{2}\frac{\mathrm{d}^{2}\eta_{\mathrm{th}}}{\mathrm{d}j_{\mathrm{mod}}^{2}} = \frac{\Delta\sigma_{\mathrm{th,j}}}{\sigma_{\mathrm{m}}^{0}}. \tag{5.21}$$

The defined modulation efficiencies were obtained by fitting the modulation strength with the proper current (density) dependence (linear for SHE and quadratic for thermal modulation) in the low current regime. The obtained values are depicted in Fig. 5.16 **(f)**. By comparing the SHE efficiencies of the different modulators (purple bars) and neglecting the SHE inefficient Ti/Al and Ru devices, we see that Ir is the least efficient with 1.7%, followed by PtAu with 5.6%, whereas Pt exhibits the highest efficiency of 11.6% per $10^{11}\mathrm{Am}^{-2}$ modulator current density. These results qualitatively reproduce the observations from Chap. 4.5, were we characterized the SHE efficiencies by means of SMR measurements (c.f. Fig. 4.11), very well. In Ref. [17], simulations predicted an SHE efficiency of $\sim 16\,\%\mathrm{mA}^{-1}$ for a $10\,\mathrm{nm}$-thick YIG film for an external field $\mu_0 H = 50\,\mathrm{mT}$. All three of our SHE active devices (Ir, PtAu, Pt) were grown on $\sim 20\,\mathrm{nm}$ thick films, with the measurements conducted at $\mu_0 H = 50\,\mathrm{mT}$. By recalculating the SHE efficiencies (c.f. Eq. 5.20) with respect to the modulator current intensity I_{mod}, we obtain efficiency values of 17%, 56% and 58% per mA for Ir, PtAu and Pt, respectively. Thus, all devices are exceeding the expectations made in Ref. [17]. However, it is important to point out that for a proper comparison of devices with different modulator geometries, one must define the modulation efficiency with respect to the applied charge current density, rather than the current intensity, since the SHE depends on the former (c.f. Eq. 2.3).

The obtained thermal efficiencies shown in Fig. 5.16 **(f)** (green bars) should not be understood as quantities merely reflecting the modulator's heating power. If we consider the definition of η_{th}'' (c.f. Eq. 5.21), it becomes obvious that this quantity reflects the ratio of the thermally induced magnon conductivity $\Delta\sigma_{\mathrm{th,j}}$ and the the magnon conductivity in

thermal equilibrium σ_{m}^{0}. Since we are considering the electrical transport contribution, σ_{m}^{0} represents the magnon conductivity in thermal equilibrium of the SHE-induced magnons. Thus, η_{th}'' does not reflect the heating powers of the different devices in general. We see that for the Ir device, which was shown to have the highest heating power of all devices, η_{th}'' is minimal, whereas the Ti/Al device with the lowest heating power among all devices has a pronounced thermal efficiency η_{th}''.

5.3 Summary

In this Chapter, we intensively investigated the electrical and thermal contributions of the magnon transport modulation by utilizing modulator electrodes of different NMs. In the beginning of the Chapter, we addressed the currently open questions regarding this topic, especially the nonlinearities observed in Refs. [18] and [106], and offered a phenomenological description of the relevant physics at the modulator/YIG interface. Subsequently, we presented angle dependent measurements of the electrical and thermal contributions for a two-strip device (c.f. Chap. 5.1). We showcased the principles of magnon transport and qualitatively explained the observed features, as well as offered intuitive explanations for the field and temperature dependencies. Thereafter, angle dependent measurements of magnon transistor devices prepared with modulators made with non-, moderate- and high-SHE efficiency were evinced (c.f. Chap. 5.1.1). Here we demonstrated the impact of applying a charge current to the modulator. Furthermore, a model describing the superimposed influence of thermal and electrical effects induced by the modulator was used based on Ref. [17]. An in detail study of the influence of the modulator current was achieved by conducting modulator current dependent magnon transport measurements (c.f. Chap. 5.2). A discussion of the data obtained for the electrical contribution (c.f. Chap. 5.2.1) has shown that for low modulator current bias the magnon transport can be described by the aforementioned model very well. For the Pt and PtAu devices, however, we observed similar nonlinear features as in Refs. [18] and [106] for large modulator current bias, indicating (at least the onset) of the damping compensation, as proposed in Ref. [18]. These effects were neither observed for the SHE-inefficient Ru and Ti/Al devices, nor for the moderately efficient Ir device. This indicates that the nonlinearities cannot be caused by thermal effects, contrary to the predicition made in Ref. [106]. Furthermore, the model put forward in Ref. [34] based on Ref. [109], which accounts for the damping compensation, fitted our data for the Pt modulator device very well. In the case of the Ir and Ru devices, we observed a rapid decrease of the signal for large modulator current bias. The seemingly equal effects were appointed to different causes: in the case of Ru we proposed the behavior to be caused by electrical leakage currents in the YIG film, whereas in the case of Ir we proposed a magnetic phase transition of the YIG film underneath the modulator, both caused by extensive heating. Our predictions were shown to be valid by considering the corresponding thermal contribution of the magnon transport (c.f. Chap. 5.2.2). By comparing the electrical and thermal signal contributions we came to the conclusion that the electrical signal contribution might be considered as a measure of the system's entropy, whereas the thermal contribution might be seen as a measure of the system's heat capacity, supporting the considerations made in Ref. [34]: the magnetic phase transition of the Ir device demonstrated

a specific behavior in the thermal contribution, which was replicated to some extent by the Pt and PtAu devices, exactly were the onset of the damping compensation is observed in the electrical contribution. The damping compensation transition is expected to represent a phase transition within the magnon system [107, 109], which we verify by the characteristic features in the measurements of the thermal contribution. A semiconductor model applied to YIG has been put forward to describe the possibility of emerging electrical leakage currents (c.f. Chap. 5.2.3). The model fitted our data very well and the extracted bandgap value was in reasonable agreement with the findings from Ref. [117] and furthermore yielded a value for the heating coefficient of the modulator very close to the expected value. Finally, we exploited the different symmetries of electrical and thermal magnon excitation effects and calculated the modulation strengths and efficiencies of the electrical and thermal modulation separately for the electrical signal contribution (c.f. Chap. 5.2.4). As expected, the SHE-inefficient Ti/Al and Ru modulators did not show a finite electrical modulation efficiency, whereas Ir, PtAu and Pt resembled the behavior foreseen by the SMR measurements from Chap. 4.5. Furthermore, all devices were shown to exhibit a finite thermal modulation efficiency due to their finite electrical resistance.

6 Summary and Outlook

In this work, we investigated the magnon transport NM/YIG bilayers patterned as magnetic transistor devices [22, 23]. The studied YIG samples were ultrathin ($10-20\mathrm{nm}$) films grown by PLD at the Walther-Meißner-Institut. The injection and detection of the spin waves was achieved by utilizing the spin Hall and inverse spin Hall effects (SHE and ISHE) in Pt electrodes, which we refer to as injector and detector. The injector and detector electrodes were patterned as electrically isolated nanowires, allowing to achieve high current densities by applying comparably low current intensities at the injector electrode. Due to the SHE, a charge current applied to the injector gives rise to a spin current in the injector, which subsequently induces an electron spin accumulation at the injector Pt/YIG interface. Spin flip scattering events occurring at this interface generate or annihilate magnons in the YIG film, thus giving rise to a non-equlibrium magnon accumulation. Another mechanism for generating non-equilibrium magnon accumulations is the spin Seebeck effect (SSE), which is achieved by a temperature gradient of the electron and magnon bath. The generated non-equilibrium magnon accumulations diffuse in the YIG layer, induce an electron spin accumulation at the detector Pt/YIG interface and are measured via the ISHE. Due to the different symmetries of the SHE (electrical) and SSE (thermal), we are able to distinguish between the electrical and thermal induced magnons, which we refer to as the electrical and thermal magnon transport contribution. The main drawback of this kind of transport is reflected in the fact that the number of magnons in a magnetically ordered insulator is not conserved. This work was aimed at bypassing this shortcoming by introducing a third electrode- the modulator, which fulfills a function similar to a gate electrode in a conventional semiconductor transistor, that is to modulate the magnon conductivity of the YIG layer [17, 18, 106]. The deployed measurement techniques allowed to measure the change in the magnon conductivity, without "picking-up"the magnons stemming from the modulator. Depending on the choice of the modulator material, one can tune its electrical contribution and therefore investigate the underlying physics in more detail. In the following Sections we are going to present a summary of the main results of this thesis and offer some proposals for future experiments on the topics covered in this work.

6.1 Summary

In Chapter 4, we characterized two $\mathrm{Pt_{1-x}Au_x}$ alloys with $x = 0.1, 0.25$ patterned on two YIG films as series of devices of different thickness together with Pt reference devices. Recent publications [78, 79] suggested that PtAu alloys with small concentrations of Au could exceed pure Pt in terms of SHE efficiency, therefore acting as an even better material for generation of pure spin currents. In order to prove these observations, we conducted angle dependent spin Hall magnetoresistance (SMR) measurements for a variety of different temperatures and field strengths. Furthermore, we repeated the measurements in three mutually orthogonal planes to gather additional informations about the alloys. The out-of-plane measurements yielded a very interesting result: we arguably observed additional magnetoresistance (MR) effects which exhibit a strong temperature dependence. These findings were attributed to a combination of ordinary MR, magnetic proximity effect-induced anisotropic MR and to simple sample misalignment with the external magnetic field. Con-

trary to the theoretical predictions for the SMR [50], we observed a pronounced magnetic field dependence which can only be rationalized by imperfect NM/YIG interfaces giving rise to so-called pinning effects. The quality grade of the interface was also reflected in the resistivites of the metals, which were one to two orders of magnitude larger when compared to values obtained in previous studies [75, 78, 79]. Nevertheless, our measurements suggest that the PtAu alloys are not comparable with Pt in terms of SHE efficiency, taking into account not only the spin Hall angle θ_{SH}, but rather a combination with the spin diffusion length λ_{s} and the spin mixing conductance $g^{\uparrow\downarrow}$. Furthermore, the SHE efficiency was shown to decrease with increasing concentration of the Au component. We were still able to take advantage of this result by fabricating $\mathrm{Pt}_{0.75}\mathrm{Au}_{0.25}$, together with Ti/Al, Ru, Ir and Pt modulators for our magnon transport experiments. The SHE efficiency of these materials were as well characterized by SMR measurements, which have shown to be a very powerful probe for characterizing SHE efficiency of a metal for a particular NM/YIG interface.

In Chapter 5, we first discussed angle dependent magnon transport measurements of a two-electrode device in order to highlight the general features of magnon transport. Subsequently, we discussed measurements of magnon transistor devices with different modulator electrodes. First of all, we conducted angle dependent measurements, allowing for a qualitative characterization of the influence of the particular electrode material. A model describing the magnon conductivity in terms of electrically induced effects odd in the modulator current and thermally induced effects even in the modulator current was used [17], describing our data very well. Employing different modulator materials allowed us to gradually reduce the SHE contribution of the modulator electrode. Opting for a quantitative decription, we employed current dependent measurements. Here, the effect of the SHE modulation at the modulator electrode became perceptible. Considering the electrical signal contribution, materials showing vanishing (Ti/Al, Ru) or low SHE efficiency (Ir) were well described by the aforementioned model, even for large modulator current bias. On the other hand, the moderately and highly SHE effective PtAu and Pt modulators, exhibited a pronounced deviation from this model for large modulator current bias. These findings corroborate the observations from Ref. [18] and the theoretical prediction made in Ref. [109] about a possible SHE induced magnetic damping compensation. Contrary to the assumptions from Ref. [106], arguing that the observed nonlinearity is a consequence of heating (SSE) effects, we clearly demonstrated that the nonlinear behavior cannot be invoked by exclusive thermal excitation at the modulator. Furthermore, for the Ir device, the achieved current densities were large enough to reach temperatures above the ordering temperature of YIG and thus observed a magnetic phase transition. The corresponding measurements of the thermal contribution of the magnon transport verified this observation, showing characteristic lambda-shaped peaks for current densities at which the signal rapidly decreased in the electrical signal contribution. This observation corroborates the premise made in Ref. [34], where the electrical signal contribution is described as a possible measure of the system's entropy, whereas the thermal signal contribution is regarded as a possible measure of the system's heat capacity. Furthermore, we observe a similar lambda-shaped peak in the thermal contributions of the PtAu and Pt devices, corresponding to the damping compensation regime in the electrical contribution. This suggests that a damping compensation is

indeed achieved in the YIG films with PtAu and Pt devices. The damping compensation regime [18] is not to be mistaken with a ferromagnet to paramagnet phase transition which occurs at T_c. In the case of the Ru and Pt devices we arguably observed effects caused by electrical leakage currents. This was tested by introducing a semiconductor model for the YIG films, which was shown to describe our data with extraordinary agreement, therefore confirming the assumption of leakage currents. Comparing the obtained bandgap value with Ref. [117] yielded a reasonable result. Finally, the electrical and thermal modulation efficiencies of the different modulator materials were disentangled. This was discussed for the electrical contribution, with the results being in very good agreement with the predictions made by the SMR characterization, indicating once more the versatility of the SMR measurements.

6.2 Outlook

We now want to offer a short outlook to possible future investigations of the topics investigated in this work. Regarding the characterization of the PtAu alloys and alloys in general, it is important to point out that the co-sputtering technique is not the best suited technique for producing alloys with a precisely set stoichiometry, since it is difficult to precisely control the ratio of the components. Therefore we suggest the usage of pre-fabricated composite targets with the right stoichiometry. Taking into account that both Pt and Au are precious metals, this demand is not inexpensive. Utilizing a less invasive deposition technique than sputtering could as well be beneficial in terms of the interface quality. Finally, producing in situ samples would exclude the possibility of interface contaminations. The primary goal we set out was to increase SHE efficiency without increasing Joule heating due to increased resistivity of the material. Another approach would be to either utilize NM multilayers to enhance SHE efficiency [127] or utilize magnetically ordered metals and their associated anomalous spin Hall effect. Another important aspect is a better understanding of the interface and defects at the interface influencing the spin mixing conductance and thus enhance spin current injection into the MOI.

For the magnon transport measurements it is essential to verify the results regarding the phase transitions. This could be achieved by measuring the magnon transport while intentionally inducing a magnetic ordering transition by increasing the base temperature. However, it would as well be necessary to measure the heat capacity directly and to compare the results to the thermal magnon transport data. On the other hand, utilizing the 3ω method [128, 129, 130] for thermal conductivity measurements would be another option. Similar to the previously discussed SMR measurements, an improved interface quality would as well be beneficial for both the magnon modulation and transport [115]. Possible scenarios include less invasive deposition techniques and the usage of interlayers between the NM and the YIG film [131, 132, 133, 134]. At present the concept of manipulating magnon transport via an additional modulator contact has only been applied to YIG, because it exhibits the lowest magnon decay rate and thus allows to reach the point of damping compensation. It would be highly desirable to check if the effects are indeed universal and can be also observed in different MOIs, for example in antiferromagnetic insulators where current experiments indicate also long magnon lifetimes. Last but not least, it would

be helpful to combine spatially resolved probing techniques for the detection of magnetic stray fields like nitrogen vacancies in diamond with all-electrical measurement techniques to gain a deeper insight into the damping-compensation regime.

A Appendix: PLD YIG Films

In this Section we summarize the PLD YIG samples grown at the Walther-Meißner-Institut with the corresponding growth parameters.

ID	$T_{\mathrm{sample}}(^{\circ}\mathrm{C})$	number of laser pulses	$U(\mathrm{kV})$	$E(\mathrm{mJ})$	$t_{\mathrm{sample}}(\mathrm{nm})$	modulator material
YIG289	573	5500	20.98	58.74	9.93	Ti/Al, Pt
YIG301	565	6500	20.79	57.55	9.66	Ti/Al, Pt
YIG302	567	9000	20.71	56.29	20.73	PtAu, Pt
YIG305	528	9000	20.74	55.4	13.78	Ru, Pt
YIG306	520	10000	20.88	57.21	22.21	Ru, Pt
YIG309	558	8500	20.67	51.38	19.52	Ir, Pt

Tab. A.1: List of PLD-grown YIG samples used in this work with indicated sample growth temperature T_{sample}, number of laser pulses during the growth process, voltage bias U for the reflection high-energy electron diffraction (RHEED) in situ analysis method, the laser-beam energy E, sample thickness t_{sample} and subsequently deposited modulator materials. The laser is a pulsed UV-excimer laser (KrF, $248\,\mathrm{nm}$) and the energy density per pulse was $2\,\mathrm{J cm^{-2}}$. All samples were grown on GGG(100) substrates in an Oxygen atmosphere at a surrounding temperature of $450\,^{\circ}\mathrm{C}$ and a pressure of $25\,\mu\mathrm{bar}$.

References

[1] P. Ehrenfest. Ersetzung der Hypothese vom unmechanischen Zwang durch eine Forderung bezüglich des inneren Verhaltens jedes einzelnen Elektrons. *Die Naturwissenschaften* **13**, 953–954 (1925). URL.

[2] W. Pauli. Über den Zusammenhang des Abschlusses der Elektronengruppen im Atom mit der Komplexstruktur der Spektren. *Zeitschrift für Physik* **31**, 765–783 (1925). URL.

[3] A. Pais. George Uhlenbeck and the Discovery of Electron Spin. *Physics Today* **42**, 34–40 (1989). URL.

[4] 1956 Nobel Prize in Physics. *Physics Today* **10**, 16–17 (1957). URL.

[5] G. E. Moore. Progress in digital integrated electronics [Technical literaiture, Copyright 1975 IEEE. Reprinted, with permission. Technical Digest. International Electron Devices Meeting, IEEE, 1975, pp. 11-13.]. *IEEE Solid-State Circuits Society Newsletter* **11**, 36–37 (2006). URL.

[6] R. Dennard, F. Gaensslen, H.-N. Yu, V. Rideout, E. Bassous & A. LeBlanc. Design of ion-implanted MOSFET's with very small physical dimensions. *IEEE Journal of Solid-State Circuits* **9**, 256–268 (1974). URL.

[7] L. Johnsson & G. Netzer. The impact of Moore's Law and loss of Dennard scaling: Are DSP SoCs an energy efficient alternative to x86 SoCs? *Journal of Physics: Conference Series* **762**, 012022 (2016). URL.

[8] M. M. Waldrop. The chips are down for Moore's law. *Nature* **530**, 144–147 (2016). URL.

[9] X. Lin, W. Yang, K. L. Wang & W. Zhao. Two-dimensional spintronics for low-power electronics. *Nature Electronics* **2**, 274–283 (2019). URL.

[10] F. Pulizzi. The rise of semiconductor spintronics. *Nature Physics* **4**, S20–S20 (2008). URL.

[11] M. N. Baibich, J. M. Broto, A. Fert, F. N. V. Dau, F. Petroff, P. Etienne, G. Creuzet, A. Friederich & J. Chazelas. Giant Magnetoresistance of (001)Fe/(001)Cr Magnetic Superlattices. *Physical Review Letters* **61**, 2472–2475 (1988). URL.

[12] G. Binasch, P. Grünberg, F. Saurenbach & W. Zinn. Enhanced magnetoresistance in layered magnetic structures with antiferromagnetic interlayer exchange. *Physical Review B* **39**, 4828–4830 (1989). URL.

[13] M. Althammer. Pure spin currents in magnetically ordered insulator/normal metal heterostructures. *Journal of Physics D: Applied Physics* **51**, 313001 (2018). URL.

[14] S. Murakami. Dissipationless Quantum Spin Current at Room Temperature. *Science* **301**, 1348–1351 (2003). URL.

[15] S. O. Demokritov, V. E. Demidov, O. Dzyapko, G. A. Melkov, A. A. Serga, B. Hillebrands & A. N. Slavin. Bose–Einstein condensation of quasi-equilibrium magnons at room temperature under pumping. *Nature* **443**, 430–433 (2006). URL.

[16] B. Flebus, S. Bender, Y. Tserkovnyak & R. Duine. Two-Fluid Theory for Spin Superfluidity in Magnetic Insulators. *Physical Review Letters* **116** (2016). URL.

[17] L. Cornelissen, J. Liu, B. van Wees & R. Duine. Spin-Current-Controlled Modulation of the Magnon Spin Conductance in a Three-Terminal Magnon Transistor. *Physical Review Letters* **120** (2018). URL.

[18] T. Wimmer, M. Althammer, L. Liensberger, N. Vlietstra, S. Geprägs, M. Weiler, R. Gross & H. Huebl. Spin Transport in a Magnetic Insulator with Zero Effective Damping. *Physical Review Letters* **123** (2019). URL.

[19] M. I. Dyakonov & V. I. Perel. Possibility of Orienting Electron Spins with Current. *Journal of Experimental and Theoretical Physics Letters* **13** (1971).

[20] J. E. Hirsch. Spin Hall Effect. *Physical Review Letters* **83**, 1834–1837 (1999). URL.

[21] Y. K. Kato, R. C. Myers, A. C. Gossard & D. D. Awschalom. Observation of the Spin Hall Effect in Semiconductors. *Science* **306**, 1910–1913 (2004). URL.

[22] L. J. Cornelissen, J. Liu, R. A. Duine, J. B. Youssef & B. J. van Wees. Long-distance transport of magnon spin information in a magnetic insulator at room temperature. *Nature Physics* **11**, 1022–1026 (2015). URL.

[23] S. T. B. Goennenwein, R. Schlitz, M. Pernpeintner, K. Ganzhorn, M. Althammer, R. Gross & H. Huebl. Non-local magnetoresistance in YIG/Pt nanostructures. *Applied Physics Letters* **107**, 172405 (2015). URL.

[24] E. Saitoh, M. Ueda, H. Miyajima & G. Tatara. Conversion of spin current into charge current at room temperature: Inverse spin-Hall effect. *Applied Physics Letters* **88**, 182509 (2006). URL.

[25] J. Xiao, G. E. W. Bauer, K.-c. Uchida, E. Saitoh & S. Maekawa. Theory of magnon-driven spin Seebeck effect. *Physical Review B* **81**, 214418 (2010). URL.

[26] M. Schreier, A. Kamra, M. Weiler, J. Xiao, G. E. W. Bauer, R. Gross & S. T. B. Goennenwein. Magnon, phonon, and electron temperature profiles and the spin Seebeck effect in magnetic insulator/normal metal hybrid structures. *Physical Review B* **88**, 094410 (2013). URL.

[27] N. F. Mott. The electrical conductivity of transition metals. *Proceedings of the Royal Society of London. Series A - Mathematical and Physical Sciences* **153**, 699–717 (1936). URL.

[28] F. D. Czeschka. *Spin Currents in Metallic Nanostructures*. Ph.D. thesis, Technische Universität München (2011).

[29] T. Wimmer. *Spin Transport in Magnetic Nanostructures*. Master's thesis, Technische Universität München (2016).

[30] J. Shi, P. Zhang, D. Xiao & Q. Niu. Proper Definition of Spin Current in Spin-Orbit Coupled Systems. *Physical Review Letters* **96** (2006). URL.

[31] P.-Q. Jin, Y.-Q. Li & F.-C. Zhang. SU(2) × U(1) unified theory for charge, orbit and spin currents. *Journal of Physics A: Mathematical and General* **39**, 7115–7123 (2006). URL.

[32] A. Vernes, B. L. Györffy & P. Weinberger. Spin currents, spin-transfer torque, and spin-Hall effects in relativistic quantum mechanics. *Physical Review B* **76** (2007). URL.

[33] S. Lowitzer, D. Ködderitzsch & H. Ebert. Spin projection and spin current density within relativistic electronic-transport calculations. *Physical Review B* **82** (2010). URL.

[34] T. Wimmer. *Controlling Magnonic Spin Currents in Magnetic Insulators*. Phd thesis, Technische Universität München (2020).

[35] J. Smit. The spontaneous hall effect in ferromagnetics II. *Physica* **24**, 39–51 (1958). URL.

[36] M. Julliere. Tunneling between ferromagnetic films. *Physics Letters A* **54**, 225–226 (1975). URL.

[37] L. Berger. Side-Jump Mechanism for the Hall Effect of Ferromagnets. *Physical Review B* **2**, 4559–4566 (1970). URL.

[38] M. V. Berry. Quantal phase factors accompanying adiabatic changes. *Proceedings of the Royal Society of London. A. Mathematical and Physical Sciences* **392**, 45–57 (1984). URL.

[39] D. Xiao, M.-C. Chang & Q. Niu. Berry phase effects on electronic properties. *Reviews of Modern Physics* **82**, 1959–2007 (2010). URL.

[40] P. Jacquod, R. S. Whitney, J. Meair & M. Büttiker. Onsager relations in coupled electric, thermoelectric, and spin transport: The tenfold way. *Physical Review B* **86** (2012). URL.

[41] M. Schreier, G. E. W. Bauer, V. I. Vasyuchka, J. Flipse, K. ichi Uchida, J. Lotze, V. Lauer, A. V. Chumak, A. A. Serga, S. Daimon, T. Kikkawa, E. Saitoh, B. J. van Wees, B. Hillebrands, R. Gross & S. T. B. Goennenwein. Sign of inverse spin Hall voltages generated by ferromagnetic resonance and temperature gradients in yttrium iron garnet platinum bilayers. *Journal of Physics D: Applied Physics* **48**, 025001 (2014). URL.

[42] C. Chen, D. Tian, H. Zhou, D. Hou & X. Jin. Generation and Detection of Pure Spin Current in an H -Shaped Structure of a Single Metal. *Physical Review Letters* **122** (2019). URL.

[43] S. O. Valenzuela & M. Tinkham. Direct electronic measurement of the spin Hall effect. *Nature* **442**, 176–179 (2006). URL.

[44] L. Liu, C.-F. Pai, Y. Li, H. W. Tseng, D. C. Ralph & R. A. Buhrman. Spin-Torque Switching with the Giant Spin Hall Effect of Tantalum. *Science* **336**, 555–558 (2012). URL.

[45] K. Uchida, S. Takahashi, K. Harii, J. Ieda, W. Koshibae, K. Ando, S. Maekawa & E. Saitoh. Observation of the spin Seebeck effect. *Nature* **455**, 778–781 (2008). URL.

[46] W. T. L. Kelvin. XIX. On the electro-dynamic qualities of metals:—Effects of magnetization on the electric conductivity of nickel and of iron. *Proceedings of the Royal Society of London* **8**, 546–550 (1857). URL.

[47] T. McGuire & R. Potter. Anisotropic magnetoresistance in ferromagnetic 3d alloys. *IEEE Transactions on Magnetics* **11**, 1018–1038 (1975). URL.

[48] H. Nakayama, M. Althammer, Y.-T. Chen, K. Uchida, Y. Kajiwara, D. Kikuchi, T. Ohtani, S. Geprägs, M. Opel, S. Takahashi, R. Gross, G. E. W. Bauer, S. T. B. Goennenwein & E. Saitoh. Spin Hall Magnetoresistance Induced by a Nonequilibrium Proximity Effect. *Physical Review Letters* **110**, 206601 (2013). URL.

[49] F. P. Witek. *Spin Hall Magnetoresistance Noise*. Master's thesis, Technische Universität München (2013).

[50] Y.-T. Chen, S. Takahashi, H. Nakayama, M. Althammer, S. T. B. Goennenwein, E. Saitoh & G. E. W. Bauer. Theory of spin Hall magnetoresistance. *Physical Review B* **87** (2013). URL.

[51] A. Manchon, J. Železný, I. Miron, T. Jungwirth, J. Sinova, A. Thiaville, K. Garello & P. Gambardella. Current-induced spin-orbit torques in ferromagnetic and antiferromagnetic systems. *Reviews of Modern Physics* **91** (2019). URL.

[52] M. Johnson & R. H. Silsbee. Interfacial charge-spin coupling: Injection and detection of spin magnetization in metals. *Physical Review Letters* **55**, 1790–1793 (1985). URL.

[53] M. Johnson & R. H. Silsbee. Coupling of electronic charge and spin at a ferromagnetic-paramagnetic metal interface. *Physical Review B* **37**, 5312–5325 (1988). URL.

[54] A. Brataas, Y. V. Nazarov & G. E. W. Bauer. Finite-Element Theory of Transport in Ferromagnet–Normal Metal Systems. *Physical Review Letters* **84**, 2481–2484 (2000). URL.

[55] M. Weiler, M. Althammer, M. Schreier, J. Lotze, M. Pernpeintner, S. Meyer, H. Huebl, R. Gross, A. Kamra, J. Xiao, Y.-T. Chen, H. Jiao, G. E. W. Bauer & S. T. B. Goennenwein. Experimental Test of the Spin Mixing Interface Conductivity Concept. *Physical Review Letters* **111** (2013). URL.

[56] S. S.-L. Zhang & S. Zhang. Magnon Mediated Electric Current Drag Across a Ferromagnetic Insulator Layer. *Physical Review Letters* **109**, 096603 (2012). URL.

[57] S. S.-L. Zhang & S. Zhang. Spin convertance at magnetic interfaces. *Physical Review B* **86**, 214424 (2012). URL.

[58] S. A. Bender & Y. Tserkovnyak. Interfacial spin and heat transfer between metals and magnetic insulators. *Physical Review B* **91**, 140402 (2015). URL.

[59] L. J. Cornelissen, K. J. H. Peters, G. E. W. Bauer, R. A. Duine & B. J. van Wees. Magnon spin transport driven by the magnon chemical potential in a magnetic insulator. *Physical Review B* **94** (2016). URL.

[60] Y. Tserkovnyak, A. Brataas & G. E. W. Bauer. Spin pumping and magnetization dynamics in metallic multilayers. *Physical Review B* **66** (2002). URL.

[61] M. V. Costache, M. Sladkov, S. M. Watts, C. H. van der Wal & B. J. van Wees. Electrical Detection of Spin Pumping due to the Precessing Magnetization of a Single Ferromagnet. *Physical Review Letters* **97** (2006). URL.

[62] K. Ando, S. Takahashi, J. Ieda, Y. Kajiwara, H. Nakayama, T. Yoshino, K. Harii, Y. Fujikawa, M. Matsuo, S. Maekawa & E. Saitoh. Inverse spin-Hall effect induced by spin pumping in metallic system. *Journal of Applied Physics* **109**, 103913 (2011). URL.

[63] K. Uchida, J. Xiao, H. Adachi, J. Ohe, S. Takahashi, J. Ieda, T. Ota, Y. Kajiwara, H. Umezawa, H. Kawai, G. E. W. Bauer, S. Maekawa & E. Saitoh. Spin Seebeck insulator. *Nature Materials* **9**, 894–897 (2010). URL.

[64] V. Cherepanov, I. Kolokolov & V. L'vov. The saga of YIG: Spectra, thermodynamics, interaction and relaxation of magnons in a complex magnet. *Physics Reports* **229**, 81–144 (1993). URL.

[65] C. Dubs, A. Chumak & B. Hillebrands. Functional layers of nanometer-thick YIG films and microstructured surfaces for spintronic application. `https://www.physik.uni-kl.de/hillebrands/research/dfg-nanoyig/`. DFG-Normalverfahren (2015).

[66] M. L. Néel. Propriétés magnétiques des ferrites ferrimagnétisme et antiferromagnétisme. *Annales de Physique* **12**, 137–198 (1948). URL.

[67] M. L. Néel. Magnetism and the Local Molecular Field. `https://www.nobelprize.org/uploads/2018/06/neel-lecture.pdf`. Nobel Lecture (1970).

[68] N. Miura, I. Oguro & S. Chikazumi. Computer Simulation of Temperature and Field Dependences of Sublattice Magnetizations and Spin-Flip Transition in Gallium-Substituted Yttrium Iron Garnet. *Journal of the Physical Society of Japan* **45**, 1534–1541 (1978). URL.

[69] A. Prabhakar & D. D. Stancil. *Spin Waves, Theory and Applications* (Springer US, 2009).

[70] S. O. Valenzuela & M. Tinkham. Electrical detection of spin currents: The spin-current induced Hall effect (invited). *Journal of Applied Physics* **101**, 09B103 (2007). URL.

[71] C. Du, H. Wang, F. Yang & P. C. Hammel. Systematic variation of spin-orbit coupling withd-orbital filling: Large inverse spin Hall effect in3dtransition metals. *Physical Review B* **90** (2014). URL.

[72] K. Eid, R. Fonck, M. A. Darwish, W. P. Pratt & J. Bass. Current-perpendicular-to-plane-magnetoresistance properties of Ru and Co/Ru interfaces. *Journal of Applied Physics* **91**, 8102 (2002). URL.

[73] J. E. Gómez, B. Z. Tedlla, N. R. Álvarez, G. Alejandro, E. Goovaerts & A. Butera. Spin transport parameters inNi80Fe20/RuandNi80Fe20/Tabilayers. *Physical Review B* **90** (2014). URL.

[74] T. Fache, J. C. Rojas-Sanchez, L. Badie, S. Mangin & S. Petit-Watelot. Determination of spin Hall angle, spin mixing conductance, and spin diffusion length in CoFeB/Ir for spin-orbitronic devices. *Physical Review B* **102** (2020). URL.

[75] M. Althammer, S. Meyer, H. Nakayama, M. Schreier, S. Altmannshofer, M. Weiler, H. Huebl, S. Geprägs, M. Opel, R. Gross, D. Meier, C. Klewe, T. Kuschel, J.-M. Schmalhorst, G. Reiss, L. Shen, A. Gupta, Y.-T. Chen, G. E. W. Bauer, E. Saitoh & S. T. B. Goennenwein. Quantitative study of the spin Hall magnetoresistance in ferromagnetic insulator/normal metal hybrids. *Physical Review B* **87** (2013). URL.

[76] X. Wang, C. O. Pauyac & A. Manchon. Spin-orbit-coupled transport and spin torque in a ferromagnetic heterostructure. *Physical Review B* **89** (2014). URL.

[77] J. Gückelhorn, T. Wimmer, S. Geprägs, H. Huebl, R. Gross & M. Althammer. Quantitative comparison of magnon transport experiments in three-terminal YIG/Pt nanostructures acquired via dc and ac detection techniques. *Applied Physics Letters* **117**, 182401 (2020). URL.

[78] Y. Xu, Y. Yang, H. Xie & Y. Wu. Spin Hall magnetoresistance sensor using AuxPt1-x as the spin-orbit torque biasing layer. *Applied Physics Letters* **115**, 182406 (2019). URL.

[79] L. Zhu, D. C. Ralph & R. A. Buhrman. Highly Efficient Spin-Current Generation by the Spin Hall Effect in Au1-xPtx. *Physical Review Applied* **10** (2018). URL.

[80] S. Matsura. *Investigation of Magnetoresistance Tuned by Interface States of YIG/Pt Heterostructures*. Master's thesis, Technische Universität München (2017).

[81] B. Coester. *Analysis of pure spin current transport in yttrium iron garnet | normal metal heterostructures*. Master's thesis, Technische Universität München (2018).

[82] J. Schirk. *Spin Hall magnetoresistance in yttrium iron garnet | tungsten heterostructures*. Bachelor's thesis, Technische Universität München (2019).

[83] R. Markiewicz & L. Harris. Localization in ultrathin metal films. *Surface Science* **113**, 531–536 (1982). URL.

[84] H. Ebert, A. Vernes & J. Banhart. Magnetoresistance, Anisotropic. In *Encyclopedia of Materials: Science and Technology* 5079–5083 (Elsevier, 2001).

[85] Y. M. Lu, J. W. Cai, S. Y. Huang, D. Qu, B. F. Miao & C. L. Chien. Hybrid magnetoresistance in the proximity of a ferromagnet. *Physical Review B* **87** (2013). URL.

[86] X. Zhou, L. Ma, Z. Shi, W. J. Fan, J.-G. Zheng, R. F. L. Evans & S. M. Zhou. Magnetotransport in metal/insulating-ferromagnet heterostructures: Spin Hall magnetoresistance or magnetic proximity effect. *Physical Review B* **92** (2015). URL.

[87] S. Geprägs, S. Meyer, S. Altmannshofer, M. Opel, F. Wilhelm, A. Rogalev, R. Gross & S. T. B. Goennenwein. Investigation of induced Pt magnetic polarization in Pt/Y3Fe5O12 bilayers. *Applied Physics Letters* **101**, 262407 (2012). URL.

[88] S. Vélez, V. N. Golovach, A. Bedoya-Pinto, M. Isasa, E. Sagasta, M. Abadia, C. Rogero, L. E. Hueso, F. S. Bergeret & F. Casanova. Hanle Magnetoresistance in Thin Metal Films with Strong Spin-Orbit Coupling. *Physical Review Letters* **116** (2016). URL.

[89] S. Meyer, M. Althammer, S. Geprägs, M. Opel, R. Gross & S. T. B. Goennenwein. Temperature dependent spin transport properties of platinum inferred from spin Hall magnetoresistance measurements. *Applied Physics Letters* **104**, 242411 (2014). URL.

[90] M. Isasa, E. Villamor, L. E. Hueso, M. Gradhand & F. Casanova. Temperature dependence of spin diffusion length and spin Hall angle in Au and Pt. *Physical Review B* **91** (2015). URL.

[91] S. R. Marmion, M. Ali, M. McLaren, D. A. Williams & B. J. Hickey. Temperature dependence of spin Hall magnetoresistance in thin YIG/Pt films. *Physical Review B* **89** (2014). URL.

[92] S. Meyer. *Magneto-thermogalvanische Experimente an (Ga,Mn)As Dünnfilmen*. Diploma thesis, Ludwig-Maximilian-Universität München (2012).

[93] X. guang Wang, Z. wei Zhou, Y. zhuang Nie, Q. lin Xia & G. hua Guo. Self-consistent study of local and nonlocal magnetoresistance in a YIG/Pt bilayer. *Physical Review B* **97** (2018). URL.

[94] R. J. Elliott. Theory of the Effect of Spin-Orbit Coupling on Magnetic Resonance in Some Semiconductors. *Physical Review* **96**, 266–279 (1954). URL.

[95] Y. Yafet. Factors and Spin-Lattice relaxation of Conduction Electrons. *Solid State Physics* **14**, 1–98 (1963). URL.

[96] C. James. The residual resistance of metals. *Physics Education* **2**, 315–316 (1967). URL.

[97] J. Shan, A. V. Singh, L. Liang, L. J. Cornelissen, Z. Galazka, A. Gupta, B. J. van Wees & T. Kuschel. Enhanced magnon spin transport in NiFe2O4 thin films on a lattice-matched substrate. *Applied Physics Letters* **113**, 162403 (2018). URL.

[98] J. Cramer, F. Fuhrmann, U. Ritzmann, V. Gall, T. Niizeki, R. Ramos, Z. Qiu, D. Hou, T. Kikkawa, J. Sinova, U. Nowak, E. Saitoh & M. Kläui. Magnon detection using a ferroic collinear multilayer spin valve. *Nature Communications* **9** (2018). URL.

[99] T. Wimmer, A. Kamra, J. Gückelhorn, M. Opel, S. Geprägs, R. Gross, H. Huebl & M. Althammer. Observation of Antiferromagnetic Magnon Pseudospin Dynamics and the Hanle Effect. *Physical Review Letters* **125** (2020). URL.

[100] A. V. Chumak, A. A. Serga & B. Hillebrands. Magnon transistor for all-magnon data processing. *Nature Communications* **5** (2014). URL.

[101] J. Cramer, F. Fuhrmann, U. Ritzmann, V. Gall, T. Niizeki, R. Ramos, Z. Qiu, D. Hou, T. Kikkawa, J. Sinova, U. Nowak, E. Saitoh & M. Kläui. Magnon detection using a ferroic collinear multilayer spin valve. *Nature Communications* **9** (2018). URL.

[102] A. Hamadeh, O. d'Allivy Kelly, C. Hahn, H. Meley, R. Bernard, A. Molpeceres, V. Naletov, M. Viret, A. Anane, V. Cros, S. Demokritov, J. Prieto, M. Muñoz, G. de Loubens & O. Klein. Full Control of the Spin-Wave Damping in a Magnetic Insulator Using Spin-Orbit Torque. *Physical Review Letters* **113** (2014). URL.

[103] M. Collet, X. de Milly, O. d'Allivy Kelly, V. V. Naletov, R. Bernard, P. Bortolotti, J. B. Youssef, V. E. Demidov, S. O. Demokritov, J. L. Prieto, M. Muñoz, V. Cros, A. Anane, G. de Loubens & O. Klein. Generation of coherent spin-wave modes in yttrium iron garnet microdiscs by spin–orbit torque. *Nature Communications* **7** (2016). URL.

[104] M. Evelt, V. E. Demidov, V. Bessonov, S. O. Demokritov, J. L. Prieto, M. Muñoz, J. B. Youssef, V. V. Naletov, G. de Loubens, O. Klein, M. Collet, K. Garcia-Hernandez, P. Bortolotti, V. Cros & A. Anane. High-efficiency control of spin-wave propagation in ultra-thin yttrium iron garnet by the spin-orbit torque. *Applied Physics Letters* **108**, 172406 (2016). URL.

[105] M. Evelt, L. Soumah, A. Rinkevich, S. Demokritov, A. Anane, V. Cros, J. B. Youssef, G. de Loubens, O. Klein, P. Bortolotti & V. Demidov. Emission of Coherent Propagating Magnons by Insulator-Based Spin-Orbit-Torque Oscillators. *Physical Review Applied* **10** (2018). URL.

[106] J. Liu, X.-Y. Wei, G. E. W. Bauer, J. Ben Youssef & B. J. van Wees. Electrically induced strong modulation of magnons transport in ultrathin magnetic insulator films. *arXiv e-prints* arXiv:2011.07800 (2020), 2011.07800.

[107] S. A. Bender, R. A. Duine, A. Brataas & Y. Tserkovnyak. Dynamic phase diagram of dc-pumped magnon condensates. *Physical Review B* **90** (2014). URL.

[108] V. E. Demidov, S. Urazhdin, B. Divinskiy, V. D. Bessonov, A. B. Rinkevich, V. V. Ustinov & S. O. Demokritov. Chemical potential of quasi-equilibrium magnon gas driven by pure spin current. *Nature Communications* **8** (2017). URL.

[109] S. Takei. Spin transport in an electrically driven magnon gas near Bose-Einstein condensation: Hartree-Fock-Keldysh theory. *Physical Review B* **100** (2019). URL.

[110] M. Evers & U. Nowak. Transport properties of spin superfluids: Comparing easy-plane ferromagnets and antiferromagnets. *Physical Review B* **101** (2020). URL.

[111] S. Hoffman, K. Sato & Y. Tserkovnyak. Landau-Lifshitz theory of the longitudinal spin Seebeck effect. *Physical Review B* **88** (2013). URL.

[112] L. J. Cornelissen & B. J. van Wees. Magnetic field dependence of the magnon spin diffusion length in the magnetic insulator yttrium iron garnet. *Physical Review B* **93** (2016). URL.

[113] J. Li, Y. Xu, M. Aldosary, C. Tang, Z. Lin, S. Zhang, R. Lake & J. Shi. Observation of magnon-mediated current drag in Pt/yttrium iron garnet/Pt(Ta) trilayers. *Nature Communications* **7** (2016). URL.

[114] J. Shan, L. J. Cornelissen, N. Vlietstra, J. B. Youssef, T. Kuschel, R. A. Duine & B. J. van Wees. Influence of yttrium iron garnet thickness and heater opacity on the nonlocal transport of electrically and thermally excited magnons. *Physical Review B* **94** (2016). URL.

[115] R. Kohno, N. Thiery, K. An, P. Noël, L. Vila, V. V. Naletov, N. Beaulieu, J. Ben Youssef, G. de Loubens & O. Klein. Enhancement of YIG|Pt spin conductance by local Joule annealing. *arXiv e-prints* arXiv:2009.02785 (2020), 2009.02785.

[116] E. E. Anderson. Molecular Field Model and the Magnetization of YIG. *Physical Review* **134**, A1581–A1585 (1964). URL.

[117] N. Thiery, V. V. Naletov, L. Vila, A. Marty, A. Brenac, J.-F. Jacquot, G. de Loubens, M. Viret, A. Anane, V. Cros, J. B. Youssef, N. Beaulieu, V. E. Demidov, B. Divinskiy, S. O. Demokritov & O. Klein. Electrical properties of epitaxial yttrium iron garnet ultrathin films at high temperatures. *Physical Review B* **97** (2018). URL.

[118] V. Cherepanov, I. Kolokolov & V. L'vov. *The Saga of YIG: Spectra, Thermodynamics, Interaction and Relaxation of Magnons in a Complex Magnet*. Physics reports (North-Holland, 1993).

[119] E. Hartmann, L. Kovács & J. Paitz. Electrical conductivity of gadolinium–gallium garnet (GGG) crystals. *Physica Status Solidi (a)* **86**, 401–405 (1984). URL.

[120] P. K. Larsen & R. Metselaar. Electrical properties of yttrium iron garnet at high temperatures. *Physical Review B* **14**, 2520–2527 (1976). URL.

[121] L. Sirdeshmukh, K. K. Kumar, S. B. Laxman, A. R. Krishna & G. Sathaiah. Dielectric properties and electrical conduction in yttrium iron garnet (YIG). *Bulletin of Materials Science* **21**, 219–226 (1998). URL.

[122] K. Modi & P. Sharma. On the effect of SHI irradiation on dielectric properties of Y3xFe5-xO12(x=0.0–0.6) system. *Radiation Effects and Defects in Solids* **169**, 723–739 (2014). URL.

[123] R. Gross & A. Marx. *Festkörperphysik* (De Gruyter, 2018).

[124] B. Howells, M. Wang, K. W. Edmonds, P. Wadley, R. P. Campion, A. W. Rushforth, C. T. Foxon & B. L. Gallagher. Crystalline anisotropic magnetoresistance in quaternary ferromagnetic semiconductor (Ga, Mn)(As, Sb). *Applied Physics Letters* **102**, 052407 (2013). URL.

[125] T. Narr. *All Electrical Magnon Transport in Magnetically Ordered Insulators*. Bachelor's thesis, Technische Universität München (2019).

[126] J. Cramer, L. Baldrati, A. Ross, M. Vafaee, R. Lebrun & M. Kläui. Impact of electromagnetic fields and heat on spin transport signals in Y3Fe5O12. *Physical Review B* **100** (2019). URL.

[127] Q. Ma, Y. Li, D. Gopman, Y. Kabanov, R. Shull & C. Chien. Switching a Perpendicular Ferromagnetic Layer by Competing Spin Currents. *Physical Review Letters* **120** (2018). URL.

[128] D. G. Cahill & R. O. Pohl. Thermal conductivity of amorphous solids above the plateau. *Physical Review B* **35**, 4067–4073 (1987). URL.

[129] D. G. Cahill, M. Katiyar & J. R. Abelson. Thermal conductivity ofa-Si:H thin films. *Physical Review B* **50**, 6077–6081 (1994). URL.

[130] T. Borca-Tasciuc, A. R. Kumar & G. Chen. Data reduction in 3ω method for thin-film thermal conductivity determination. *Review of Scientific Instruments* **72**, 2139–2147 (2001). URL.

[131] L. Zhu, L. Zhu, S. Shi, M. Sui, D. Ralph & R. Buhrman. Enhancing Spin-Orbit Torque by Strong Interfacial Scattering From Ultrathin Insertion Layers. *Physical Review Applied* **11** (2019). URL.

[132] L. Zhu & R. Buhrman. Maximizing Spin-Orbit-Torque Efficiency of Pt/Ti Multilayers: Trade-Off Between Intrinsic Spin Hall Conductivity and Carrier Lifetime. *Physical Review Applied* **12** (2019). URL.

[133] W. Lin, K. Chen, S. Zhang & C. Chien. Enhancement of Thermally Injected Spin Current through an Antiferromagnetic Insulator. *Physical Review Letters* **116** (2016). URL.

[134] Y. Wang, D. Zhu, Y. Yang, K. Lee, R. Mishra, G. Go, S.-H. Oh, D.-H. Kim, K. Cai, E. Liu, S. D. Pollard, S. Shi, J. Lee, K. L. Teo, Y. Wu, K.-J. Lee & H. Yang. Magnetization switching by magnon-mediated spin torque through an antiferromagnetic insulator. *Science* **366**, 1125–1128 (2019). URL.

Acknowledgements

At the end of this work, I want to thank all the people who supported me during this thesis and made this work possible. These are in particular:

- Prof. Dr. Rudolf Gross, for giving me the opportunity to write my Master's thesis here at the Walther-Meißner-Institut.
- Dr. Matthias Althammer for drawing my interest to magnetism and spintronics during the lectures, offering me this topic and welcoming me to the Magnetiker group. Thank you for the extraordinary guidance, for letting me learn by making mistakes and for your patience when I made them, for sharing your profound knowledge through detailed answers to the countless questions I had, for the numerous interventions in the lab concerning all sorts of issues, for writing the LabView scripts, for helping me to find a PhD position and for the proof-reading of this thesis. Your valuable comments determined the interpretation of the results obtained within this work.
- Tobias Wimmer for teaching me basically all procedures done within this thesis, from sample fabrication over measuring to the data evaluation. Thank you for the support throughout this year, be it in the lab, in the process of writing this thesis or for my future plans. Your intuitive explanations of concepts that often caused me headaches, the numerous discussions about physics and the world, all the occasions when you left your work in order to help me, your patience despite my frequent visits and disturbances, proof-reading of this thesis with an SEM and the overall relaxed atmosphere certainly contributed to my personal development and to the quality of this thesis, furthermore making this year pass by as swiftly as possible.
- Janine Gückelhorn for fabricating the PLD YIG films used in this thesis, instructing me how to use the AFM, helping in the lab whenever needed and for her overall supportive attitude.
- Dr. Hans Huebl for asking the right questions, for the sharp-minded observations which could always be relied on and for helping with my PhD application.
- Dr. Matthias Opel and Dr. Stephan Geprägs for suggestions regarding my measurements and generally keeping a great atmosphere during the DC-Meetings and for giving me equal rights regarding the ever-wanted cryostat pump.
- Luis Flacke, Manuel Müller and all the other PhD students for their willingness to help me out, regardless of the kind of issue.
- All my Master colleagues, especially my room-mate Christoph Scheuer, for the pleasant atmosphere, a nice work environment and mutual support.
- The entire staff of the WMI for the kind atmosphere and for accepting me as a WMI member.

- Prof. Dr. Martin S. Brandt for all his support and for always having an open ear for my problems.
- My friends, namely Anel, Arman, Ćazim, Demir, Edin, Nudžeim and Senad for both scientific (especially the countless days spent in the library and your proof-reading Arman) and moral support.
- The light of my eyes, Chayma for her love and support, for constantly pushing me to achieve my best and for being there for me even when I was a walking bundle of stress.
- My aunt Rasema, my uncle Nedžad and my girls Hana and Emina for offering me a warm home filled with love and positive vibes during my Master's studies. Without your support I would not be able to even start this journey.
- My brother Enes for being the best big brother one could imagine. Thank you for always being there for me, for understanding my free-time shortage and for doing everything possible to make my life easier. You raised me beyond the limit of science, my beloved brother.
- My mother Mediha and my father Vahid, for their unconditional love and support, for devoting their lives for the well-being of their children and for being the best advisors. You made me the person I am today and all my achievements are only an embodiment and a consequence of your upbringing.

The One in whose hand is my soul, all praises are for Him in all conditions.